THESIS

INVESTIGATION OF DUAL-PULSE LASER PLASMAS FOR IGNITION OF FUEL-AIR MIXTURES

Submitted by:

Carter Vincent Butte

Department of Mechanical Engineering

In partial fulfilment of the requirements

For the Degree of Master of Science

Colorado State University

Fort Collins, Colorado

Spring 2020

Master's Committee:

Advisor: Azer Yalin

Anthony Marchese
Ryan Bailey

ABSTRACT[1]

INVESTIGATION OF DUAL-PULSE LASER PLASMAS FOR IGNITION OF FUEL-AIR MIXTURES

Progress towards more complex combustion applications has demanded more advanced and versatile ignition techniques.[1–5] One attempt to address some of the concerns associated with well-established techniques such as spark plugs and igniters is laser plasma ignition. Advantages of laser ignition include flexibility of spark location and timing, reduced NO_x formation, leaner engine operation, increased combustion efficiency, and greater system longevity at elevated pressures. Additionally, the non-intrusive nature of laser plasmas results in more unperturbed kernel evolution, as mounting hardware is not required. This is an advantage when compared with spark plug or igniter electrodes which typically act as heat sinks quenching the flame. However, large input energies, complications with beam delivery, and undesirable kernel dynamics have impeded field implementation.[6–8]

Our approach to address these challenges uses a dual-pulse laser plasma where an ultraviolet (UV) beam preionizes a gas mixture and a second near infrared (NIR) beam increases

[1] This work draws heavily from material previously published in a number of AIAA conference proceedings. Those works will be referenced throughout this contribution, but include: (1) Butte C., Dumitrache C., and Yalin A., "Properties of Dual-Pulse Laser Plasmas and Ignition Characteristics in Propane-Air and Methane-Air Mixtures," 2019 AIAA Aerospace Sciences Meeting, AIAA SciTech Forum, 2019. (2) Butte C., Lokini, P., Dumitrache C., and Yalin A., "Single and Dual-Pulse Laser Ignition of Methane-Air and Hydrogen-Air Mixtures," 2020 AIAA Aerospace Sciences Meeting, AIAA SciTech Forum, 2020. (3) Dumitrache C., Butte C., Eickelberg A. and Yalin A., "On the Use of REMPI Pre-ionization for Laser Plasma Formation," 2018 AIAA Aerospace Sciences Meeting, AIAA SciTech Forum, 2018. and (4) Butte C., Dumitrache C., and Yalin A., "Dual-Pulse Laser Ignition Using Oxygen REMPI Preionization," 2019 AIAA Aerospace Sciences Meeting, AIAA Aviation Forum, 2019. For all except (3), my contribution was to collect and analyze all data and be the lead manuscript writer. For (3), my focus was data collection.

the energy and ionization state of the gas. The use of this technique decouples the processes responsible for ionization, predominantly multiphoton ionization (MPI) and electron avalanche ionization (EAI) through inverse bremsstrahlung absorption, and allows for tailoring of plasma properties through adjustments to beam energies and delay time.[9–13] Recent work has shown that dual-pulse laser plasmas not only reduce energy requirements but also enhance ignition characteristics such as combustion efficiency, particularly around the lean limit.[6] The present thesis serves to fill voids in the existing literature with regards to plasma properties and ignition characteristics in various fuels, as well as present a new resonant preionization scheme targeting molecular oxygen at λ=287.5 nm.

Four laser plasmas are investigated in this work: non-resonant single pulse (λ=1064 nm), non-resonant dual-pulse (preionization at λ_{UV}=266 nm with energy-addition at λ_{NIR}=1064 nm), resonant single-pulse (λ_{REMPI}=287.5 nm), and resonant dual-pulse plasma (preionization at λ_{REMPI}=287.5 nm and energy addition at λ_{NIR}=1064 nm). Each of these plasmas are analyzed for electron density and gas temperature using combined Rayleigh Thomson scattering, and are studied for ignition of propane-air, methane-air, and hydrogen-air mixtures. In the analysis, these experimental results are combined with past results to give a comprehensive picture of the ignition abilities of single pulse and dual-pulse plasmas in propane-air, methane-air, and hydrogen-air mixtures.[6,14] Together, knowledge of plasma properties and ignition characteristics give us a more complete picture of the capabilities and limitations of each plasma for combustion applications.

ACKNOWLEDGMENTS

I want to begin by thanking Dr. Yalin for taking a chance on me on as a spread thin undergraduate student, who committed more time to his job with the football team than to research in the lab. When I started, I had little experience with lenses and optics, and had no experience with laser diagnostics. Since that time, I have developed significantly both as a person and as a researcher, even surprising myself when explaining my project to other people. Thank you Azer for aiding me in this development, your support and backing during conferences, and continued guidance on this project, which has no doubt steered the analysis in the right direction a number of times. To Dr. Dumitrache, thank you for the pivotal role you played in training and encouraging me along the way when experimental results were confusing or not even in existence yet. Your feedback and guidance have helped solidify my understanding of plasma physics and laser diagnostics, and the example you set while still here showed me what it means to work hard and approach every problem with tenacity.

I would also like to thank my committee members, Dr. Bailey and Dr. Marchese, for their continued support in this work as well. Dr. Bailey's statics class was the first real engineering course I had in college. Unlike the other classes I had, Dr. Bailey worked to create an environment that was fun and even empowering, and from that class I became excited about engineering and met some of my lifelong friends (Zach, Ryan, Jackson, and Wyatt). I was only lucky enough to have Dr. Marchese as a professor for a class I audited because I was interested in the subject material. Like Dr. Bailey, it was obvious that he was passionate about the subject area, and he did an excellent job of imparting this onto his students. It was part of that class and discussions of it,

that enabled the observed normalized intensity calculations outlined in this work. To both of you, thank you for both supporting me in this project and encouraging me to follow my passions.

I am forever indebted to the teachers I had before college who started me on this path. It is there that I was taught not what to think, but how to think, and was encouraged and stretched in ways I have not been since. It was also there that I became passionate about learning, and I cannot express enough gratitude towards the plethora of people who have contributed to my own development in that manner. To Mrs. Giraldes, Mr. May, Mrs. Sheehan, Mrs. Harris, Mrs. Lechuga, Mr. Magrin, Mr. Block, Mr. Ferguson, Ms. Hendry, Ms. Holladay, Mrs. Dassler, Mrs, Bockhacker, Mr. Babcock, and Mr. Culotta, thank you so much. This document would not exist as it does without each of you wonderful people giving your time and effort to support students as individuals.

I would be a fool to not recognize the support system I have from family members. Their continual belief in me and my abilities (though sometimes unfounded, excessive, and unwarranted) have been a huge contribution to the success of this project and my entire education, beginning with the three years of which I was homeschooled. Thank you mom for showing what it means to care about all people and appreciate the value of different perspectives. Thank you dad for showing me what it means to have an unfailingly good attitude, to never ask what the odds are, and to believe in yourself more than anyone else does. You two have made my life so incredibly easy that I can only hope to repay the debt. Thanks for helping shape me into the person I am today, while allowing me to choose my own path in most areas of my life. To the other members of my family that have showed interest in my project simply because of my connection to it, thank you for showing interest me. I will always enjoy talking practical applications with you Uncle Rex and

joking about the “reverse-osmosis flux capacitor capitulation device” that I am building with you Uncle Rich.

It is also imperative that I acknowledge the colleagues and great friends I have made here at the lab. Adam and Charles, I admire you both for your work ethic, perseverance, and depth of understanding you possess for your respective subject areas. Your example led the way for my success, as did your advice. I am so thankful for the time we got to spend together away at conferences as well as here at home. Charles, if it weren’t for you and Jenni’s selfless sacrifice of your time, I would probably be dead in streets somewhere. Adam, if it weren’t for your commitment to good food, I may have never gained an appreciation for the finer things in life (which is debatable whether I’ve attained but hey there’s been progress). As far as you Ben, I will forever be thankful for the chauffeur service you provided when the weather was termed DiF, as well as iota you preserved of absolute disregard for safety. Thanks for the countless laughs, the early mornings at the gym and related second date updates, the near sleepovers we had in the lab, and the outrageous number of times we got beaten by team James in darts. I have appreciated your presence and general life perspective through the two years we’ve concurrently been here. Thank you Tad for demonstrating on numerous occasions the superiority of AI in explaining theory and understanding mathematics (except for simple addition), as well as contributing significantly to diffusion calculations. This list is by no mean extensive. Numerous other people (Iman, Mars, Puga, Sipich, Brenna, Andrew E., Andrew Z., CVR, Derek) and events (paper airplane competitions, EISL trips and competitions) have made the journey one worth having and remembering with fondness.

I would finally like to thank the friends I have developed here outside of the Powerhouse community. Two groups that were crucial to my success were the original Edwards crew and the

football equipment managers. I keep looking over at you Nick as I write this realizing we went from room neighbors freshman year to desk mates as graduate students. There has been a lot of change that's happened in the last five years, but I know that you, Jake, Cody, Michael, and Alec will be some of my lifelong friends. You are truly some of the most generous and genuine people I know. To the guys who worked for football team with me (Josh, Jon, Tim, Zac, Griff), you guys are equally my brothers. Through thick and thin we found a way to muster the cold without the gear that definitely was ordered and could be found in the well-organized laundry closet right next to Jordan Benson's jersey. I wouldn't trade those experiences for the world.

I am blessed to say that unlike most people, I have had nothing but great relationships with my roommates. To Trent, thanks for providing freshman me a place to live, and entertaining me with deluded sleep-deprived conversations on the bus back from the airport at 4 AM. To Mike, Marcus, Chandler and Detrich, thank you for disrupting my paradigm in more ways than one. Thanks for rounding me out from a too focused person who only cared about work and school to something much more. You guys introduced me to seasonings and tried to teach me how to dance. I loved the diversity of opinions, interests, and life experiences that our group had. I'll never forget the daily McDonald's runs, the late Fortnite chats with you Marcus, and the games of 21 out front with a hoop that only God knows where it came from. Thankful for you all and hope we stay in touch. To Travis, Brando, and Connor thanks for showing me the value of loyalty and longterm friendships. Though we are all independent people, I am incredibly thankful to have been friends as long as we have. Living with you in even abnormal conditions was one of the most fun experiences I had, and I was sad to see it come to an end. To Mike Palasits and Kyle Johnson, thank for being two people who shaped my ability to have

conversations with people I disagree with. You two regularly challenged my viewpoint and showed me the value of not isolating my opinions or conversations of differences.

To my fellow adventurers, I truly am confident that our "Cooky Crusades," kept me going, though it's probably equally true to say that the pursuit of these thrills could've permanently ended me. Chris, Daniel, and Jackson, I feel guilty for never having the sufficient time to fully embraced the climbing mantra, though the ice shelves we dodged, avalanches we saw, and cracks we shimmied through will set the foundation for a lifetime of future excursions. I hope that those will include you. To my ski and board buds, the same truth holds. To my friends of the sky, I have never experienced a community more selfless that finds so much joy in other people's successes. Thank you Mel, Rich, JP, Joni and John for introducing me to a sport I will never be able to abandon, and the unfailing and lifesaving support that has gotten me to this point.

Lastly, I want to thank Mountain View Community church and the people of it. Though I was never quite as involved as I maybe should have been, this is where I truly learned how to follow Jesus. The people here have demonstrated exactly what it looks like to be vulnerable in a place of struggle and to fight through it together. I am thankful to be blessed intellectually such that I feel like I can contribute to scientific discovery, and to be encouraged by people in the church to speak into that realm. It is a remarkable place to be where you realize the complexity of the universe, the vast amount of knowledge we do not have, and then realize we can be in relationship with the designer of it all. Specifically, I would like to thank those mentioned previously (Ryan and Zach) for being persistent with me in my earlier years, and pouring into me on a regular basis in the later ones. I also want to thank my discipleship group (Branton, Josh, and Peter), for the bonds we formed through D-group and events like The Mighty Mighty Super

Duper Scoopa Noodle Challenge (of which Branton was my Calvin Johnson), Nuggets games, ski trips, and adventures in the park. I also want to thank the families that have opened their doors and been available at all hours of the day and night, including the Elgard's and Mitchell's.

Despite my outstanding community here, there are two people whose investment and interest in my life has had greater longevity than anyone else. Drew and Nicole, you two are my rocks. Every time I get to spend time with you two, you remind me of who I am, what I want to be, and encourage me in whatever direction I need to go. I think that the distance we have endured has shown that the bonds we have will truly stand the test of time, no matter our circumstances. I could not ask for wiser more loving friends that you.

Again, this list is not extensive, and a number of other people have influenced who I am today and showed unfailing support. This includes Chase, Collin, Mike L, Sam, Matt A, Sawyer, Austin J, Austin L., Soph B., Seal, Soph L., Cameron C., Daniel R., Jake L., Cole L., Jacob A., Jake H., and the TOU crew. In summary, I have much to be thankful for, and am grateful for every moment I have shared with others along the way.

TABLE OF CONTENTS

LIST OF FIGURES

CHAPTER 1:

Introduction

1.1 Motivation

Developments in laser technology may enable new applications with regards to laser plasmas and ignition. In comparison to traditional options such as spark plugs and igniters, laser ignition removes the physical electrodes (and required mounting hardware) which can act as heat sinks and flame quenching obstacles.[1–4] Use of laser plasmas for ignition can also provide increased flexibility of spark location and timing. Past experimentation has shown that laser ignition can extend the lean limit, reduce NO_x emissions, and increase flame speeds.[5] However, adoption of laser ignition by industry remains minimal owing to a myriad of challenges including large input energy requirements (driving the need for larger sources and limiting fiber delivery) and the need to demonstrate low-cost and reliable systems. These issues, in particular the laser energy requirement, motivate our development of dual-pulse preionization plasma schemes which decouple the ionization and energy addition events, potentially allowing for plasma tailoring and efficient plasma generation. The dual-pulse schemes can also be advantageous to ignite yet leaner mixtures than achievable with single-pulse.[6] The approaches employ a first laser pulse, usually in the ultraviolet (UV), to efficiently generate preionization and a secondary pulse, usually in the near-infrared (NIR), for energy addition. Our past work combining 266 and 1064 nm nanosecond pulses has shown potential towards reducing minimum ignition energies, extending the lean limit of ignition, and improving combustion efficiency.[6,12]

1.2 Physics of Laser Induced Plasmas

Laser based ignition processes are typically due to one of four mechanisms.[15] Two of these mechanisms (thermal ignition and photochemical ignition) are relatively unstudied, owing to difficulties in targeting these mechanisms. For thermal heating, beam focusing has the opposite of the desired effect and creates a diffusely heated region.[15,16] For this reason, a large unfocused beam is typically used, which is undesirable in practical applications.[16] For photochemical ignition, the difficulty lies in small input energy windows. Energy deposition must be large enough to cause dissociation and radical formation at a rate greater than the recombination rate, while simultaneously small enough to not result in significant ionization. When the input energy exceeds some threshold, full breakdown is observed, generally characterized by high electron densities and temperatures, while being physically observed as a violent light emitting spark with an audible blast wave. This full breakdown event is where most laser ignition literature exists, and encompasses the final two ignition mechanisms mentioned by Ronney (non-resonant and resonant breakdown).[15]

In ignition environments, the growth and gas dynamic evolution of the laser plasma and its evolution into a flame kernel are dictated by the initial energy deposition profiles and resulting plasma properties such as electron density and temperature gradients. Subsequently, l fuel consuming flame growth releases heat that can be used to perform work. The generation of such plasmas are caused by a variety of ionization mechanisms, though multiphoton ionization and electron avalanche ionization are the most dominant, which generally work in tandem over the timescale of laser energy deposition (~10 ns).[13] Multiphoton ionization is typically the first stage in plasma formation, where incident laser photon energy is absorbed by a molecule, expressed as the excitation of an electron. Through a series of transitions, formerly ground state atoms (or

molecules) become ionized. The series of transitions define the ionization process as either resonant or non-resonant.[12,13]

One type of multiphoton ionization is resonant-enhanced multiphoton ionization (REMPI). REMPI ionization is a multiple stage process in which incident light, when absorbed by electrons, allows for electrons to traverse different energy levels corresponding to different atomic or molecular rotational-vibrational energy levels. If sufficient energy is then absorbed from secondary photons within "the excitation lifetime," a parameter that defines the amount of time an electron can stay in an excited state before it decays back to its ground state, the electron becomes ionized.[13] When resonant ionization techniques are utilized, the number of photons required for each stage of the ionization of a singular electron is well documented. For instance, Sean McGuire and his associates at Princeton University utilize a 2+2 REMPI ionization scheme for molecular nitrogen (N_2) using a laser wavelength of 283.1 nm.[17] In this scheme, two photons are initially absorbed by molecular nitrogen, exciting an electron to a more energetic state, where it remains for a finite amount of time before absorbing energy from two additional photons to reach a final (energy) state above the ionization threshold.

Non-resonant multiphoton ionization is similar to resonant multiphoton ionization with the exception that electrons are not excited to higher energy levels, but to quantum virtual levels, considered very unstable. The amount of time allotted for the electron to stay in this virtual state is defined by the Heisenberg uncertainty principle

$$\tau = \frac{1}{n*\nu} \tag{1.1}$$

where τ represents the amount of time in the virtual state, n represents the number of photons absorbed, and ν represents the frequency of each photon.[18] This equation demonstrates the characteristic of higher energy levels (particularly virtual ones) to have greater instability, as the

allotted time in the virtual state becomes smaller. Because of the miniscule timescale associated with this type of ionization, it can be thought of as the simultaneous absorption of multiple photons. Experimentation has shown that MPI is more probable to occur at UV wavelengths than NIR, which encourages use in the preionization leg outlined later.[13] Though significantly less efficient at coupling input energy into plasma formation when compared with resonant MPI, it is the most commonly targeted ionization mechanism for laser ignition seen in the literature since fixed wavelength lasers can be used (for example, widely available Nd: YAG lasers at 1064 nm and its harmonics).

Once a number of electrons have been ionized, a secondary ionization mechanism takes place, generally thought of as a cascading or snowball effect. Free seed electrons generated through MPI are accelerated by the electromagnetic field of the laser light. This acceleration of electrons and corresponding increase in kinetic energy absorbed from incident laser light is called inverse bremsstrahlung energy absorption.[19] Free electrons, accelerated by the electric field of the beam, collide with other molecules leading to further ionization. As those electrons then impart their momentum on more molecules, freeing other electrons, a snowball effect occurs.

The combination of MPI and EAI can result in the generation of a plasma at full breakdown, though it is important to note that the competing rates of recombination, stimulated emission, diffusion from the focal volume, and attachment also affect the input energy requirements. This process is summarized in Fig. 1.1, developed by Adlegren, where a) and b) show MPI and EAI processes, and c) and d) show plasma growth (with a lobe toward the laser) and the ensuing blast wave.[19]

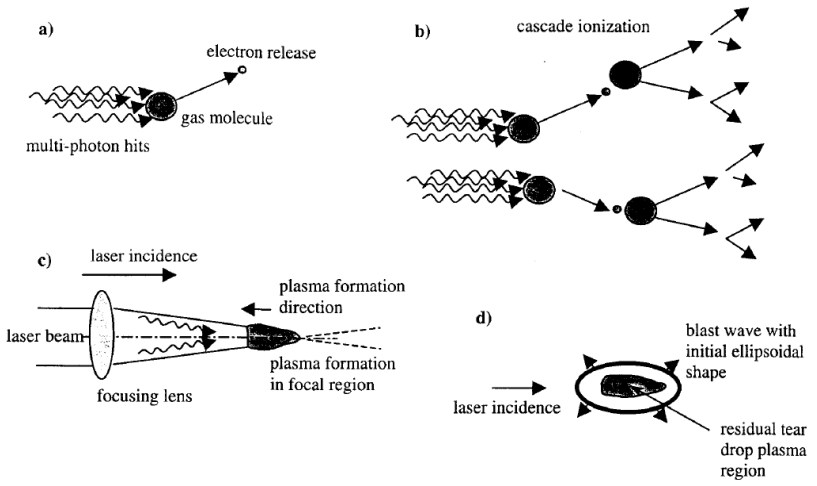

Figure 1.1: The development and growth of a laser plasma. MPI is shown in a), EAI is shown in b), and plasma growth and blast wave propagation are shown in c) and d) respectively.[19]

1.3 Laser Plasma Applications

Laser plasmas are of growing interest for ignition in a host of combustion applications including within the aerospace field. As spark plugs and other igniter technologies reach their performance limit, emerging emphasis is placed on developing new ignition techniques, one of which is laser ignition. Laser ignition techniques have the advantage of not requiring mounts or electrodes, thus avoiding associated heat sink and flame quenching effects, as well as increased flexibility in positioning the ignition source.[1–4] Other advantages include precision timing control and potential combustion enhancement. As new fuel types, including bio-fuels, are developed for aerospace applications, there is a need for development of accompanying ignition techniques. Laser ignition has shown promise in rocket applications including deep space nuclear propulsion and ignition of non-hypergolic fuels in orbital maneuvering thrusters.[20–22] Ramjet and scramjet engines may benefit from spark location flexibility, rapid relight, and potentially spatially (volumetric) arrays of ignition points which contributes to increased control over intermediate reactions, leading to more stable and complete ignition.[20–22] Terrestrial applications include

turbomachinery and reciprocating engines, where laser ignition techniques can offer reduced maintenance requirements, and have been shown to extend the lean limit, increase flame speeds,[5] and reduce pollutant emissions.[6] In certain scenarios, high frequency (multi-pulse) laser induced plasmas have been shown to increase flame stability and assist in flame propagation.[23,24] However, the high energy requirements necessary for gas breakdown have proved a significant obstacle in making laser ignition industrially attractive.[6] Previous studies have found that less than 8% of breakdown energy contributes to ignition, while the rest of the plasma energy is lost through shockwave propagation and radiative processes.[25]

Applications of laser plasmas are not limited to the field of combustion. Two other primary research fields are the use of laser plasmas for standoff detection of hazardous material, and the use of laser plasmas for flow control.

Laser induced breakdown spectroscopy (LIBS) is a technique which uses a pulsed laser, a spectrometer, and an imaging component to determine the composition of a targeted object. Its versatility, simple setup, and rough alignment requirements encourage implementation in rugged and hazardous environments, specifically for in-situ evaluations of potential threats. Recent work by two groups has demonstrated the potential of LIBS to correctly identify explosive materials at both close (~ 1 m)[26–28] and standoff (>100 m)[29–31] distances. Results suggest that LIBS is a viable candidate to replace current demining techniques and a sufficient means to safely identify improvised explosive devices (IEDs).

LIBS has extended its usefulness to many other fields as well. In the late 1980s and early 1990s, applications of this technique began to reach outside the fields of science and research. Smaller, more portable devices started being built commercially as a means to address safety concerns. Some monitored beryllium concentrations in ambient air. Others were dedicated to study

lead concentrations in paint and soldered joints. With each new application, the demand for more portable and easy to operate systems increased. Eventually, LIBS devices could be found in a variety of industries, measuring concentrations of soil contaminants and air pollutants, characterizing metals, explosives, chemical and biological threats, radiological and nuclear materials (CBRNE) and even operating in underwater conditions.[32,33] One extensive field being rapidly advanced is that of LIBS for biological measurements. LIBS has shown promise in detecting and monitoring cancer, bacteria, airborne infectious diseases, viruses, allergens, fungal spores, pollen, as well as biohazards such as anthrax.

Perhaps the most famous recent implementation of LIBS can be found on the Mars Curiosity rover. This undertaking began in the Nevada desert on the NASA Ames "K9" rover.[34] This was the first field test attempting to demonstrate standoff detection of composition. The K9 not only proved that composition calculations were possible, but informed decisions about how future units should be built. It brought to light concerns about spectral resolution, focusing spot size, allocation of time for data collection, dust coating effects, and localized variations in composition both laterally across the surface and vertically into the ground. Providing sufficient promise, a new ChemCam system was built and mounted to the Curiosity rover. With capability of analyzing samples up to seven meters away, this device gave some of the first information about the Martian soil that we may someday call home. In summary, LIBS is not limited in the areas in which it can be applied, and its simplicity allows for relatively easy implementation for measurements of all kinds of specimens.

In terms of flow control, conventional airfoils typically utilize mechanical flaps which are actuated to allow greater control over lift at takeoff and landing. They are then stowed once the aircraft reaches cruising altitudes. However, these systems are far from ideal, increasing

component complexity and possibility of mechanical failure, adding weight to the wing, and creating parasitic drag due to mounting requirements.

A suggested alternative is the use of plasma actuators, which require minimal hardware and achieve similar (and occasionally better) lift properties to those of mechanically actuated flaps. Additionally, they lack the parasitic drag that mechanical actuators are known for. Most commonly, plasma actuation is done using electrodes or dielectric barrier discharges (DBDs), though laser induced plasmas provide the same effect with greater versatility due to focusing capabilities. This allows for greater versatility in flow control and custom optimization for desired applications. Multiple groups have shown the effects of varying focusing locations along the wing for a variety of airfoils on lift coefficients, formation of vortices, and turbulence.[35–37] Others have demonstrated that airfoil roll is made possible through plasma actuation, begging the question of just how far plasma actuation can change flight control at both subsonic and supersonic speeds.[38–40]

Plasma actuation is not limited to aircraft applications. Wind farms have entertained the idea of using plasma actuation on turbine blade airfoils as a means to control flow separation and accordingly minimize drag.[41] Plasma actuation has also entered the realm of acoustics, where multiple groups have demonstrated the ability of plasma actuation to provide real time noise cancelling by the superposition of deconstructive waves.[42]

We focus primarily on the use of laser induced plasmas for combustion. LIBS and plasma actuation are just two non-combustion related fields of laser induced plasmas. Many more fields and uses of laser induced plasmas exist, and will continue to be developed to match the demands of new technology and applications.

1.4 Dual-Pulse Laser Plasmas

Of recent and growing interest addressing the ignition challenges of single pulse laser plasmas is the use of multiple lasers to form ignition probable plasma. Our group specifically examines multi-pulse plasmas based on two nanosecond laser pulses operating at different wavelengths, as a means to expand ignition windows and tailor properties such as gas temperature, electron number density, and plasma size and hydrodynamics.[6,12,13] By decoupling the two processes responsible for plasma formation, multiphoton ionization (MPI) and electron avalanche ionization (EAI), the dual-pulse technique makes plasma properties controllable and requires less input energy than well-established laser spark ignition.[12,13] Mahamud et al. recently developed a model illustrating that properties such as kernel growth and ignition delay are made controllable through adjustment of laser intensity and focusing distance.[9] Past research has shown that UV laser ionization is dominated by MPI processes, while NIR breakdown is dominated by EAI processes.[13] Accordingly, our method uses a UV laser pulse (λ=266 nm in the present work) for pre-ionization, and a secondary NIR laser pulse (λ=1064 nm in the present work) for energy addition to seed electrons. Other research has examined the effect of time-spacing between pulses for multi-pulse and repetitive-pulse schemes and combinations of laser and microwave pulses. [24,43–45] Dual-pulse plasmas have been shown to cause less flame stretching and successful suppression of an undesirable third lobe, commonly observed with other laser ignition techniques.[6] These properties result in better ignition characteristics, particularly with regards to increased efficiencies and extension of the lean limit.[6,20] In high speed flows, dual-pulse plasmas (created with other wavelength/timing schemes) also have increased ignition probabilities compared to single pulse plasmas of equivalent energy.[24] For these reasons, we continue to investigate dual-pulse plasma ignition characteristics, with an emphasis on a new resonant enhanced scheme. To characterize

plasma properties and relate them to combustion characteristics, we apply a number of laser plasma diagnostics.

1.5 Laser Plasma Diagnostics

Laser diagnostics are broadly defined as the techniques employing lasers to measure physical parameters of a sample (gas or solid etc.) of interest.[46]Typically, the collected data is composed of some kind of light, which can be spectrally and/or spatially resolved. For our purposes, we employ certain laser diagnostics to characterize the novel laser plasmas we generate for ignition. This section will discuss the general laser diagnostic techniques used to measure the plasmas of interest in this work, and will briefly detail some other similar diagnostic techniques.

The most significant laser diagnostics used in our study of plasma parameters are Rayleigh and Thomson scattering. Rayleigh scattering is the result of elastic scattering of light from molecules. When incident light of a given electric field reaches a molecule, the dipole moment of the molecule begins to oscillate much like a spring. The oscillating molecule can then considered a radiating dipole, emitting photons of equivalent wavelength to the incident ones at a one-to-one ratio. A simple example of Rayleigh scattering can be observed by looking up at the sky. When observing a region of the sky the corresponding light is the resultant scatter from gas molecules in that region. During the middle of the day, when sunlight propagation direction is orthogonal to the atmosphere and has to travel a shorter distance, the sky is observed as blue, due to the frequency intensity relationship described earlier. At sunrise and sunset, blue light is still scattered with greater intensity, but the distance it has to travel is much further, as is the density of the medium through which it travels. The result is that the blue light diffuses much more rapidly than red light because of multidirectional scattering. The red light that then reaches an observed point of the sky

at dawn/dusk then still has sufficient energy to Rayleigh scatter in an observable manner while the blue light does not.

A number of parameters can result in the spectral broadening or frequency shift of the Rayleigh scattered light, of which the main culprits are Doppler broadening (thermal broadening), and Stark broadening (pressure broadening). In all experimental setups, a third parameter, referred to as instrument broadening, must also be accounted for. Typically, the broadening mechanisms act in conjunction, and form a Voight profile based upon the independent constituent distributions (Gaussian and Lorentzian lineshapes). Though this is an issue when spectrally resolving the data or when using spectrally sensitive optics like the filter mentioned in chapter four, it can be neglected for most Rayleigh scattering thermometry measurements, as only the intensity of light matters, assuming the sensitivity of the detector is constant over the spectrally broadened lineshape (which is typically the case).

Rayleigh scattering intensity (I) is known to be dependent on incident frequency (ν) by the relation $I \sim \nu^4$.[47] Exploitation of this relation can be beneficial for a variety of diagnostic measurements. One such case is described by Limbach et al., where two color Rayleigh scattering is used to separate contributions of Rayleigh and Thomson scattering.[48,49] This is necessary and desirable because at early times (< 1 μs) in the plasma decay process, there is a significantly high electron density such that the perceived intensity is the combination of both Rayleigh scattering and Thomson scattering. By using this two color technique, one can more effectively separate the Rayleigh and Thomson scattering contributions.

For our purposes, we will focus on Rayleigh scattering thermometry, which uses Rayleigh scattering as a means to measure gas temperatures inside a plasma (which can be equated to electron and ion temperatures assuming the plasma is in equilibrium). The basic principle of

Rayleigh scattering thermometry is that localized temperature variations can be predicted assuming the ideal gas law and relating the localized particle density to the observed detector intensity. Though the observed signal is dependent on a number of other parameters, like optical component transmission percentages, detector quantum efficiencies, and the collection solid angle, these parameters can be neglected when normalized to a reference condition. The full procedure for Rayleigh scattering thermometry is described in a number of past publications by our group and others, and specific analysis is described in more detail for the single pulse plasma.[13,48,50]

As described above, when performing Rayleigh scattering on a scattering volume comprised of a mixture of atoms (and molecules) and electrons, it is inevitably accompanied by Thomson scattering, a similarly elastic scattering process for free electrons. As will be further discussed herein, in some cases (even with a single probe wavelength) we are able to separate the Rayleigh and Thomson contributions to measure both gas and electron density.. Another approach to measuring low density plasma measurements uses a high reflective cavity to enhance the scattering from the focal volume, and is hence termed cavity enhanced Thomson scattering (CETS).[51,52] It is similar to cavity ringdown spectroscopy (CRDS), but the scattering volume scatters light instead of absorbs it. For CRDS, a laser of wavelength resonant to a target molecule transition is scanned in frequency space, and the resulting ringdown time pattern can be correlated to the density of the absorbing molecule. Other laser diagnostics that are capable of measuring plasma and experimental properties include optical emission spectroscopy (OES), coherent anti-Stokes Raman spectroscopy (CARS), laser induced fluorescence and two photon absorption laser induced fluorescence (LIF and TALIF), and particle imaging velocimetry (PIV), just to name a few.

1.6 Thesis Objectives

Presented here is extensive testing performed on single pulse plasmas and dual-pulse plasmas formed using a UV preionization pulse and an NIR energy addition pulse. This contribution seeks to fill in the existing gaps for non-resonant behavior, such that a metric for comparison exists when similar parameters are studied for a new resonant enhanced dual-pulse scheme which targets molecular oxygen at λ=287.5 nm. Specifically, this thesis measures the plasma parameters of electron density and temperature for four plasmas of interest. Secondarily, it evaluates ignition characteristics of these plasmas in three fuel air-mixtures. The goal is to have a good understanding of plasma parameters for each condition as to be able to effectively explain ignition characteristics for each fuel. The plasmas of interest are the non-resonant single pulse NIR case, the non-resonant dual-pulse case, the resonant preionization pulse, and the resonance enhanced dual-pulse plasma (REMPI dual-pulse). The mixtures of interest are propane-air, methane-air, and hydrogen-air. For all plasmas, combined Rayleigh/Thomson scattering is performed, while ignition testing is performed for all cases except the resonant preionization plasma, which does not exhibit tendencies of full breakdown, and does not possess sufficient energy deposition to ignite fuel air mixtures independently.

1.7 Thesis Outline

The rest of the document is laid out as follows. Chapter two details non-resonant plasmas, including the single pulse NIR case, and the dual-pulse preionization case, the results of the employment of Rayleigh/Thomson scattering diagnostics, and ignition characteristics in methane-air and hydrogen-air mixtures. In attrition to providing useful insight into these specific plasmas, this section also provides a baseline for which the resonant plasmas (Chapter 3) can be compared.

The third chapter follows with parallel structure, this time analyzing the resonant preionization plasma and the resonant enhanced dual-pulse plasma for the same properties. Chapter four describes progression towards a future filtered setup for combined Rayleigh/Thomson, which will provide 2-D planar measurements (as opposed to the current 1-D measurements) using a planar beam along with a molecular (iodine) vapor filter to suppress background light scatter. Chapter five makes final conclusions and compares each of the plasmas in terms of plasma parameters and ignition characteristics, while detailing sources of error and potential future work.

CHAPTER 2:

Non-resonant Plasma Properties and Ignition Characteristics[2]

2.1 Introduction

We begin our investigation by filling in gaps that exist in literature for the most commonly used plasmas. Specifically, we investigate single and dual-pulse plasmas that utilize the direct ionization methods of MPI and EAI detailed earlier. Most existing literature exists in the single pulse realm, though variations in wavelength, pulse energy, focusing conditions, fuel types, and beam parameters makes extrapolation to our test setup difficult. We are particularly interested in the electron density and gas temperature of the plasma, while also interested in having a metric for comparison with regards to combustion efficiency and the lean limit. Accordingly, we employ Rayleigh/Thomson diagnostics to measure plasma properties, and perform ignition studies in propane, methane, and hydrogen air mixtures. Once this metric is established, we create a non-resonant dual-pulse plasma of energies corresponding to E_{UV}=20 mJ and E_{NIR}=40 mJ and evaluate the same properties using the same methods. The goal is to ascertain what ignition benefits exist (if any) when using different plasma types, and then hypothesize why they exist based upon plasma properties determined through diagnostic techniques. This is the goal for all of the plasmas formed, and carries over into the resonant plasmas investigated in Chapter 3.

[2] This chapter draws a significant amount of material from two conference papers: (1) Butte C., Dumitrache C., and Yalin A., "Properties of Dual-Pulse Laser Plasmas and Ignition Characteristics in Propane-Air and Methane-Air Mixtures," 2019 AIAA Aerospace Sciences Meeting, AIAA SciTech Forum, 2019. (2) Butte C., Lokini, P., Dumitrache C., and Yalin A., "Single and Dual-Pulse Laser Ignition of Methane-Air and Hydrogen-Air Mixtures," 2020 AIAA Aerospace Sciences Meeting, AIAA SciTech Forum, 2020. For both papers, my contribution was to collect all data and lead the writing of the manuscript.

2.2 Experimental Setups

We use the fourth-harmonic (λ=266 nm) of an Nd:YAG (Continuum Powerlite 8010) for preionization and the fundamental output (λ=1064 nm) from a second Nd: YAG (New Wave Gemini) for energy addition. The two together, separated temporally by 15 ns using a pulse delay generator (Berkeley Nucleonics 555), form the dual-pulse plasma. The preionization beam is attenuated to an energy of E_{UV}=20 mJ and has a pulse duration of approximately 7 ns. The energy addition pulse has an energy of E_{NIR}=40 mJ and has a pulse duration of 10 ns. These energies were selected to match the conditions of dual-pulse plasmas used for ignition of propane-air mixtures in the past.[6] The optical layout for dual-pulse plasma formation is shown in Fig. 2.1. The beams are spatially overlapped using a beam splitter (ThorLabs HBSY134) and focused to a common waist using two lenses of focal length f = 300 mm. Rough beam overlap is achieved with irises and pinholes, while final precise alignment is achieved by minimizing the laser energies required to spark. The lens for the energy addition pulse is placed on a translation stage as to be able to optimize and adjust the axial offset of the two beams. The beams are focused to the approximate center of a custom chamber of volume V = 195 cm^3 in which ignition experimentation is performed. The same 1064 nm laser used for energy addition is also used for single pulse plasma formation, where the duration is the same but the energy is raised to E_{SP}=60 mJ. A dynamic pressure transducer (PCB Piezotronics 113B24) mounted on the side of the chamber is used with an oscilloscope (Rigol DS1204B), to record pressure histories of ignition, while simultaneous OH* chemiluminescence imaging is performed using an ICCD (pco DICAM pro) and an optical bandpass filter (Andover 310FS10-50) of wavelength λ~310 nm.

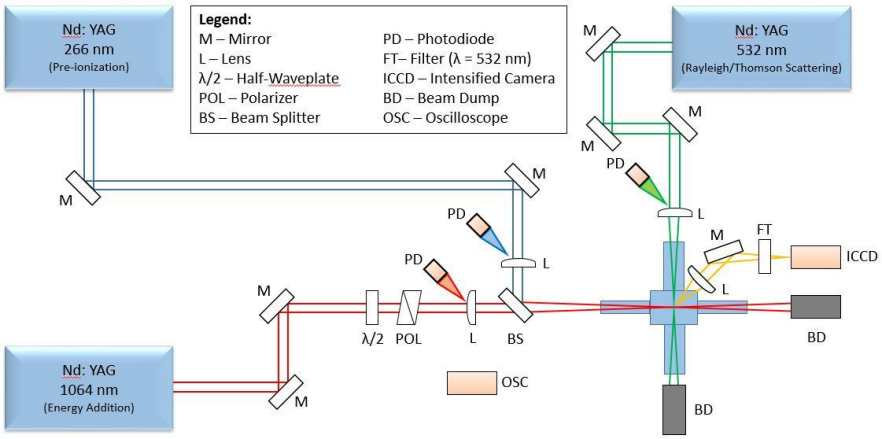

Figure 2.1: The optical setup for the dual-pulse plasma with Rayleigh/Thomson scattering diagnostic.

An additional Nd:YAG laser source (Spectra Physics Quanta Ray) operating at 532 nm is used for diagnostics by (combined) Rayleigh and Thomson scattering. The diagnostic probe beam is introduced into the combustion chamber using dielectric steering mirrors and focused with a plano-convex lens (f=250 mm). The diagnostic beam is orthogonal in direction to the plasma formation beams and weakly focused in the laser plasma region, possessing a beam waist diameter of approximately 190 µm (narrower than the laser plasmas that it is used to probe). The scattering signal is collected along a direction orthogonal to both the plasma formation and diagnostic beam axes with a collection lens (f=75 mm). It is then imaged through a 532 nm bandpass filter (ThorLabs FL532-10) onto an ICCD camera (pco DICAM pro). Baffles positioned inside the chamber reduce the amount of background light collected by the camera (i.e. reduce the elastic scattered laser light from the chamber windows and spurious reflections etc.). The camera imaging is executed using 2 x 2 binning, resulting in an image resolution of 512 x 640 pixels, with a spatial resolution corresponding to 11 µm/pixel. 774 images are collected for each condition (three sets of 258 images) and photodiodes are utilized to monitor the timing of each laser as well as the camera. A similar setup is used for plasma characterization studies and ignition studies, but in the

latter case the chamber arms for delivery of the diagnostic beam are removed. For combustion heat-release analysis, pressure data is collected using a dynamic pressure transducer (PCB Piezotronics 113B24) and oscilloscope (Rigol DS1204B).

2.3 Single Pulse Plasma

Single pulse laser plasmas were generated in the NIR (λ=1063 nm) using the aforementioned Nd:YAG laser. Presented here are the results of combined Rayleigh/Thomson scattering, used for measurement of the electron density and temperature of the plasma, and combustion in methane-air and hydrogen-air mixtures, as to supplement ignition testing performed by our group in propane-air mixtures. We present a new technique to estimate plasma temperatures, based upon assumptions of chemical equilibrium under the scenarios of constant volume and constant pressure plasma evolution. We report a peak measurable electron density of n_e~$3.9x10^{17}$ cm^{-3} at a time of 300 ns after laser energy deposition in the focal volume, and maximum measureable temperature of 9,400 K at 7.5 μs, which is in good agreement with literature.[13] For ignition, we report lean limits of ϕ=0.12 for hydrogen, ϕ=0.53 for methane, and literature reports a lean limit of ϕ=0.70 for propane.[6] In terms of the kernel shape, a toroid structure with a third lobe is observed in all fuels, but that hydrogen-air mixtures tend to not exhibit the third lobe feature at near stoichiometric conditions. This third lobe detaches from the toroid in lean mixtures, resulting in flame quenching and extinction.

2.3.1 Electron Density Measurements by Thomson Scattering

We have performed 2-D scattering measurements of the laser plasmas to examine plasma density and gas temperature. The scatter signal is due to a combination of Rayleigh and Thomson

scattering (and much weaker Raman scattering). At early times the scattering signal is primarily due to Thomson scattering, and can be used for electron density determination, while at later times the signal is primarily Rayleigh, allowing for determinations of gas temperature.[49] The transition between the two regimes can be difficult to determine and in the present case is set as the time when the central Thomson peak (clearly visible at early times) diminishes to be no longer discernible. The NIR plasma had E_{NIR}=95 mJ. The scattering profiles are plotted in Fig. 3 where the vertical axis shows the scatter and the horizontal axis is the spatial position transverse to the plasma formation axis. The inset shows the orientation of the probe beam relative to the laser plasma axis – the dark region in the middle is due to low density and high temperature. The scattering signal, I, is normalized by a baseline signal, I_0. The method to infer electron density, at the center position, is based on lower and upper bounds of the Thomson peak and has been described in our past work.[13] Taking the 1 μs delay profile (Fig. 2.2) as an example, one sees that far away from the center of the plasma, the signal remains unchanged (I/I_0=1), because the plasma induced shockwave has not reached this point. Working inwards, we observe a large increase in signal due to scattering from increased particle density on the leading edge of the shockwave. The reduction in intensity in the central portion is attributed to rarefaction on the trailing edge of the shockwave and the elevated temperature (reduced density) of the plasma kernel, while an upward pointing peak due to Thomson (electrons) is also present.[13,49]

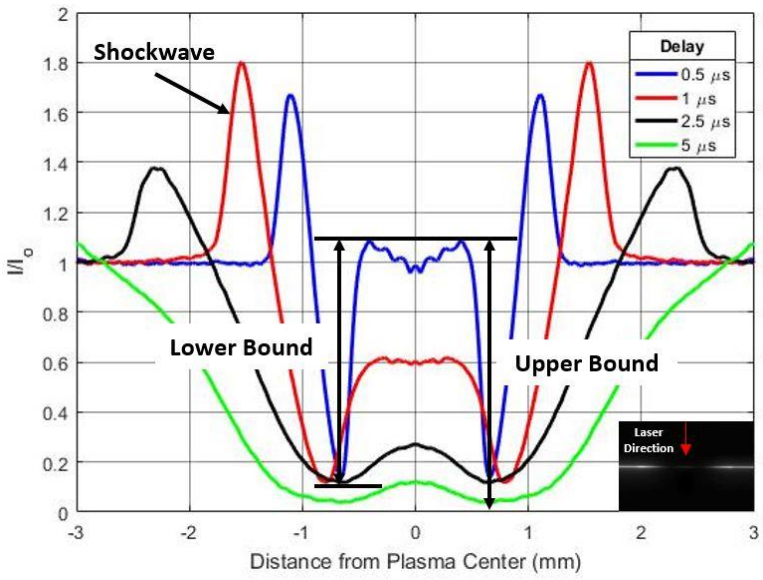

Figure 2.2: Rayleigh scattering signal along the transverse axis of the plasma for a NIR laser plasma. The signal has been normalized by the intensity of the scattering beam. The rise of central portion of the signal is due to Thomson scattering. Images in the bottom right detail the raw ICCD images at a delay of 2.5 μs. The plasma formation lasers enter from the top of the image.

For the 0.5 μs delay case the lower and upper bounds of the Thomson scatter are shown, from which the electron density can be estimated.[13] Electron density decay for the NIR plasma can be seen in Fig. 2.3, where the uncertainty bars span between the bounding values. We report a peak electron density of $n_e \sim 3.9 \times 10^{17}$ cm^{-3} measured for the single pulse NIR plasma at delay of 300 ns after plasma formation. This is in good agreement with electron densities for similar plasmas.[53,54]

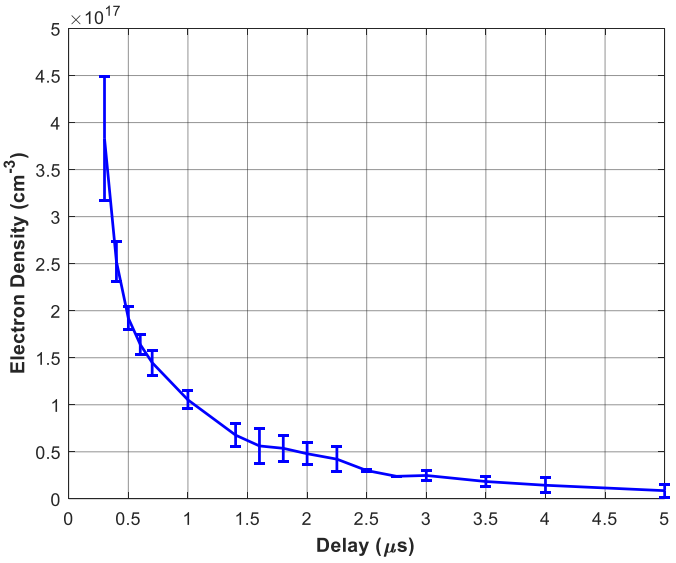

Figure 2.3: Electron density decay for the NIR plasma as a function of time.

2.3.2 Diagnostic Development Towards Temperature Measurements

In general, the Rayleigh/Thomson technique can be used for Rayleigh scattering gas temperature measurements at later times following the decay of the electron density (Thomson). In this manner, electron density values are calculated for early delays, and temperatures are calculated for later delays. Realizing that it would be informative to understand early plasma dynamics, NASA chemical equilibrium code was used to predict scatter intensity ratios (*I/Io*) across a wide variety of temperatures under two different scenarios, the first of which is a constant pressure of 1 bar. Limitations in the code prevented us from exceeding temperatures of 22,000 K. Comparing the computed equilibrium scattering signals versus temperature with those experimentally observed may also give insight into the state of plasma equilibrium. Fig. 2.4 shows the predicted densities of air constituents, as a function of temperature and assuming fixed pressure.

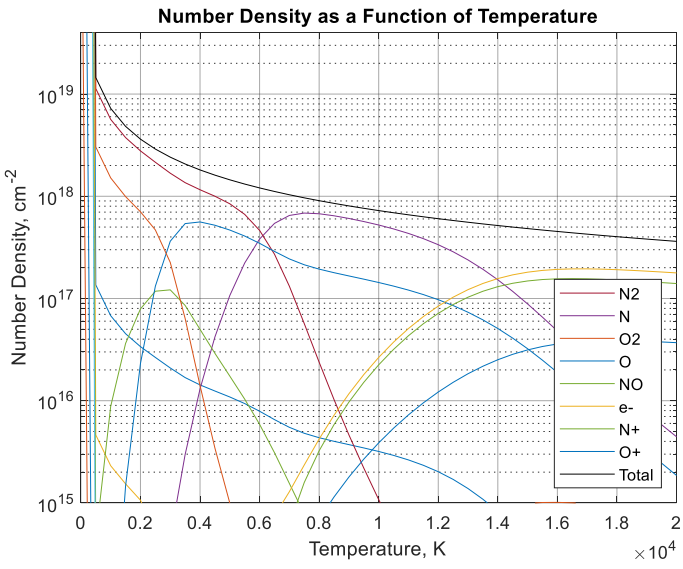

Figure 2.4: Component species concentrations as a function of temperature. This plot assumes fixed pressure (1 bar) and uses NASA chemical equilibrium code to determine mole fractions of each component species.

By combining the equilibrium component species densities with (temperature dependent) scattering cross sections, we can predict the normalized scattering signals expected for equilibrium conditions:

$$\frac{I-I_B-I_P+I_D}{I_0-I_B} = \frac{\sum_i n_{R_i}*\sigma_i(T)+n_e\sigma_T}{\sum_i n_{R_{i_0}}*\sigma_{i_0}(T_0)} \tag{2.1}$$

where I is the scattering image, I_B is the background image with no laser beams at reference conditions (P_0=1 bar, T_0=298 K), I_P is the plasma image with no scattering beam at the reference conditions, and I_D represents the dark counts of the camera. For brevity, this term is represented as I/I_0. On the right side of Eqn. (2.1), n_{R_i} represents the density of the component species (Fig. 2.4), σ_i the Rayleigh scattering cross-section, n_e the density of free electrons, and σ_T the Thomson scattering cross-section (corrected for temperature by the Salpeter approximation). Subscripts of zero denote the same properties at a reference temperature of 298 K. In summary, this equation is stating that the ratio of the scattering signal in an ionized medium to that in ambient environment

is equivalent to ratio of the sum of the Rayleigh and Thomson scattering that is observed in the ionized medium to the Rayleigh scattering that occurs in an ambient environment (with negligible electrons). Fig. 2.5 shows the predicted scattering intensities as a function of temperature for an equilibrium air plasma at constant pressure.

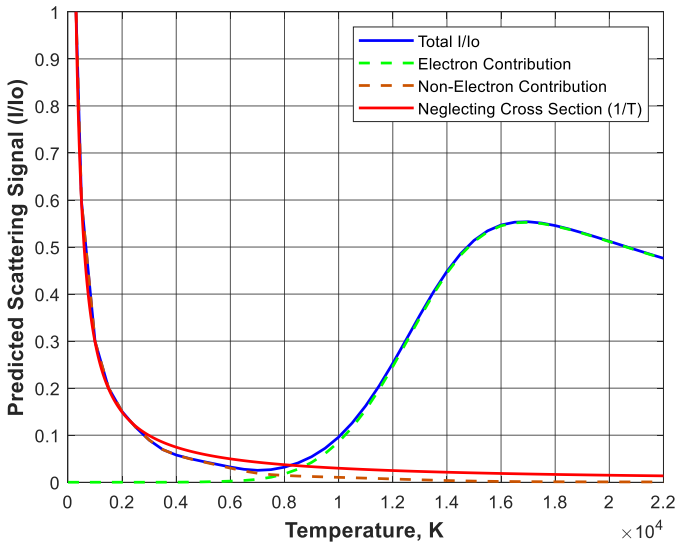

Figure 2.5: Predicted scattering signal as a function of temperature for equilibrium air plasma at 1 bar. The blue curve represents the total observed scattering signal which has contributions from electrons (dashed green curve) and non-electrons (orange curve). An ideal gas law (*1/T*) estimation of *I/Io* is shown in red.

Considering Fig. 2.5, if one were to neglect the change in species composition (in particular the increase in electrons at T~8,000 K) and temperature dependent cross-sections, then the predicted scatter signal would simply reduce with temperature as *1/T* based on decreasing density. This type of analysis also shows that if one neglects composition and cross-section temperature dependences, one can make relatively accurate temperature measurements (based on simple *1/T* dependence) up to around 3,000 K.[49,55] Another important finding from Fig. 2.5 is that the (normalized) scatter intensities should never fall below 0.0253 (which occurs at ~7,000 K) and should never exceed 0.554 (~17,000 K) over the domain of 298-22,000 K. However, our data shows cases with scattering intensities greater than 0.554 at early times (see Fig. 2.2). This result

has also been observed multiple times in the past.[13,49] There are several possible reasons for this. The first is that the plasma is in chemical non-equilibrium at early times owing to the complex kinetics and/or time-scales associated with collisional and radiative processes. The possibility of nonequilibrium in the laser plasma is interesting given that a large body of laser plasma research assumes LTE based on the McWhirter criterion.[56,57] The second potential explanation (which could act in conjunction with the first) is that the constant pressure assumption is invalid. We believe this to be the case at sufficiently early times, as demonstrated by Dumitrache et al. through the detailed modeling of dual pulse plasma.[58]

Interested in expanding our range for which we can make temperature measurements, we followed the same sort of analysis for a constant volume scenario. Though obviously not ideal, this kind of analysis more appropriately approximates the first microsecond of plasma kernel formation and development. The number density of constituent particles for the constant volume case is shown below in Fig. 2.6.

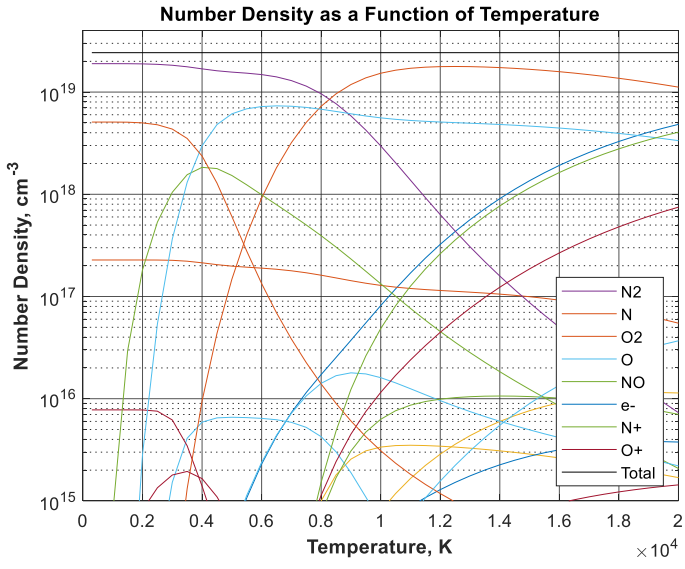

Figure 2.6: Component species concentrations as a function of temperature. This plot assumes fixed volume (195 cm^3) and uses NASA chemical equilibrium code to determine mole fractions of each component species.

Note that the though the number density of this plot differs from that of the constant pressure case (Fig 2.4), the mole fractions of each component species are approximately equal across all temperatures. The use of constant pressure instead of constant volume is essentially a simple scaling of the number density based on the ideal gas law, where regions of the plasma kernel with higher temperatures at constant pressure have a corresponding decrease in density. Using Equation 2.1, we can relate the known number densities inside our chamber to a measured intensity value (*I/Io*).

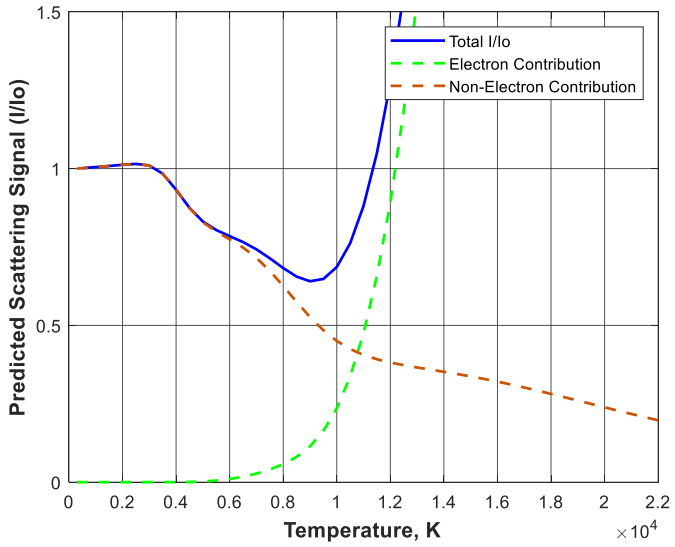

Figure 2.7: Predicted scattering signal as a function of temperature for equilibrium air plasma at constant volume. The blue curve represents the total observed scattering signal which has contributions from electrons (dashed green curve) and non-electrons (orange curve).

This is the equivalent of Fig. 2.5 for the constant volume case. As expected, high temperatures dictate a large increase in the electron density inside the scattering volume. Accordingly, the observed intensity *I/Io* skyrockets with temperature as the average scattering cross section in the scattering volume increases. However, this type of analysis presents some concerns of its own. The first is the importance of a high signal to noise ratio during data collection.

If calculations for the normalized intensity deviate by values greater than 1.5%, the estimated temperature at that point will exceed 11,000 K. Secondarily, the normalized intensity should never fall below 0.641 (which happens at 9000 K). We know this occurs at much later delays, but we also note that the constant volume assumption is broken in this regime as well.

Both of these types of analyses are an improvement from previous techniques. Previous estimations were developed from the most generally accepted method to determine temperature from the Rayleigh (dominated) scattering profiles. This method uses a ratio approach where (at each spatial position) the intensity for a given condition of interest, *I*, is normalized by the Rayleigh signal, Io, from known reference conditions (in this case T_0=298 K, P_0=1 bar). Then, assuming the ideal gas law and uniform pressure between the two cases, the unknown temperature can be readily found from the ratio *I/Io*. Further details on the method, including background subtraction, can be found in our past work.[13] The aforementioned approach does not however account for variations of species composition (e.g. due to dissociation of nitrogen) with temperature, nor the variation of the contributing cross-sections with temperature. Provided a significant amount of time has passed, one can successfully use this method and fairly accurately estimate the temperature, as long as complete recombination has occurred and temperatures have subsided to reasonable temperatures (T<3,000 K). These two qualifiers usually happen in tandem. Though most literature that exists using the ideal gas assumption does predict temperature in this low temperature region, some cases do exist where estimated plasma temperatures exceed 10,000 K.

In order to understand how accurately these two models predict temperature, we must consider the underlying assumptions. First, both models assume equilibrium. The vast majority of existing literature agrees that for most laser plasmas, this is an appropriate assumption, though it is reasonable to trust this assumption at later delays (the constant pressure case). Examining the

model developed by Dumitrache at all for the dual-pulse plasma (Fig. 2.8), we see that the plasma expands from a radius just under 1 mm to just over 1 mm in the first 500 ns.[58] From 500 ns to 2 µs, the plasma radius grows to nearly 4 mm. Examining this plot, we can see that our constant volume assumption breaks down between 500 ns and 2 µs. For this reason, we apply our CV analysis over the range of 0-800 ns.

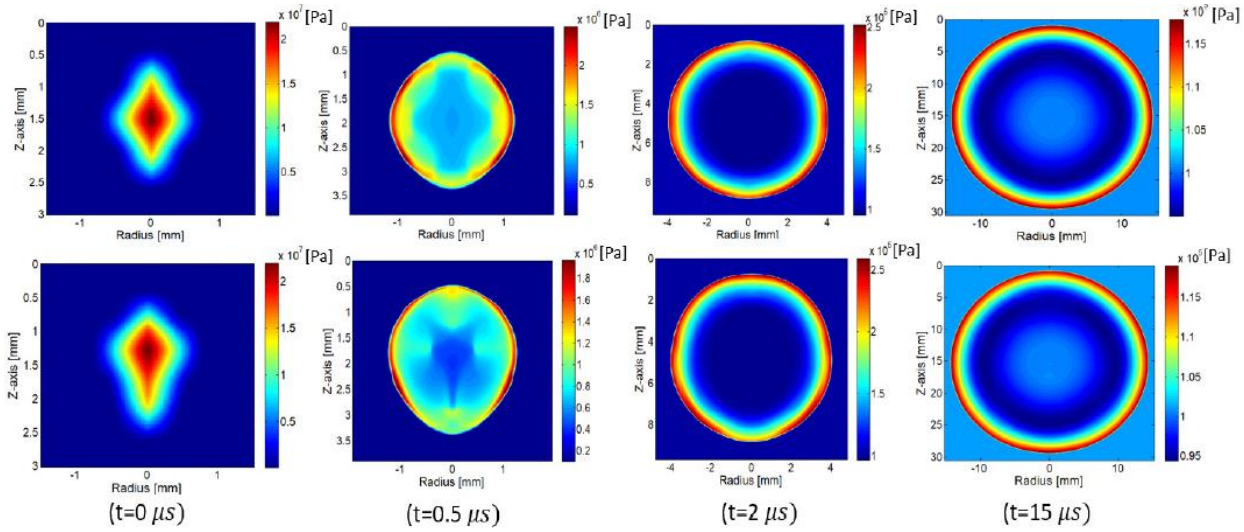

Figure 2.8: Modeled dual-pulse plasma pressures at varying times. The top case imitates an ideal overlap of the waists, while the second imitates a waist offset. Analysis of this model demonstrates that our constant volume assumption breaks down between 500 ns and 2 µs.[58]

A pressure analysis on the same model shows that the kernel pressure doesn't subside to approximately ambient conditions until around 10 µs. At 5 µs the maximum pressure is ~150 kPa near the shockwave. However, we anticipate maximum temperatures to be inside the plasma kernel near the centerline, as shown in Fig. 2.9. Because we only care about maximum temperatures, as long as the region corresponding to maximum temperature has a localized homogenous pressure gradient surrounding it, we can assume constant pressure and make estimations of temperature. For this reason, we assume a constant pressure analysis to be appropriate over the timescale of t=5-10 µs.

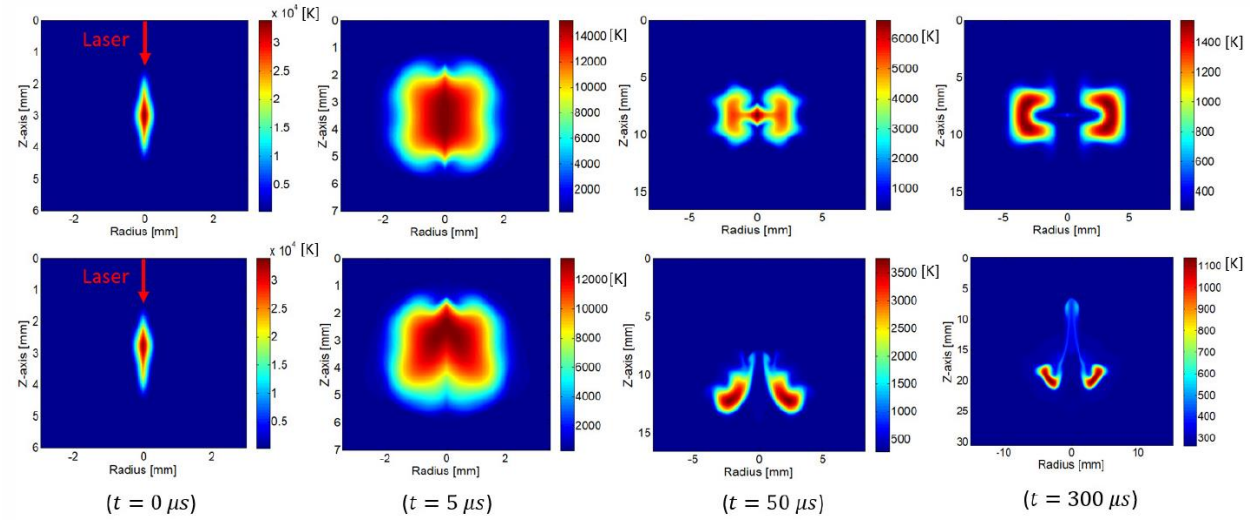

Figure 2.9: Modeled dual-pulse plasma temperatures at varying times. The top row models a perfect overlap of the two waists, while the second shows an offset. Analysis of this model demonstrates that though our plasma pressure may vary over the regime of 5-10 µs, the maximum temperatures we calculate with be regions where the pressure is approximately constant.[58]

Though the previous model and analysis is for dual-pulse plasma propagation, recent (unpublished) simulations have been performed for single-pulse plasmas yielding similar conclusions in terms of applicable time regimes for CV and CP analysis. We therefore extend this type of analysis (and time-window regimes) to single pulse plasmas as well as the resonant dual-pulse plasma. Given the limited range over which we can assume constant volume and constant pressure, we generally obtain segmented plots where the first section estimates temperature under constant volume and chemical equilibrium assumptions, while the second section uses a constant pressure assumption. The time scales corresponding to these regions are sufficiently early times (t≤800 ns) for constant volume analysis, and sufficiently late times (t>5 µs) for constant pressure analysis.

2.3.3 Temperature Measurements by Rayleigh Scattering

In analyses performed prior to the existence of the robust model, including the present contribution, the time regimes for which Rayleigh and Thomson scattering were applied could be justified through the criteria that follows. Rayleigh scattering measurements for temperature can begin to be applied at the time when the Thomson scattering signal becomes negligible. We (somewhat crudely) estimate this to be the time at which the central region of the scattering signal begins to rise (due to cooling) rather than continues to fall (due to electron decay).[15] The corresponding time is approximately 7.5 µs for the single pulse NIR plasma, in reasonable agreement with literature.[13] Note that the estimation made here matches our constant pressure assumption regime quite well, and accordingly we use the constant pressure model to estimate temperature at each point. The corresponding (Rayleigh dominated) profile is shown in Fig. 5. At the extended delay times, some interesting hydrodynamic fluid behaviors become apparent. The peaks and dips are thought to be due to kernel vorticity extracting hot fluid from the central region and circulation of this fluid through two adjacent lobes.[2,13] This will be examined with greater detail in Chapter 3 for the REMPI dual-pulse plasma.

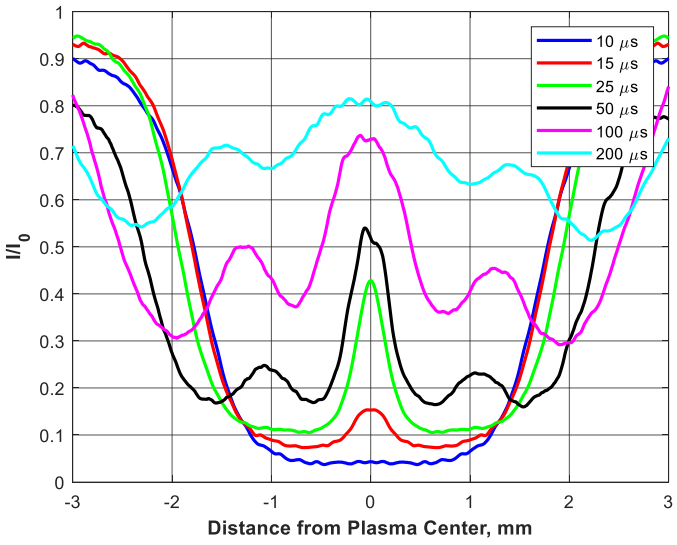

Figure 2.10: The normalized scattering signal at later delays for both NIR (left) and dual-pulse (right) plasmas.

Using normalized intensities presented above and the CP curve shown in Fig. 2.5 we can estimate the pointwise temperature for each pixel location. The resulting temperature measurements, with and without correction for cross-sections, are shown in Fig. 2.11 for NIR and dual-pulse cases. Here, the blue trace represents the measured temperature applying Equation 2.1 while the red trace represents the estimated temperature using the ideal gas relationship while neglecting the temperature dependent cross sections and mole fraction variations. For most of the conditions shown in Fig. 2.5, the corrected temperatures are slightly lower than those without correction. In this range (T < 8500 K), the corrected (species-averaged) cross-section is a bit below the uncorrected value (mostly due to nitrogen dissociation) meaning that, without correction, inferred densities are low, and inferred temperatures a bit high. This is in good agreement with literature.[48] Note that a corresponding ideal gas point is not plotted for the 7.5 µs case, because at this point, the error flips and the ideal gas relationship severely underestimates temperature. This can be seen as the intersection of the red and blue lines in Fig. 2.5 at an actual temperature of ~ 8500 K. We report a maximum gas temperature of 9,400 K at 7.5 µs for the NIR single pulse plasma. It takes the NIR plasma a long time to cool, as it takes more than 100 µs to fall below 1,000 K.

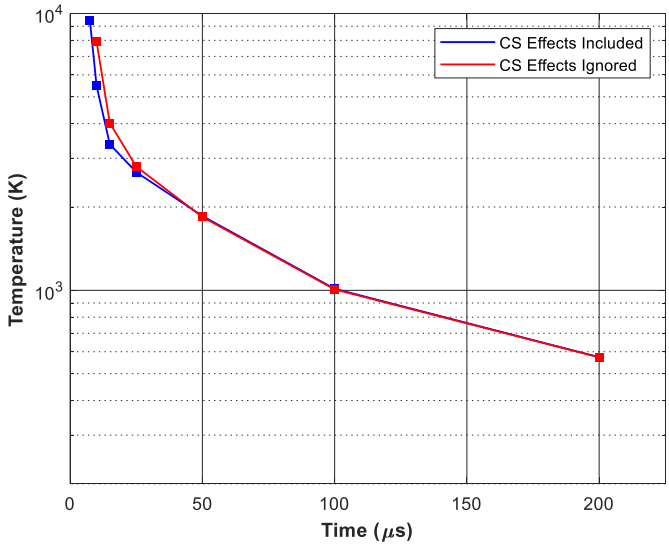

Figure 2.11: Temperature versus time profiles, from Rayleigh scattering, for the NIR single pulse plasma.

2.3.4 Ignition Characteristics

2.3.4.1 Combustion Efficiency

Combustion of methane-air and hydrogen-air mixtures was performed using both single pulse plasmas to supplement past ignition testing in other fuels.[6] We examined equivalence ratios from the stoichiometric case down to the lean limit, with increasing resolution towards the lean limit. The pressure traces presented in Fig. 2.12 show single pulse ignition of methane-air (left) and hydrogen-air (right) mixtures. Time of zero corresponds to the time of laser energy deposition, and the central line of each pressure trace represents the average of at least n=10 individual measurements, while the shaded region represents one standard deviation in either direction of the igniting cases. As expected, we see decreasing peak pressure and increasing ignition delay and variability with increasing equivalence ratio.

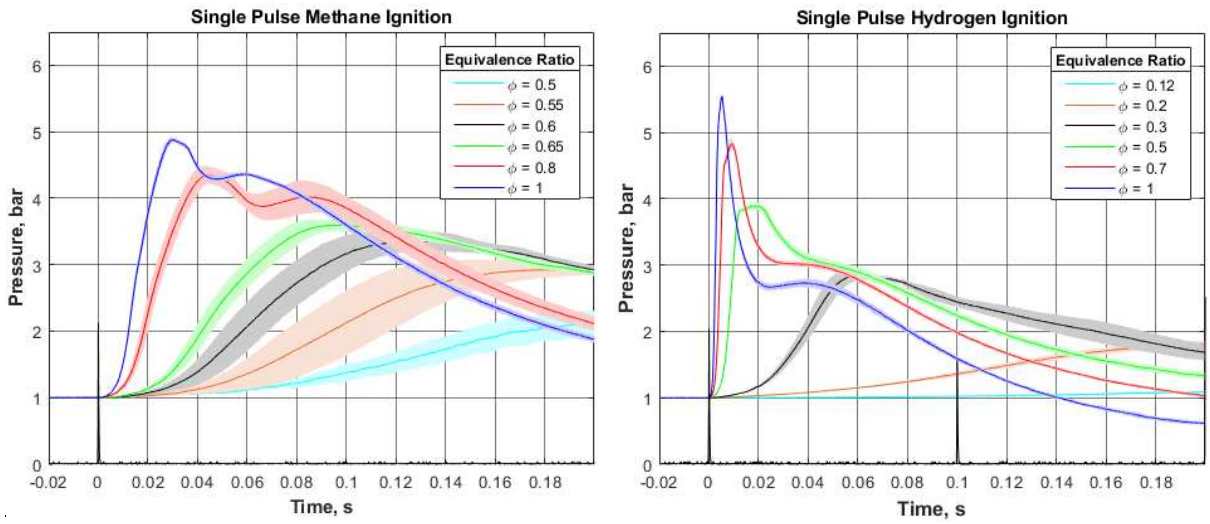

Figure 2.12: Combustion pressure histories for single pulse ignition of methane-air and hydrogen-air mixtures. Each trace is the result of averaging successful ignition events of at least ten trials.

We define successful ignition as any increase in pressure (as monitored by the dynamic pressure transducer) accompanied by simultaneous flame propagation as monitored through OH* chemiluminescence. This definition includes weak and partial combustion events. We define the lean limit as the leanest test case where probability of ignition met or exceeded 50%. Using the pressure traces shown above, we can extract a heat release rate from each ignition event as described in our past work.[6] By comparing to the heating values of the respective fuels, we can calculate the combustion efficiency for each ignition event. The resulting efficiencies are shown in Fig. 2.13 for the single and pulse case and is compared with existing information for propane from literature.[6] The vertical error bars are representative of the standard deviation in efficiency for each equivalence ratio, while horizontal error bars indicate the measurement uncertainty associated with the pressure gauge used to monitor partial pressures. Note that the uncertainty in equivalence ratio varies for each fuel type. The average efficiency value is calculated from the

igniting cases, and excludes unsuccessful ignition events. All cases ignited 100% of the time, unless otherwise marked (shown as fractions of successful ignition events around the lean limit).

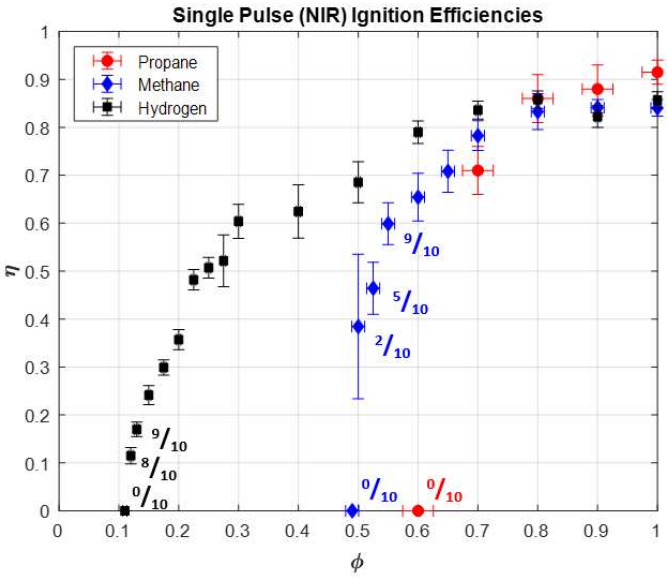

Figure 2.13: Combustion efficiency for propane (red), methane (blue), and hydrogen (black) fuel-air mixtures using single pulse plasmas.

As seen in past experimentation, we observe higher efficiency for lean mixtures, as well as extended lean limits for hydrogen-air when compared with methane-air and propane-air mixtures.[6] Near stoichiometric conditions, we see elevated efficiencies for propane. Based on our definition of the lean limit, we report single pulse NIR lean limits of ϕ=0.12 for hydrogen, ϕ=0.53 for methane, and literature reports a lean limit of ϕ=0.70 for propane.[6]

2.3.4.2 Kernel Shapes from OH Chemiluminescence*

In tandem with ignition experimentation, we imaged the flame front and kernel growth using an intensified charged camera and a λ~310 nm filter corresponding to the emission from the

intermediate OH* radical, known to be a species correlated with regions of heat release.[59–61] This method allows for temporal imaging of the plasma kernel evolution when ignition is repeated and the timing for the gate of the camera is altered. This method works very well when the kernel shape is consistent shot to shot, as is the case near stoichiometric conditions, but becomes difficult near the lean limit, where localized variations in fuel concentrations result in differently shaped flame fronts and flame speeds. For this reason, we tend to look at the kernel shapes near the lean limit independently rather than as a sequence. Fig. 2.14 shows flame kernel development of the single pulse NIR plasma in methane, revealing similar kinds of kernel shapes that are well documented in literature for other fuel-air mixtures.[2,45,62–65] Though this structure is actually an asymmetric torus, it is typically described as a series of lobes because of the shape it takes on when viewed in two dimensions. The toroid is formed by plasma induced hydrodynamics and acts as a driving mechanism through which surrounding gas is entrained and forced through its center.[2,58] The asymmetric torus can be identified in the following images as two vertical side lobes (corresponding to the cross-section image of the torus) and the expelled jet passing through the center of the torus can be identified as the third lobe propagating towards the laser.[6] In this investigation, we see third lobe formation for single pulse methane-air ignition for all equivalence ratios, and separation of the third lobe for mixtures of equivalence ratios of $\phi \leq 0.70$. We also see that near the lean limit, the flame front propagates for hundreds of microseconds, before dissipating or quenching on a several millisecond timescale. Though partial ignition does occur, the flame does not propagate to fill the chamber for some of these leaner mixtures as it does for mixtures of higher equivalence ratios. This result is expected and is similar to single pulse NIR ignition in other fuels.[6] For the flame kernels in Fig. 2.14, the gain for collection was constant, though the images use selective contrast to highlight the kernel shapes. Time delays were selected to match

(as close as possible) the conditions previously published by our group on ignition of propane-air mixtures.[6]

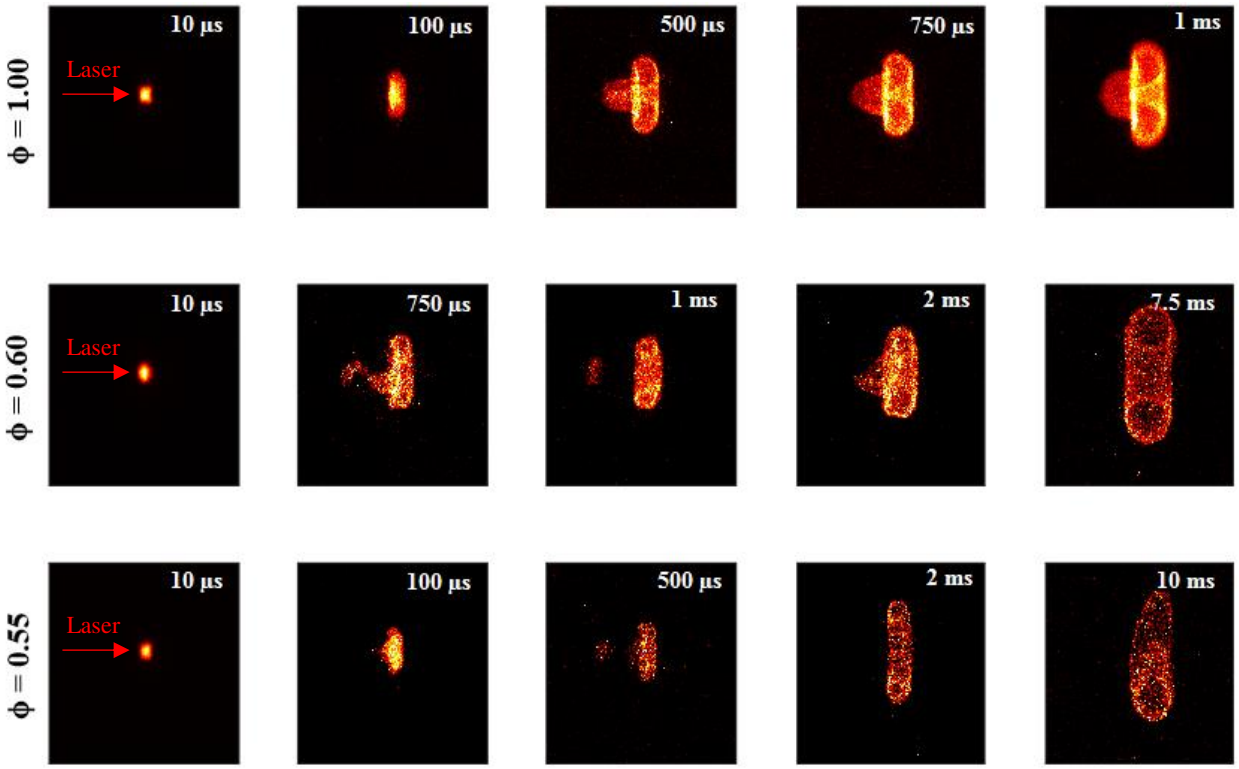

Figure 2.14: Flame propagation for the single pulse NIR plasma in methane-air mixtures at a variety of equivalence ratios. Indicated times are relative to laser energy deposition inside the chamber. Images have physical dimensions of 28 mm x 22 mm in the horizontal and vertical directions, respectively. Note the tendency of the third lobe to form and separate for the leaner cases.

Figure 2.15 details similar flame kernel evolution for single pulse NIR plasmas in hydrogen-air mixtures. Single pulse NIR combustion of hydrogen-air mixtures exhibits distinctly different kernels as compared to methane-air mixtures. Primarily, the timescale for complete combustion was much shorter. The hydrogen-air flame takes around 1 ms to fill the entire frame, while the methane-air flame takes longer than 2.5 ms. More rapid combustion can be expected based on higher predicted flame speeds associated with hydrogen.[66] This can also be seen in the pressure histories of Fig. 2.12. In terms of kernel shape, the main difference compared to methane

is that near stoichiometric conditions we observe highly different flame speeds in the radial and longitudinal (beam propagation) directions. The images show that the kernel expands rapidly over the radial axis when compared with the longitudinal axis. The flame speed of the third lobe is significantly smaller than that of the adjacent toroid, and the result is an ovular shaped kernel and a third lobe that never fully develops. However, we hypothesize that it is possible that the third lobe attempts to form in this near stoichiometric scenario, but is accompanied by large rates of flame strain, resulting in quenching and rapid extinction of this third lobe. As the equivalence ratio decreases, we begin to see the third lobe become more pronounced, which may be due to more uniform flame speeds and reduced strain rate. By ϕ=0.65, we see the third lobe on occasion, at ϕ=0.4 we see it every time, and around ϕ=0.20 we see separation begin to occur. Below ϕ=0.20, we see separation of the third lobe, though there is still enough energy in the independent lobes to sustain combustion in localized regions. This is seen in the bottom right image where a section of the kernel has expanded above the frame and is overlaid with kernels still in the frame (ϕ=0.13, t=25 ms).

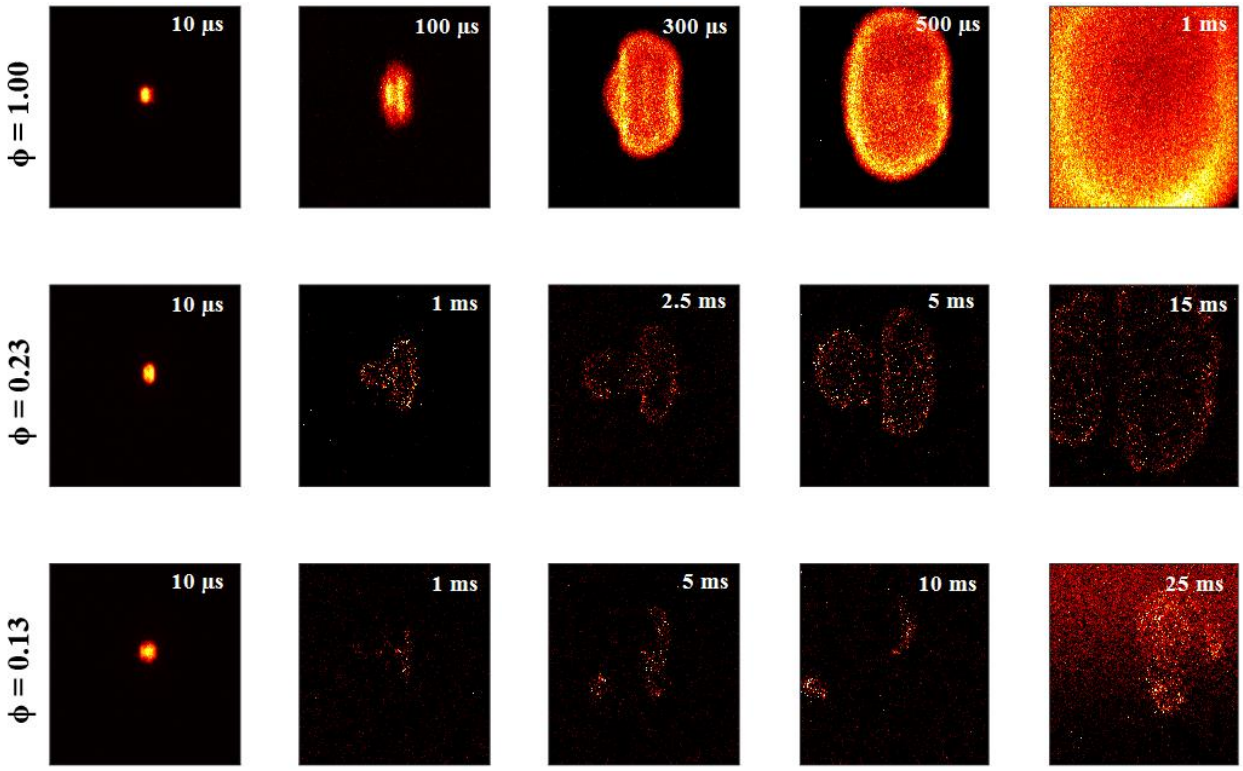

Figure 2.15: Flame propagation for the single pulse NIR plasma in hydrogen-air mixtures at a variety of equivalence ratios. Indicated times are relative to laser energy deposition inside the chamber. Images have physical dimensions of 28 mm x 22 mm in the horizontal and vertical directions, respectively. Note the ovular shape of the kernel as well as the segmentation that takes place for leaner mixtures, resulting in localized ignition events.

2.4 Dual Pulse Plasma

This section characterizes the properties of dual-pulse nanosecond laser plasmas and examines their ability to ignite fuel-air mixtures. The dual-pulse plasma is generated using a UV pre-ionization pulse (λ=266 nm) of energy E_{UV}=20 mJ, followed by an NIR pulse (λ=1064 nm) of energy E_{NIR}=40 mJ delivered 15 ns after the first pulse. Rayleigh and Thomson scattering diagnostics are performed for dual-pulse plasmas in air (T_0=298 K, P_0=1 bar) to measure electron density and gas temperature over a timescale of 200 ns to 200 µs after initial plasma formation. We report a dual-pulse electron density of n_e=4.0-5.9x10^{17} cm^{-3} at time of 200 ns after the initial pulse, and a gas temperature of 1360 K at time of 10 µs, using Thomson and Rayleigh scattering

techniques respectively. Temporal profiles of electron density exhibit similar trends to single pulse NIR plasmas, while temperature profiles indicate much more rapid gas cooling for the dual-pulse plasma. Dual-pulse laser ignition was studied in non-flowing propane-air, methane-air, and hydrogen-air mixtures (P_0=1 bar and T_0=323 K) yielding lean limits of ϕ=0.60, ϕ=0.50, and ϕ=0.11 for dual-pulse ignition of propane-air, methane-air and hydrogen-air mixtures, respectively. This is an extension from the single pulse lean limits mentioned previously. OH* chemiluminescence shows that dual-pulse toroid shapes in propane-air and methane-air mixtures consistently suppress third lobe formation near stoichiometric conditions, but that hydrogen-air mixtures tend to suppress third lobe development over a larger range of equivalence ratios. An investigation of dual-pulse beam axial offset effects demonstrates that downstream focusing of the energy addition pulse relative to the preionization pulse more effectively suppresses third lobe formation than upstream focusing. We also note that upstream focusing of the energy addition pulse near stoichiometric conditions can result in a fourth lobe centered around the preionization channel, and that for small axial offsets ($\Delta z \leq 0.5$ mm), variability exists in the direction of flame propagation. In terms of ignition, we show that for axial offsets above 2 mm no significant benefits (in terms of lean limit extension) are observed. Finally, the main finding of this study is that ignition probability using the dual-pulse non-resonant method is a strong function of axial offset and that downstream focusing of the energy addition pulse is preferable to upstream focusing.

2.4.1 Confirmation of Non-Resonance

The goal of this investigation is to develop a dual-pulse plasma with a non-resonant preionization pulse. To confirm that the ionization mechanism for the UV preionization pulse employed in the dual-pulse scheme is non-resonant, we determine the dependence of the electron

density on the laser energy using optical emission as a proxy signal. Specifically, for non-resonant MPI, given the 266 nm wavelength and the ionization energy of air (mainly consisting of molecular nitrogen), one expects a cubic dependence of electron density on laser fluence (3 photons are required for ionization).[15,18] The dependence of optical emission (obtained 200 ns after the UV pulse for shutter duration 25 ns, without spectral filtering) on the UV laser pulse energy is shown in Fig. 2.16. The emission data is well fit with a third order polynomial which supports that ionization is predominantly by non-resonant MPI. For example, for a 2+1 resonant scenario, one expects a better fit with a second order polynomial, as the simultaneous absorption of the first two photons is the rate limiting step. It is assumed that once the electron has been excited to this higher energy state, it takes little laser fluence to ionize, and therefore ionization is only related to laser energy by the first step. However, it is recognized that optical emission is not a perfect proxy for electron generation, and future efforts include similar measurements (versus laser energy) with Thomson scattering.[57]

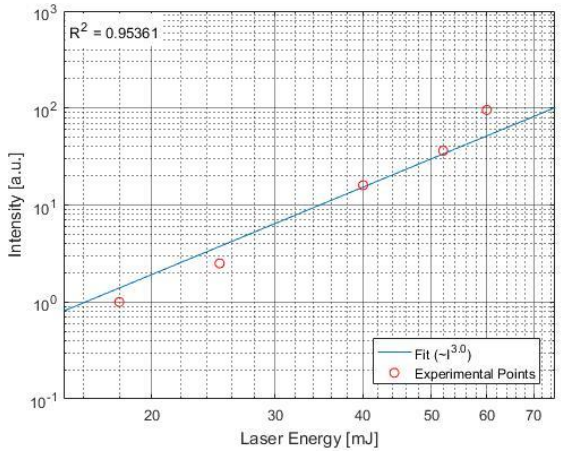

Figure 2.16: Optical emission intensity of the UV plasma as a function of the laser energy. Images were taken at a delay of 200 ns after plasma formation (first pulse). A cubic fit has been applied to the data to verify the ionization method.

2.4.2 Electron Density Measurements by Thomson Scattering

Using the same techniques outlined in section 2.3.1, we employ combined Rayleigh Thomson scattering. The normalized intensities are plotted in Fig. 2.17 below, showing the result of plasma and background subtraction, the addition of dark counts, and the normalization to the reference condition in accordance with the left side of Equation 2.1.

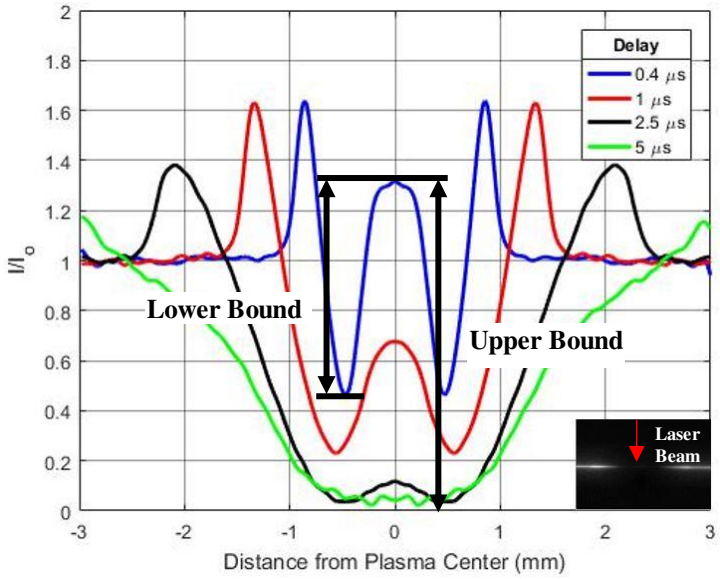

Figure 2.17: Rayleigh scattering signal along the transverse axis of the plasma for a non-resonant dual-pulse laser plasma. The signal has been normalized by the intensity of the scattering beam. The rise of central portion of the signal is due to Thomson scattering. The insert in the bottom right details the raw ICCD images at a delay of 2.5 μs. The plasma formation laser enters from the top of the image.

Using the same bounding technique detailed in section 2.3.1, we find a similar electron density profile for the dual-pulse case when compared with the single pulse NIR case, with a peak value of n_e~5.0x10^{17} cm^{-3} measured for the dual-pulse at delay of 200 ns after plasma formation.

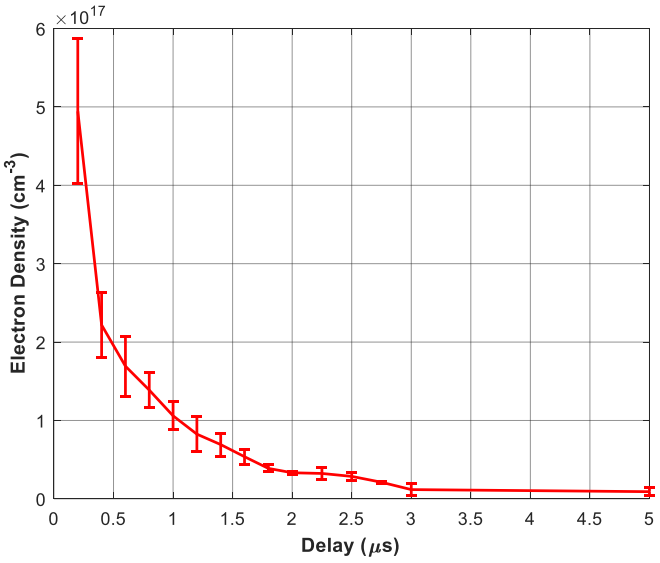

Figure 2.18: Electron density decay for the dual-pulse plasma as a function of time.

2.4.3 Temperature Measurements by Rayleigh Scattering

Applying the same diagnostic at later delays, we can extract information about the temperature of the plasma. We assume the constant pressure assumption and scattering model to be valid at delays greater than 7.5 µs, and estimate temperature accordingly. The validity of this assumption is evaluated in section 2.3.2. Instead of evaluating temperatures out to extremely late delays, we wait until we see the baseline rise to approximately match the reference condition, and terminate measurements there. Again, we apply measurements for both the modeled CP scenario (shown in blue), as well as the measurements that would be assumed had the simple ideal gas relationship been applied (shown in red). We see that the two converge vary quickly. The normalized scattering signal and corresponding temperature measurements are shown in Fig. 2.19, below.

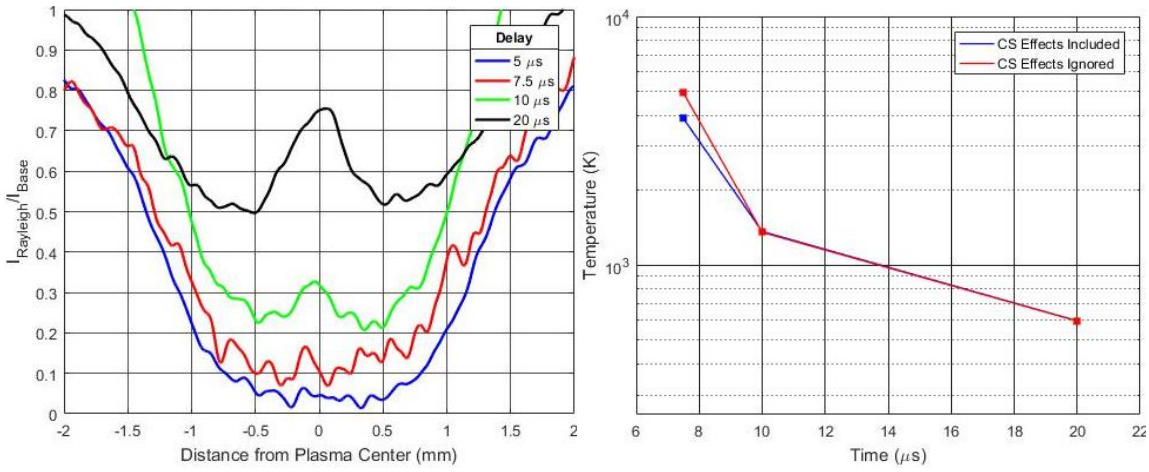

Figure 2.19: The normalized scattering signal at later delays for the non-resonant dual-pulse plasma (left), and corresponding maximum temperature measurements made using the equilibrium constant pressure model outlined in section 2.2.1 (right).

Comparing this result to the non-resonant single pulse plasma detailed in the previous section, we see that the dual-pulse plasma cools much more rapidly than its NIR counterpart. It takes approximately 10 μs for the dual-pulse plasma to reach 1,000 K, while it takes the NIR plasma more than 100 μs. These findings warrant further investigation and we note there is an additional experimental uncertainty (~30%) present in the reported measurements due to jitter in the timing of the probe laser beam that affects its overlap with the gated detection period of the intensified camera.

2.4.4 Ignition Characteristics

2.4.4.1 Combustion Efficiency

Dual-pulse ignition was performed in the same fuels as single pulse (propane, methane, and hydrogen) for equivalence ratios corresponding to ϕ=0.1-1.0. The pressure histories, due to heat release, from ignition events at each equivalence ratio were recorded using an oscilloscope

and dynamic pressure transducer as described in Section 2.3.4. The results were then averaged (n>=5 replicates per condition for propane, n>=10 replicates per condition for methane and hydrogen), and are shown in Fig. 2.20.

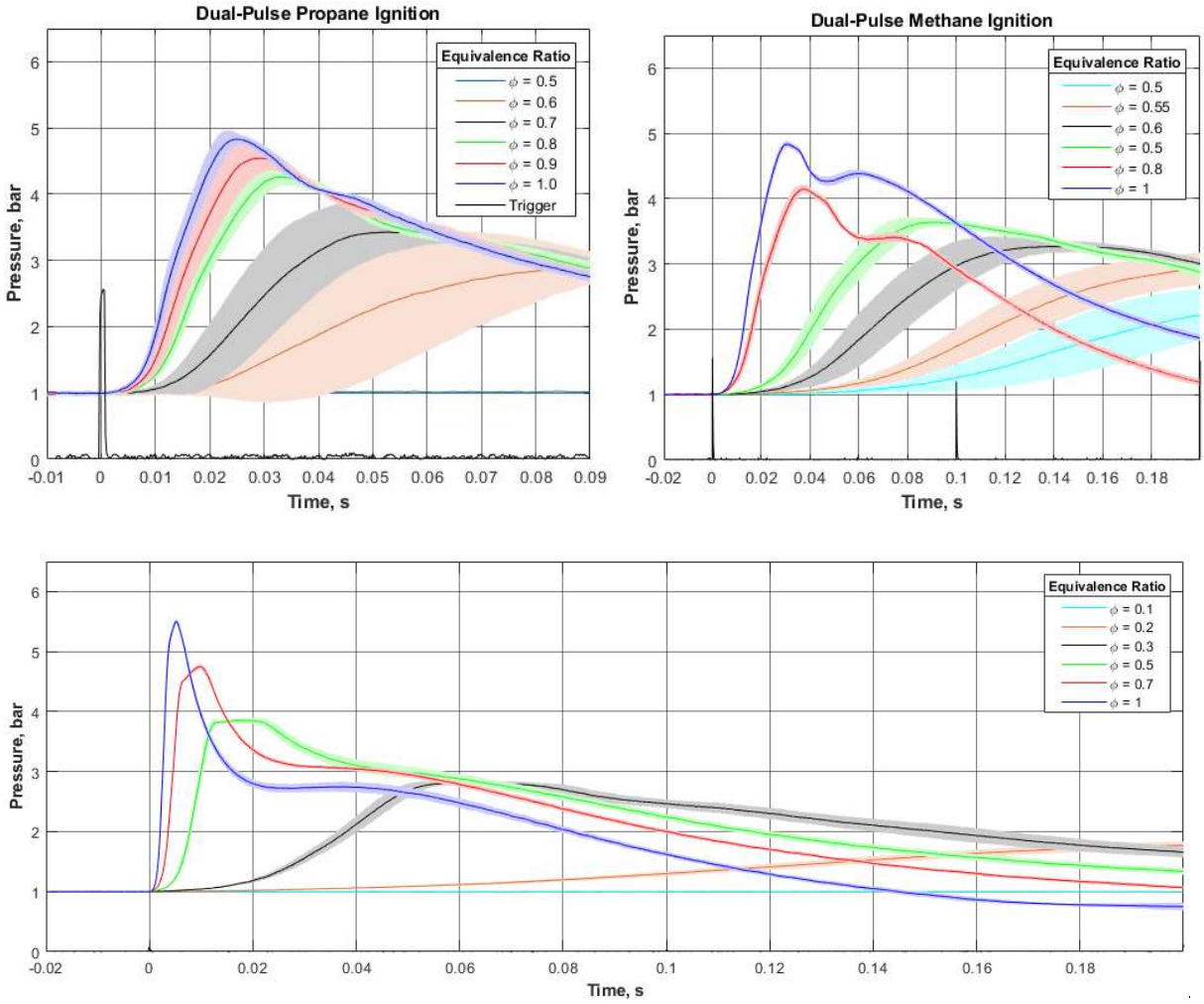

Figure 2.20: Recorded pressure traces at varying equivalence ratios for methane (left) and propane (right). The dual-pulse scheme uses E_{UV}=20 mJ and E_{NIR}=40 mJ. The standard deviation of the multiple traces for each condition is plotted as the shaded region. Initial conditions were P_0=1 bar and T_0=323 K.

The heat release of the ignition event can be calculated through integration of the pressure history and addition of estimated heat loss to the wall, calculated through estimation of the slope after the ignition event has occurred. Fuel energies are calculated using the lower heating value

(LHV) and mass as calculated from the partial pressure. Combustion efficiency is then the ratio of the heat release to the internal energy of the fuel. Resulting efficiencies are shown in Fig. 2.21.

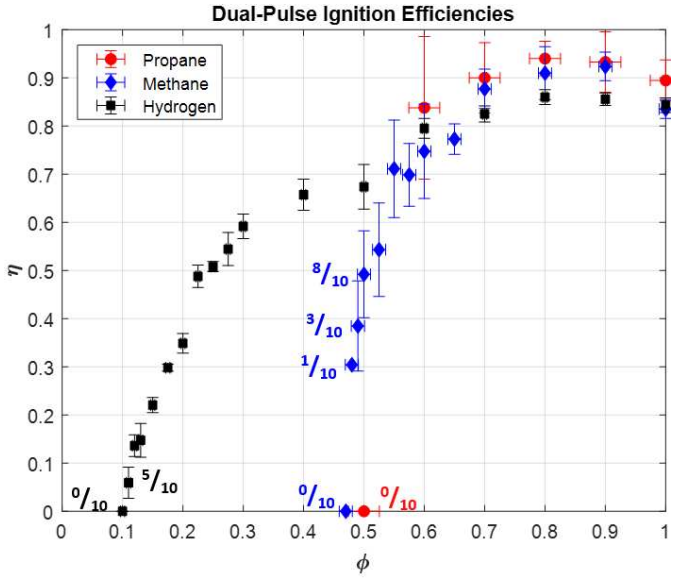

Figure 2.21: Combustion efficiency for ignition of propane-air, methane-air, and hydrogen-air mixtures by dual-pulse laser ignition. Each data point is the average of at least five traces for propane, and ten for methane and hydrogen, where the vertical error bars represent one standard deviation in each direction and the horizontal error bars show uncertainty in partial pressure measurements.

For the dual-pulse plasma, we report lean limits of ϕ=0.11 for hydrogen, ϕ=0.50 for methane, and ϕ=0.60 for propane. We find that the dual-pulse plasma results in extension of the lean limit for each fuel type relative to single-pulse (with the same total incident energy). We note the most significant difference for propane, though the resolution ($\Delta\phi$=0.1) in equivalence ratio from previous experimentation of single pulse ignition could be improved.[6] In terms of efficiency, we report generally higher efficiency ignition for the dual-pulse plasma in both methane-air and hydrogen-air mixtures when compared with single pulse NIR ignition, though the result is seen for nearly all equivalence ratios in the methane-air case while only for the particularly lean cases for hydrogen-air mixtures.

2.4.4.2 Kernel Shapes from OH Chemiluminescence*

Using the same techniques presented above for the single pulse NIR plasma and kernel, we analyze the dual-pulse plasma for ignition in both methane-air and hydrogen-air mixtures. We see that in both fuel-air mixtures, for all equivalence ratios, the dual-pulse plasma kernel exhibits the characteristic shape of a preionization channel and a larger energy addition kernel over the range of tens of microseconds.[6] Fig. 2.22 shows methane-air ignition. For equivalence ratios in the range ϕ=1.0-0.70 the energy deposition profile suppresses the development of the third lobe. For the stoichiometric case, the direction of plasma propagation (or the direction in which the third lobe would form if it did) is unpredictable. As mentioned earlier, each image represents a separate ignition event, so that each image should be evaluated individually rather than as a sequence. In eleven combustion events, we report that five of these kernels propagated towards the laser beam, while four propagated away (two were indeterminable). We attribute this to the axial overlap of the two beams, and believe that variability in propagation direction is indicative of good overlap (Δz=0), which leads to suppression of the third lobe. This is studied more rigorously in the offset investigation to follow. Below ϕ=0.7, despite successful overlap, the third lobe is formed, but it takes a long time to develop (tens of ms), which may explain why this result was not reported on in the past for propane-air mixtures.[6] Around ϕ=0.55, we observe third lobe detachment, kernel segmenting and extinction, and localized kernels which then propagate towards a complete ignition event.

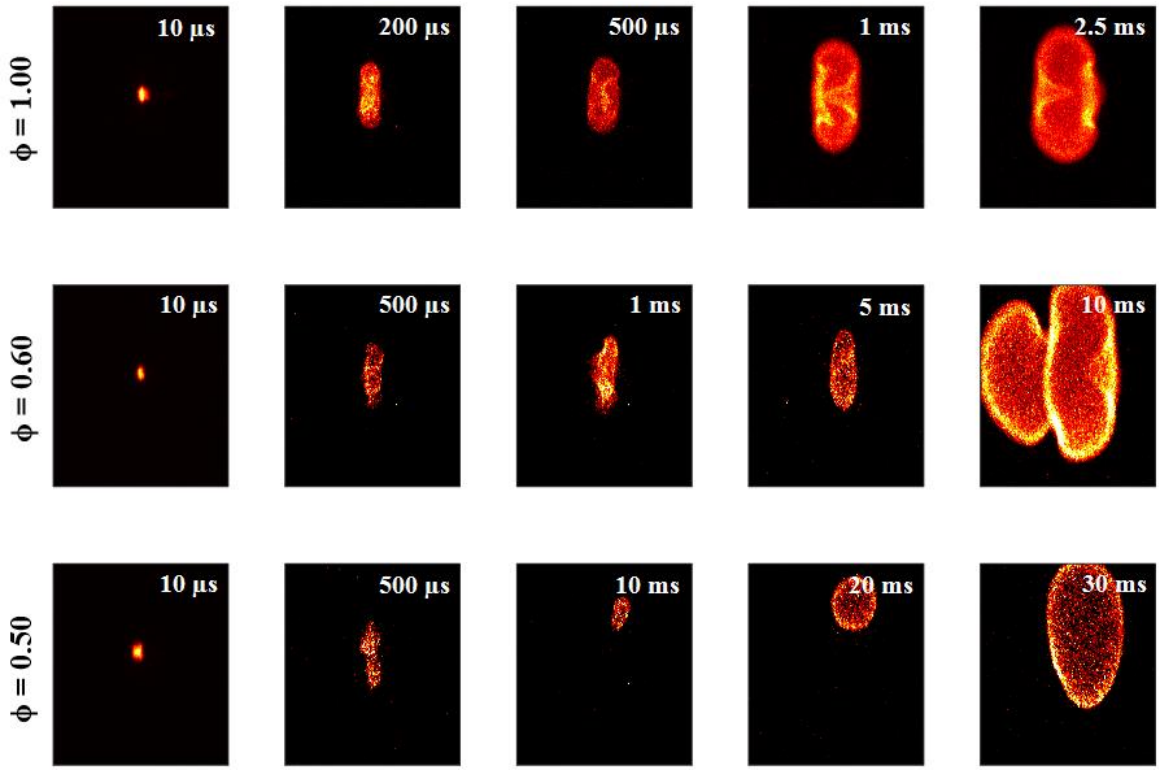

Figure 2.22: Flame propagation for the dual-pulse plasma in methane-air mixtures at a variety of equivalence ratios. Indicated times are relative to laser energy deposition inside the chamber. Images have physical dimensions of 28 mm x 22 mm in the horizontal and vertical directions, respectively. Note the non-existence of the third lobe for the stoichiometric case. Additionally note the timescale over which the third lobe is seen for the intermediate equivalence ratios and the localized combustion that occurs near the lean limit.

Much like the single pulse NIR plasma, kernel shapes for dual-pulse ignition of hydrogen-air mixtures were much different compared to those formed in methane air mixtures, likely due to fuel reactivity. Again, for all equivalence ratios, the dual-pulse plasma kernel exhibits a distinct preionization channel and energy addition kernel over the first few microseconds. For equivalence ratios in the range ϕ=1.0-0.5, the dual-pulse plasma kernel propagates with this characteristic cross shape all the way through the ignition process. Though this occurs for all equivalence ratios in this range, it is most visible for the ϕ=0.9 case. Below ϕ=0.5, the third lobe is formed, as a net central fluid flow is developed in the center of the toroid, forcing the third lobe in the direction of laser incidence. Around ϕ=0.2, we see segmenting and separation in the kernels, and near the limit we see localized pockets of ignition similar to those seen for single pulse ignition.

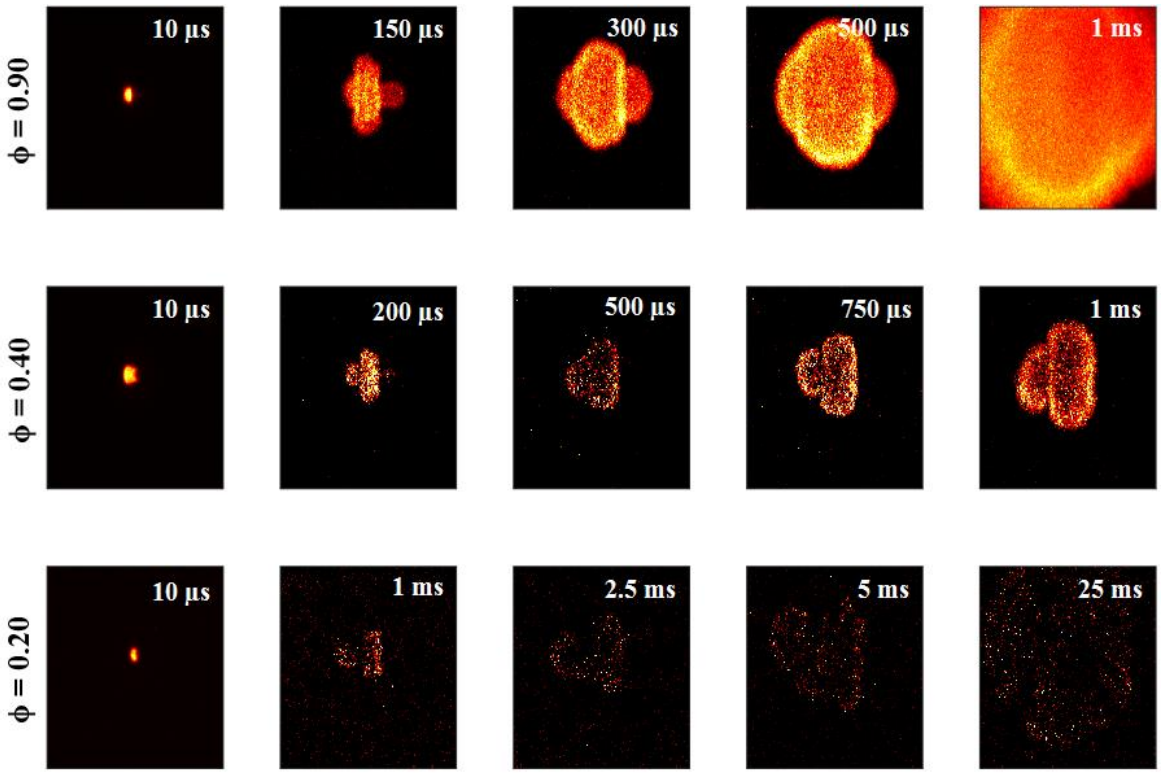

Figure 2.23: Flame propagation for the dual-pulse plasma in hydrogen-air mixtures at a variety of equivalence ratios. Indicated times are relative to laser energy deposition inside the chamber. Images have physical dimensions of 28 mm x 22 mm in the horizontal and vertical directions, respectively. Note the unique cross shaped kernel for the stoichiometric case.

2.4.4.3 Investigation of Axial Offset on Dual-Pulse Ignition

Previous work in our group has demonstrated that dual-pulse plasma kernel dynamics in propane-air mixtures are a strong function of the energy deposition profile, i.e. the focusing conditions and axial overlap of the two pulses.[6] The previous section demonstrated that third lobe formation can be inhibited near stoichiometric conditions for both methane-air and hydrogen-air mixtures. In order to better characterize this effect and the impacts of deviation from perfect overlap, a test space consisting of a series of axial offsets (Δz = -5.0, -2.0, -0.5, 0.0, +0.5, +2.0, +5.0 mm) and equivalence ratios (ϕ=0.50, 0.60, 0.80, 1.00) was developed. Example axial offsets are shown in Fig. 2.24 where a negative axial offset corresponds to the energy addition pulse (NIR)

focusing upstream of the preionization pulse (UV) and vice versa. In practice, this is done by fixing the location of the UV beam, while moving the focus of the NIR beam via a translation stage on which the lens is mounted.[10]

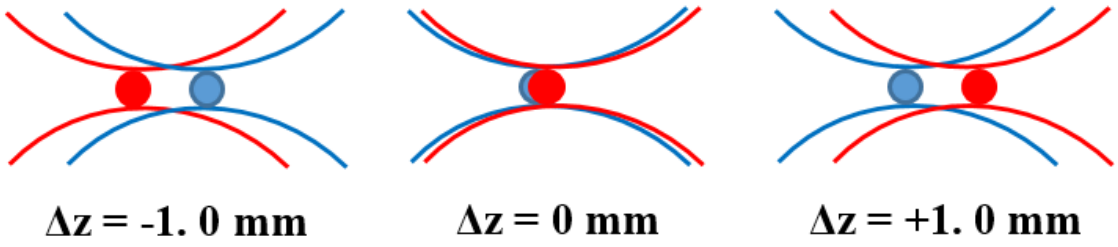

Figure 2.24: Example axial offsets where the red trace represents the focusing of the energy addition (NIR) beam, and the blue trace represents the focusing conditions of the preionization (UV) beam. The zero offset case is slightly shifted for visualization.

For each combination of axial offset and equivalence ratio, at least three combustion events were attempted, though for the zero offset case at least ten combustion events were averaged as described in the section 2.4.4.1. The absolute limit to ignition was also determined as the minimum equivalence ratio for which at least one of the ignition attempts resulted in combustion of the fuel mixture. Experiments were performed in methane-air mixtures. Fig. 2.25 shows the effects of offset variability on kernel shapes, where each image is taken at a time of t=1 ms after laser energy deposition using an exposure value of Δt=500 μs. In these images, the laser beam enters from the left. Neither beam has sufficient energy to generate full breakdown (and ignition) independently, and therefore each flame kernel can be considered a dual-pulse flame kernel. Note that the lean scenario (shown in the top row of Fig. 2.25) varied with the offset in order to be able to obtain a successful ignition event. Within Δz = ±0.5 mm, this lean scenario corresponded to an equivalence ratio of ϕ=0.50, but outside this offset, the lean scenario corresponded to ϕ=0.53.

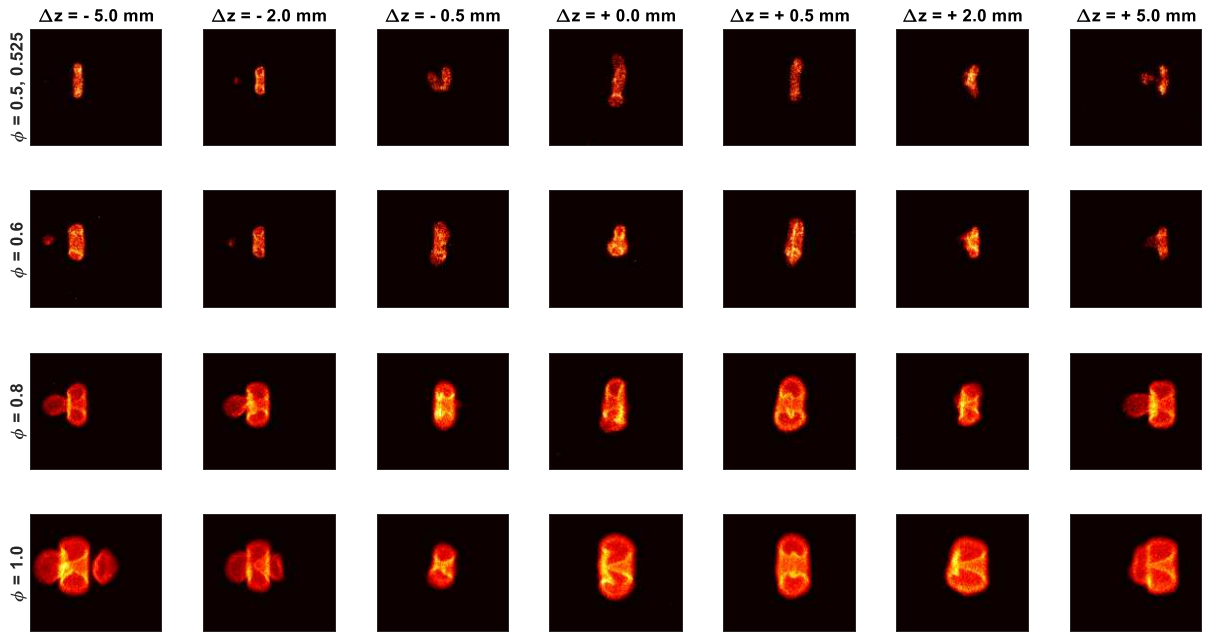

Figure 2.25: Flame kernel shapes from the dual-pulse plasma in methane-air mixtures at a variety of equivalence ratios and offset conditions. Each image is taken at a time of t=1 ms using an exposure of Δt=500 μs. Images have physical dimensions of 28 mm x 22 mm in the horizontal and vertical directions, respectively.

The cases for which the energy addition pulse is focused upstream of the preionization pulse tend to exhibit higher longitudinal flame speeds for the third lobe, resulting in much more common third lobe detachment than equal axial offsets that focus downstream of the preionization pulse. We hypothesize to this be to be due to the free electron densities along the longitudinal axis, and the corresponding MPI/EAI electron production proportions for each beam.[13] For the upstream case (negative axial offsets), the energy addition beam has not passed through an electron dense region when it reaches its focal point. Though some of the pulse energy gets absorbed by free electrons downstream of the focal point, the proportion of energy that reaches these free electrons is smaller, and the plasma tends to develop as if it were a single pulse plasma, where the energy addition pulse becomes responsible for both MPI and EAI. An interesting phenomenon is observed for the negative axial offset at the stoichiometric condition, where a "fourth lobe" is developed

near the location of preionization focus. This suggests that in these conditions, sufficient energy deposition occurs downstream of the focal point in the preionization channel to develop another lobe. Much like the third lobe, this lobe is susceptible to separation from the main toroid, as is seen in the extreme offset case of Δz=-5.0 mm.

The cases where the energy addition pulse is downstream of the preionization pulse tend to have less flame stretching of the third lobe, and separation occurs less frequently. We hypothesize this to be due to better inverse bremsstrahlung absorption of the energy addition pulse, which in this case has to completely pass through the preionization channel before it reaches its focal point. This results in better absorption of the energy addition pulse, as it is responsible for a much smaller proportion of MPI and contributes mainly to EAI, developing kernel shapes that better suppress the third lobe. We also see in Fig. 2.25 that the overlap precision is difficult to discern by simply looking at kernel shapes. As mentioned before, for the zero offset case, we see that the flame growth is unpredictable, sometimes occurring upstream and sometimes occurring downstream (seen in the first row of Fig. 2.22 and described in section 2.4.4.2). We see that within the range of $\Delta z \leq 0.5$ mm, this trend continues. Somewhere between 0.5 mm and 2 mm, this variability breaks down and the three lobe structure grows towards the laser for every ignition test.

In conjunction with imaging, pressure histories were collected so that efficiencies could be calculated. For each condition, three combustion events were attempted, and successful events were averaged. The resulting combustion efficiencies as a function of offset and equivalence ratio are shown in Fig. 2.26 (left). The zero offset case has increased combustion efficiency for nearly all equivalence ratios, though no observable trend exists for the other offsets at equivalence ratios far from the lean limit. Near the lean limit, the closer the axial offset to the zero offset case, the further the absolute ignition limit was extended. For the zero offset case, the absolute ignition limit

was ϕ=0.48. For an axial offset of Δz=0.5 mm in either direction, the absolute ignition limit was found to be ϕ=0.50. Once the axial offset reached Δz=2.0 mm, the absolute ignition limit was ϕ=0.53. This matches the lean limit of single pulse ignition. Therefore, we conclude that in order to benefit from dual-pulse ignition lean limit extension, the axial offset between waists must be less than 2 mm, though the range of acceptable offsets is likely much smaller and further investigation is warranted.

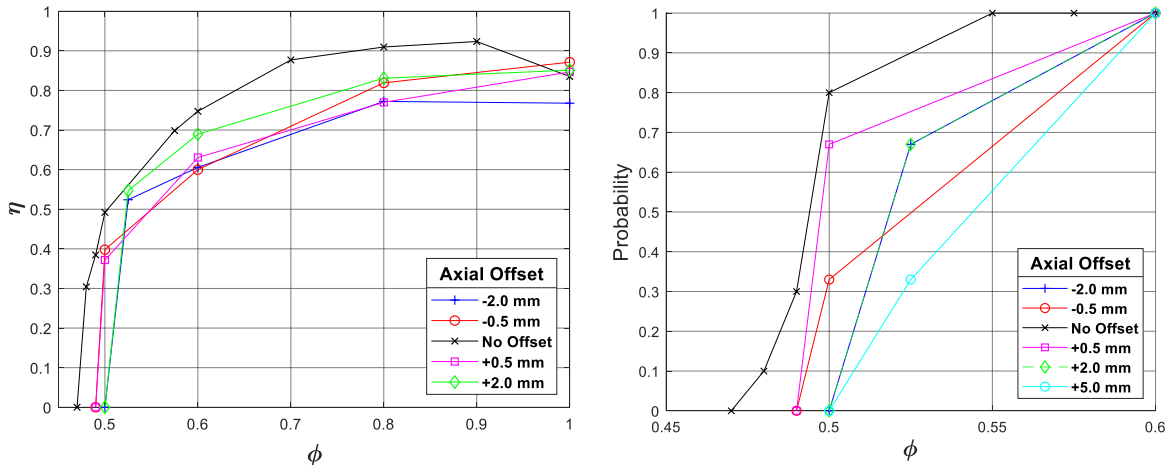

Figure 2.26: Combustion efficiency (left) and ignition probability (right) for a variety of axial offsets and equivalence ratios. Each point represents the average of at least three ignition attempts. Note the decreasing efficiency with increasing offset distance. Also note how increasing axial offset results in decreasing probability of ignition and how the -0.5 mm case has higher probability of ignition that the +0.5 mm case, attributed to better suppression of the third lobe seen in the OH* chemiluminescence images.

It is also informative to look at the probabilities of ignition as a function of offset. The measured probabilities of ignition are shown in Fig. 2.26 (right). The limited resolution step size in equivalence ratio inhibits our ability to draw thorough conclusions though we do note some important trends. We see that the probability of ignition increases with better overlap precision. Additionally, we notice an increase in probability for the downstream focusing condition when compared with the upstream condition at Δz=0.5 mm. We attribute this to the better suppression

of third lobe as commented upon in the OH* chemiluminescence section of the offset investigation. Recall that this third lobe is known to transport heat and intermediate species away from the kernel, so suppression of it results in more stable combustion, therefore increasing the probability of ignition.

CHAPTER 3:

Resonant Plasma Properties and Ignition Characteristics[3]

3.1 Introduction

The two ionization methods involved in our dual-pulse plasma formation with nanosecond lasers are multiphoton ionization (MPI) and electron avalanche ionization (EAI). During MPI in the preionization step, incident laser photon energy is quasi-simultaneously absorbed by gas molecules, exciting electrons beyond the ionization threshold. Free electrons generated in this manner are then accelerated by the second laser pulse and collide with heavier charged particles. Inverse bremsstrahlung absorption leads to electron avalanche ionization (EAI) and full breakdown. During MPI, incident photons arrive or collide with molecules at discrete times, successively increasing the virtual energy state of an electron. However, as defined by the Heisenberg uncertainty principle, there is a limited time frame in which an electron can stay in an elevated virtual state.[18] As the magnitude of the virtual energy level increases, the electron becomes increasingly unstable, and the time frame that an electron can remain in that state significantly decreases. For a given ionization step, the MPI rate is maximized when fewer photons are required corresponding to lower optical wavelengths (higher energy photons). On the other hand, rates for inverse bremsstrahlung increase with longer optical wavelengths.[13] Accordingly,

[3] This chapter makes conclusions and near complete references to the following conference proceedings: (3) Dumitrache C., Butte C., Eickelberg A. and Yalin A., "On the Use of REMPI Pre-ionization for Laser Plasma Formation," 2018 AIAA Aerospace Sciences Meeting, AIAA SciTech Forum, 2018. and (4) Butte C., Dumitrache C., and Yalin A., "Dual-Pulse Laser Ignition Using Oxygen REMPI Preionization," 2019 AIAA Aerospace Sciences Meeting, AIAA Aviation Forum, 2019. For (4), my contribution was to collect all data and write the manuscript. For (3), my focus was data collection.

our previous dual-pulse plasma formation has generally used λ=266 nm preionization pulse for MPI, and a second λ=1064 nm pulse for energy addition and EAI. The two pulses are separated by a time of t =15 ns. While the 266 nm is attractive since it is in the UV (and is the 4th harmonic of Nd:YAG) it is not resonant with absorbing molecules.

Striving for more energetically efficient mechanisms, we have investigated the possibility of replacing the preionization leg with a resonant preionization technique which targets an electronic transition of an oxidizing molecule. We target the $C^3\Pi_g$ (v'=2) ←$X^3\Sigma_g^-$ (v''=0) transition of molecular oxygen using a 2+1 REMPI scheme centered around 287.5 nm.[57,67–69] Two photons are required to excite an electron to this energetic state, and one further photon is required to raise it above the ionization threshold. The aforementioned energy level is much more stable than the virtual levels that are used for non-resonant ionization, making ionization much more probable and frequent. The approach can allow more efficient coupling of laser energy into ionization of electrons and less into loss mechanisms.

3.2 Single Pulse REMPI Pre-Ionization

3.2.1 Introduction

This section of the thesis present contribution examines the potential of using resonant enhanced multi-photon ionization (REMPI) as source of pre-ionization in a dual-pulse laser ignition scheme. In particular, we investigate the plasma properties of a 2+1 REMPI scheme for O_2 centered around λ=287.5 nm.[67,68] The motivation is to improve a previously developed dual-pulse laser ignition technique in which a non-resonant ultraviolet (UV) pulse (λ=266 nm) is used to preionize the fuel-air mixture followed by a near-infrared (NIR) pulse (λ=1064 nm) to add energy until the temperature is high enough to allow ignition. The REMPI scheme described here

could replace the first UV pre-ionization pulse. To confirm the presence of REMPI we present rotationally resolved spectra for the two-photon excitation of the $C^3\Pi_g\,(v' = 2) \leftarrow X^3\Sigma_g^-\,(v'' = 0)$ transition in pure oxygen using laser Thomson scattering. The plasma temperature and electron number density are determined and compared with the results from the previously used pre-ionization scheme at λ=266 nm. We report an O_2 REMPI plasma density of n_e=1.3– 3.7 x 10^{17} cm^{-3} (at p_0=1 bar, T_0~300 K) for a laser pulse energy of E_{REMPI}=3 mJ. The gas temperature at time 0.6 μs after plasma formation was determined to be T=530 K ± 3 K. In contrast, no plasma was formed at these conditions with the previous preionization scheme (λ=266 nm). The findings are relevant for the development of dual-pulse schemes for laser ignition since the O_2 REMPI plasma allows for more efficient gas preionization with smaller energy requirements than the previous 266 nm wavelength.

3.2.2 Theory

The 2+1 REMPI scheme for O_2 can be described as follows (see Fig. 3.1): a two-photon transition excites the molecules from the ground state O_2 ($X^3\Sigma$, v=0) to the excited state O_2 ($C^3\Pi$, v=2). From this excited state, the absorption of a third photon promotes the molecule above the ionization threshold leading to the formation of a free electron and a molecular oxygen ion in the ground state O_2^+($X^2\Pi$). It is worth mentioning that as part of this study a large wavelength interval was probed starting from λ=266 to λ=289 nm. This wavelength region contains the previously used pre-ionization wavelength (266 nm), several 2+2 and 3+1 N_2 REMPI schemes (at 283.1 nm and 285.6 nm respectively[17,70]) as well as the 2+1 O_2 REMPI scheme that makes the main topic of this work. However, no plasma has been observed at 266 nm and negligible fluorescence (most likely from the N_2^+(B) state), below our Thomson detection limit, has been observed at the N_2

REMPI wavelengths. Consequently, the experiments described here focus exclusively on the 2+1 O_2 REMPI scheme which was experimentally observed to be the strongest at our conditions.

The REMPI generated plasma did not present any visible emission (by eye) at the conditions studied here. Instead, laser induced Thomson and Rayleigh scattering were used for detecting the plasma formation and determining the plasma properties (electron number density and plasma temperature). Rayleigh scattering is an elastic scattering process from gas molecules that produces a signal proportional to gas density.[71,72] Temperature can be inferred from density (using the ideal gas law) by essentially dividing the Rayleigh signal from the plasma by a Rayleigh signal at reference conditions. This approach to Rayleigh thermometry requires background subtraction, uniform pressure and composition.[13] On the other hand, Thomson scattering is a process involving free electrons inside the plasma. Electron number density estimations can be obtained by normalizing the Thomson signal inside the plasma by the reference Rayleigh signal in the absence of the plasma. As such, both experiments require the same experimental setup with the observation that Thomson measurements are performed at early times (first few hundred of nanoseconds) when the scattering signal is predominantly coming from the plasma. Rayleigh thermometry measurements are performed at later times (~1 μs and later) on the remaining hot gas after plasma recombination.

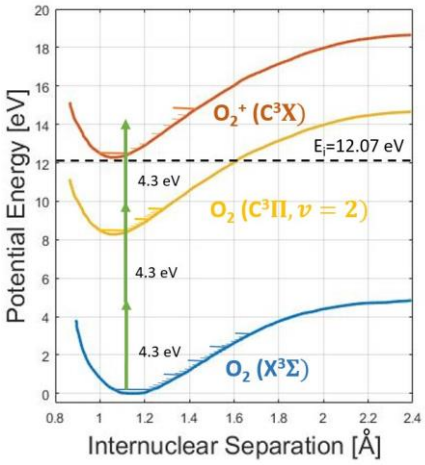

Figure 3.1: Potential energy diagram showing the energy levels involved in the O_2 2+1 REMPI scheme.

3.2.3 Experimental Setup

The optical layout used for the experiments described in this manuscript is presented in Fig. 3.2 below. The third harmonic of an Nd:YAG laser (Continuum Powerlite 8010) at λ=355 nm is used to pump an optical parametric oscillator, OPO (Sunlite EX). The OPO allows one to access a broad range of wavelengths (λ=445−1750 nm) with an output power of E ~ 30 mJ. The output from the OPO is subsequently passed through a frequency doubler (Continuum FX-1) in order to reach to UV wavelength interval that is of interest in this study (λ=266−289 nm). The REMPI beam was focused inside of a pressure cell filled with pure oxygen using a plano-convex lens with a focal lens of f=100 mm. The focal spot size was estimated to be ~150 µm (for a beam quality factor: M^2~5).

Rayleigh and Thomson scattering line (1-D) measurements were performed using another Nd:YAG laser (Spectra Physics Quanta Ray) operating at the second harmonic (λ=532 nm). The probe beam was brought inside the chamber using a pair of dielectric mirrors and focused perpendicular to the interrogation region using a plano-convex lens (f=250 mm). In order to get maximum scattering signals, the polarization of the 532 nm beam was set to S-polarization. The

scattering photons were collected using an ICCD camera (pco DICAM pro) from a plane above the plasma kernel using an f/3.0 lens. Due to the very low S/N ratio characteristic to unfiltered Rayleigh scattering, shielding from the elastically scattered photons inside the chamber was provided by installing baffles across the length of the chamber. To determine temperature from the Rayleigh data, we collected 774 images (three sets of 258 images averaged on the camera chip). The images were binned 2x2 to give an actual image resolution of 513 x 460 pixels. Finally, two photodiodes were used to monitor the delay between the two pulses.

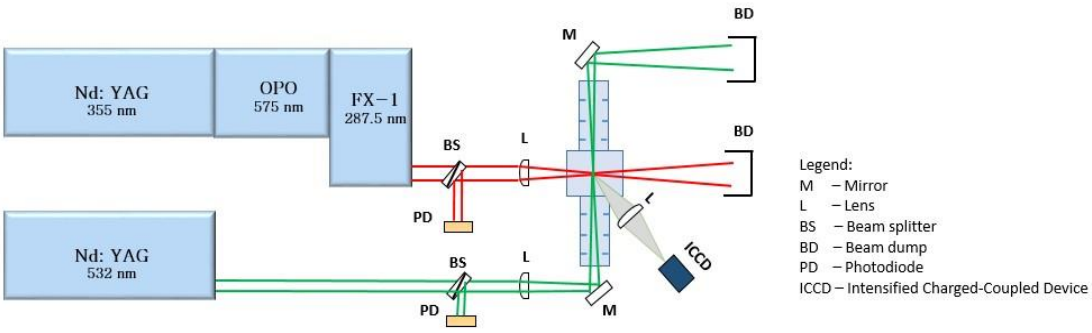

Figure 3.2: Optical layout for laser induced REMPI plasma formation. The Thomson\ Rayleigh scattering setup used for measuring gas temperature is also shown.

3.2.4 Confirmation of Oxygen Resonance

Shown in Fig. 3.3 (left) is a typical REMPI wavelength scan of the Thomson scattering signal due to excitation of the O_2 (Π, v = 2) state. The mixture consisted of pure oxygen at an initial pressure of p_0=1 bar and room temperature (T_0~300 K). The Thomson signal collected during the scan changes with wavelength as the laser is tuned to various rotational transitions within the band. Note that since all of the electrons detected through Thomson scattering are obtained from molecules that first pass through the excited state O_2 ($C^3\Pi$, v=2), the REMPI spectrum presented below is due to the rotational structure of this vibronic state. The maximum signal intensity is observed around 287.6 nm which is in good agreement with the literature.[67] Importantly, the signal

completely disappears as the laser wavelength is scanned away from the transition (towards λ=289 nm). The role of the two-photon resonant absorption process in the plasma formation process is further confirmed by analyzing the dependence of the collected REMPI signal on laser intensity. Data presented in Fig. 3.3-right were obtained by setting the laser wavelength to 287.6 nm and varying the laser energy between 1 mJ and 4 mJ. The numerical fit suggests that the plasma density varies with the laser intensity squared (~I^2). For a typical non-resonant MPI process one would expect a dependence on the order of ~I^3 since three photons are required to be simultaneously absorbed to photoionized the molecule from its ground state O_2 ($X^3\Sigma$). This finding serves to further confirm that the plasma analyzed herein comes from a 2+1 process that is resonant with O_2.

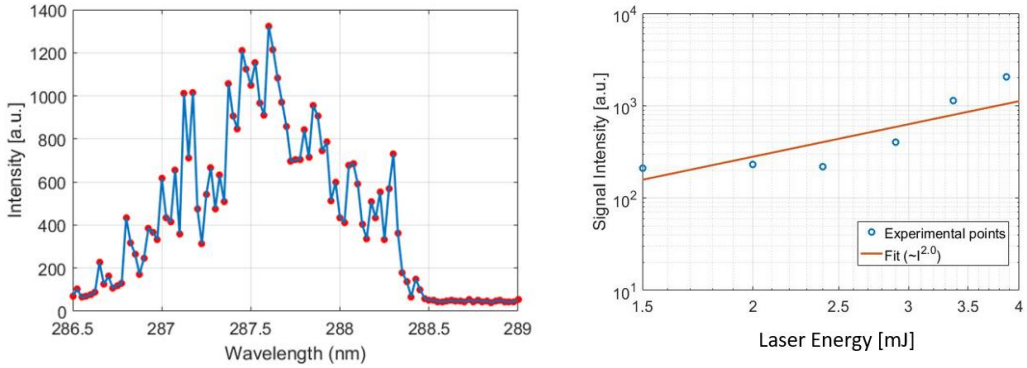

Figure 3.3 (Left): O2 REMPI spectrum obtained due to the two-photon excitation of the C3Πg (ν' = 2) ← X3$\sum_g^-$ (ν'' = 0) transition E_{REMPI}=3 mJ. **(Right):** Dependence of REMPI signal on laser energy. All data was collected at p_0=1 bar and T_0~300 K.

3.2.5 Electron Density Measurements by Thomson Scattering

Combined Rayleigh/Thomson scattering data from the plasma generated using the 2+1 O_2 REMPI scheme is presented in Fig. 3.4 below. Note that the data presented here is normalized by a reference state (or baseline) in which the REMPI beam is turned off. The laser wavelength was fixed at λ=287.6 nm (maximum value of REMPI spectrum, see Fig. 3.3-left) and the laser pulse

energy to E_{REMPI}=3 mJ. The plot in Fig. 4 shows how the scattering signal varies along the probe scattering beam. Far away from the center of the plasma (at x~-2 mm and x~2 mm) the signal ratio is unity since the gas is unperturbed by the plasma and the temperature is still ambient. However, at a time delay of 100 ns, one observes that the signal gradually increases, above the reference, as we approach the center of the plasma channel formed by the REMPI beam. This is attributed to the presence of Thomson scattering from the electrons at the focus of the REMPI beam. At this point in time the acoustic waves start to coalesce at the edges of the kernel leading to a decrease in density (and temperature increase) at the center of the plasma channel (at x=0 mm). As time progresses, it is initially observed that the signal intensity at the center of the plasma decreases due to plasma recombination leading to a decrease in electron number density. The signal stops decreasing at around 600 ns thus signaling the end of the phase in which Thomson is the dominant scattering mechanism. As shown in Fig. 3.4, one can bound the electron density by assuming the entire signal at this pixel location is due to Thomson scattering (upper bound) or by assuming that the Thomson scattering contribution is the difference between the normalized reference signal and the signal at the center of the plasma (lower bound). The salient point for the upper bound is the assumption that the plasma temperature is very high. As such, the Rayleigh contribution to the signal is expected to be very low (note that for a plasma temperature of 3000 K, the normalized Rayleigh signal would be only 0.1). In this scenario, one can assume that the entire signal comes from Thomson. The lower bound assumption implies that the temperature is negligible. Hence, any signal above unity at the center of the plot can be attributed exclusively to Thomson scattering from electrons. Based on these arguments, the electron number density of a 3 mJ REMPI pulse at 100 ns delay was estimated to be between: n_e = 1.3–3.7 x 10^{17} cm^{-3}. It is worth noting that the previously used non-resonant pre-ionization method at 266 nm did not result in plasma formation

at 3 mJ. Nonetheless, it was shown in the past work by the authors that a 20 mJ pulse operating at 266 nm can generate a plasma with an electron number density in the range of n_e = 2.5– 6.1 x 10^{16} cm^{-3} at a similar delay.[12,13] These findings suggest that we can generate a plasma within an order of magnitude denser while using only ~15% of the laser energy by employing O_2 REMPI compared to the previously studied MPI approach at 266 nm.

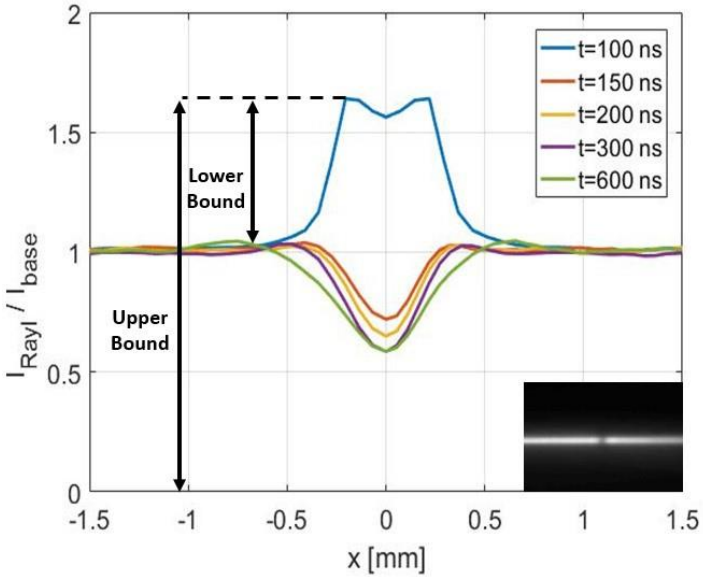

Figure 3.4: Normalized Thomson signal along the Rayleigh beam with the 2+1 O2 REMPI plasma induced at location x=0 mm. The plot shows the signal decreases with time thereby confirming the presence of Thomson scattering. An image insert showing the Rayleigh beam as seen by the ICCD camera is also included.

3.2.6 Plasma Temperature Measurements by Rayleigh Scattering

Using a similar approach to the one presented in the previous section, one can estimate the gas temperature. It is noted in Fig. 3.5-left that at later times (greater than 0.6 μs) the signal at the center of the plasma increases with time. This is the opposite trend to what was presented in Fig. 3.4 and indicates that Rayleigh scattering is indeed the dominant scattering mechanism at longer time delays. The signal increase is due to the fact the plasma is cooling down and the gas density slowly recovers to ambient conditions. Since Rayleigh scattering is a linear process, the ratio

between the signal at the center of the plasma and the baseline signal (at reference conditions) can be directly related to the change in density, assuming the temperature is sufficiently low. Moreover, the gas temperature can be inferred from this via the ideal gas law by noting that the pressure remains unchanged inside the pressure cell (p_0=1 bar). Using this ideal gas relationship, it was determined that the maximum gas temperature measured at 0.6 μs after the REMPI pulse is T=530 K $\pm$ 3 K. As expected, the REMPI pulse provides minimal heating which can be beneficial for a dual-pulse technique where it is desirable for the pre-ionization pulse to provide the necessary free electrons while producing minimal index of refraction changes in the gas due to heating. The latter aspect can play an important role in a dual-pulse scheme because large changes in the index of refraction of the medium (due to heating) could lead to defocusing of the energy addition (second) pulse. It is also interesting to note that the kernel dynamics involves the formation of a very weak acoustic wave that propagate from the main plasma kernel as time progressed. The acoustic wave is weak because the plasma is rather cold, with most of the laser energy going into photoionization rather than heating. A similar analysis for the 266 nm pulse showed no temperature increase at a pulse energy of 3 mJ. In contrast, gas temperature of T=2010 K $\pm$ 23 K was measured for a 266 nm pulse at an energy of 20 mJ. This demonstrates the ability of the REMPI pre-ionization scheme to generate a cold plasma at low laser pulse energy.

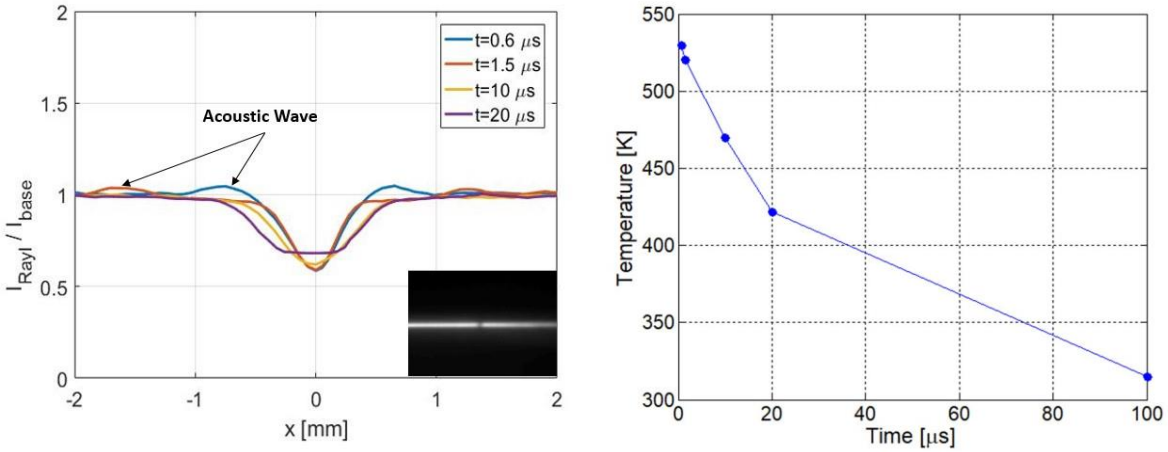

Figure 3.5 (Left): Normalized Rayleigh signal along the probe beam at various time delays after the REMPI pulse. The plasma is centered around x=0 mm. (Right): Time history of maximum kernel temperature.

3.3 Resonance Enhanced Dual-Pulse Plasma

3.3.1 Introduction

In this section, we expand upon our past work in preionization dual-pulse laser ignition to examine the possibility of using resonant enhanced multiphoton ionization (REMPI) of oxygen for the first preionization pulse. The candidate REMPI transition is a 2+1 resonance scheme of O_2 with a central wavelength of λ=287.5 nm, while the subsequent energy addition pulse is at 1064 nm in the near infrared (NIR). Our earlier research on resonant preionization plasma showed we could form plasmas with high electron densities (n_e=1.3-3.7 x 10^{17} cm^{-3}) and low temperatures (T=530 K) while using significantly less energy (E=3 mJ) than similar non-resonant plasmas.[69] For comparison, the non-resonant preionization plasma had electron densities that are an order of magnitude lower (n_e=2.5-6.1 x 10^{16} cm^{-3}), and temperatures an order of magnitude higher (T=3000 K), while requiring more than eight times as much energy (E=25 mJ).[13]

First, resonant ionization is confirmed by Thomson scattering and optical emission measurements as a function of laser wavelength in pure oxygen (T_0=298 K, P_0=1 bar). Rayleigh

and Thomson scattering techniques are then employed in air (T_0=298 K, P_0=1 bar) to determine electron densities and temperatures of the resulting dual-pulse plasma for pulse energies of E_{REMPI}=3 mJ and E_{NIR}=42 mJ. We report an electron density of n_e~7.5x10^{17} cm^{-3} at 150 ns. Finally, ignition experiments are conducted at varying equivalence ratios (ϕ =0.1–1.0) in propane-air, methane-air, and hydrogen-air mixtures. We report extension of the lean limit for methane-air mixtures relative to non-resonant dual-pulse ignition. Hydrogen-air ignition proved to have the highest peak pressures, greatest combustion efficiencies, and lowest lean limit of the three fuel mixtures tested. OH* chemiluminescence performed in tandem with ignition tests showed that dual-pulse REMPI plasmas exhibit similar kernel shapes to single pulse ignition characterized by an asymmetric torus and leading edge lobe which propagates towards the laser beam. Separation and quenching of the leading edge lobe occurred rapidly for lean mixtures. Variation in the waist offset (between the REMPI and NIR beams) had negligible effect on kernel shape and combustion efficiencies.

3.3.2 Optical Layout

The formation of the REMPI dual-pulse plasma is by overlapping of REMPI (~287.5 nm) and NIR (1064 nm) laser pulses. Beginning with the NIR beam, the fundamental output of an Nd:YAG (New Wave Gemini) is aligned onto two irises using a series of dielectric mirrors and a lens of focal length f=250 mm (LA1461-C). For the REMPI beam, an optical parametric oscillator (Sunlite EX OPO) is pumped by the third harmonic (λ=355 nm) of an Nd:YAG (Continuum Powerlite Precision II), while seeded by a continuous wave (CW) laser (Continuum SI-2000). The result allows access to a broad range of wavelengths (λ~445–1750 nm). For the present contribution, the OPO was set to approximately 575 nm such that the laser light exiting the

frequency-doubler (Continuum FX-1) was in the range of interest (λ = 287.5 nm). A dielectric mirror directs the REMPI beam through a lens of focal length f = 300 mm (LA4579-ML). A laserline mirror (Y4-1025-P), transparent to NIR light, was used to steer the beam onto the irises that already define the REMPI beam path. Fine-tuning of the overlap of the two beams (REMPI and NIR) is achieved by minimizing the beam energies required for plasma formation in lab air. Finally, the combustion chamber is added and minor adjustments are made to the beam splitter to optimize the plasma inside the chamber.

Rayleigh and Thomson scattering techniques were employed as a means to determine electron number density and temperature of the resulting dual-pulse REMPI plasma. The overall optical layout including Rayleigh and Thomson scattering of the dual-pulse plasma is shown below in Fig. 3.6.

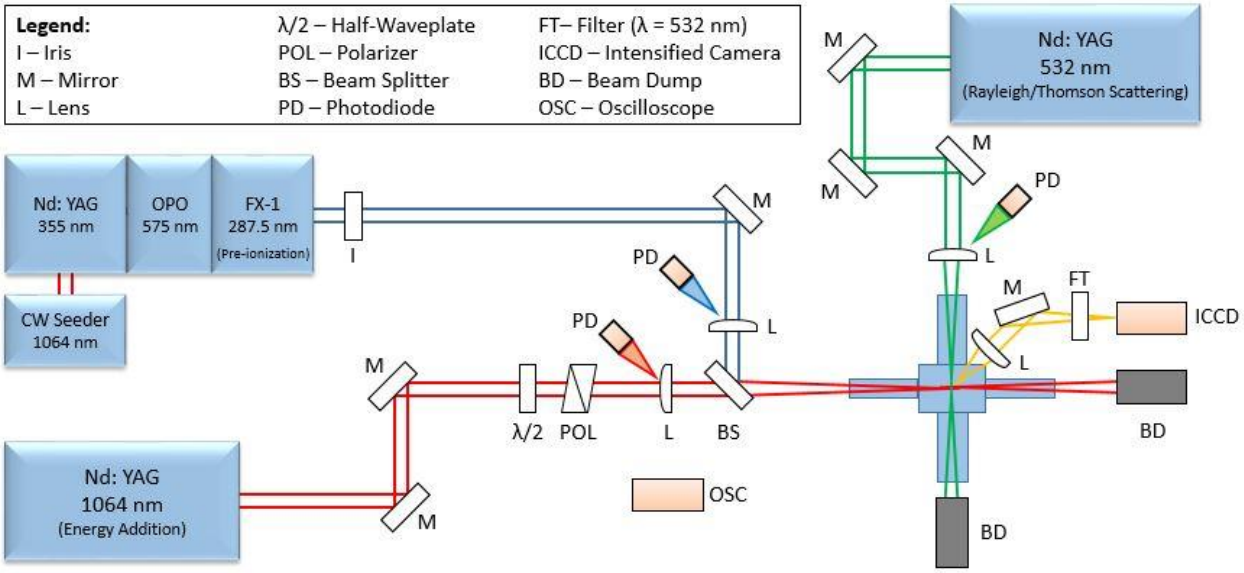

Figure 3.6: The optical setup for Rayleigh and Thomson scattering of a REMPI dual-pulse plasma.

Once the REMPI dual-pulse plasma has been well established inside the chamber, a (third) beam for Rayleigh/Thomson at 532 nm (Spectra Physics Quanta Ray) is aligned orthogonal to the

two ionization lasers using a set of dielectric mirrors and a plano-convex lens (f=250 mm). Intersecting the plasma at its center, this beam is aligned to scatter light from the plasma so that Rayleigh and Thomson scattering measurements can be made. Baffles are introduced into the chamber to diminish the noise associated with light scattering from the input and output windows. The plasma is imaged using a broadband collection lens (f=75 mm) and silver steering mirror, which direct the image into an ICCD camera (pco DICAM pro) which observes the scattering volume orthogonally from above. A bandpass filter at 532 nm (ThorLabs FL532-10) is used to filter out undesirable light from other wavelengths. For scattering measurements, 774 images are averaged at each point of interest (3 sets of 256 images averaged on the camera chip) using 2x2 binning, resulting in a detector array of 513 x 460 pixels. Photodiodes are positioned to monitor the delay between pulses and the firing of the camera.

Also of interest in this study are the characteristics of ignition associated with the REMPI dual-pulse plasma. Specifically, the combustion efficiency will be measured at varying equivalence ratios down to the lean limit such that comparisons can be made to the non-resonant dual-pulse plasma (and single-pulse laser ignition). These measurements are based on the heat release as found from pressure traces. The optical layout for ignition is shown in Fig. 3.7. To simplify geometry and calculations, ignition is performed without the orthogonal chamber arms. A dynamic pressure transducer (PCB Piezotronics 113B24) is connected to the chamber to record the pressure history of ignition, and an oscilloscope (Rigol DS1204B) is used to log data. Equivalence ratios were determined through partial pressure calculations. The chamber was first filled with the necessary partial pressure of fuel, immediately followed by the introduction of the oxidizer. A heating wrap maintained constant chamber wall temperatures of 50° C and the mixtures were allowed to thermally equilibrate for 10 minutes. During combustion, the ICCD was reoriented

to observe kernel dynamics using OH* chemiluminescence. A bandpass filter centered around 310 nm (Andover 310FS10-50) was placed in front of the camera to admit only light generated from the OH* radical generated through the branching reaction $CH+O_2=OH^*+CO$.

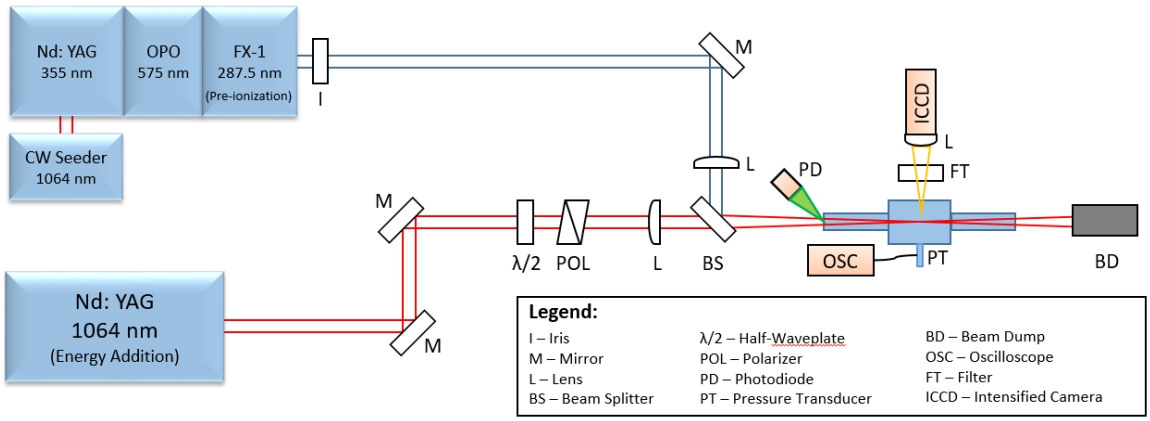

Figure 3.7: The optical layout for dual-pulse ignition of propane-air and methane-air mixtures.

3.3.3 Confirmation of Resonance

Since the goal of this investigation is to compare resonantly preionized dual-pulse plasmas to non-resonant dual-pulse plasmas, it is imperative that we first confirm that plasma formation employs the targeted 2+1 scheme. Excitation of the $C^3\Pi_g$ (v'=2) band can be confirmed by performing a wavelength scan and observing the resulting Thomson scattering signal ($E_{Scatter}$=2 mJ). Measurements were performed in molecular oxygen at initial conditions of P_0=1 bar and T_0=298 K. Plotted below in Fig. 3.8 is the maximum of the dual-pulse Thomson scattering signal 125 ns after plasma formation, normalized by laser energy. The step size in wavelength space was variable, with a minimum of $\Delta\lambda$=0.005 nm around the center and a maximum of $\Delta\lambda$=0.2 nm at the tails, resulting in 135 steps over the 4.5 nm range. The lasers were placed at energies of E_{REMPI}=3.5 mJ and E_{NIR}=37 mJ for which neither laser made a visible (by eye) spark on its own. Given the

relatively wide scan range, the beam energies and dual-pulse alignment were periodically adjusted. The overall spectral shape (containing detailed rotational structure) and maximum scatter signal at 287.615 nm are in good accordance with literature.[67,69,73] More importantly we see the scatter signal (indicative of electron density) approach zero outside the resonance band, illustrating that we are indeed resonant with oxygen in the preionization process.

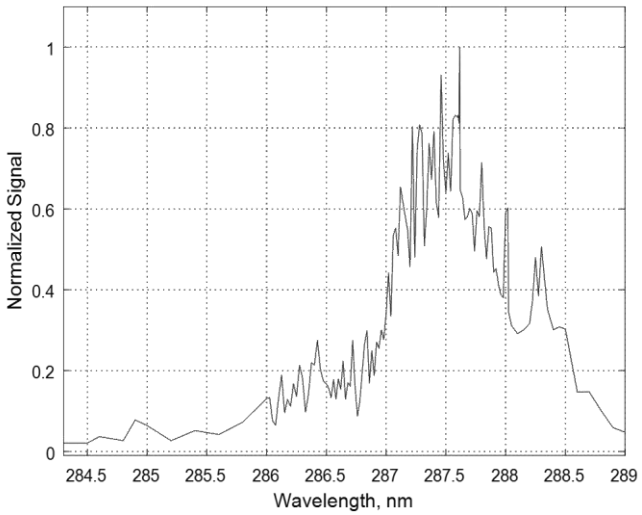

Figure 3.8: Thomson dominated scatter signal as a function of preionization laser wavelength confirming REMPI preionization.

Recognizing that maximum scattering signal corresponds to more highly ionized plasma as well as more successful excitation into the desired excitation state, we now park the preionization laser wavelength at 287.615 nm for subsequent studies.

3.3.4 Electron Density Measurements by Thomson Scattering

We employed combined (simultaneous) Rayleigh and Thomson scattering diagnostics to measure the electron density and gas temperature of the resonant dual-pulse plasma. We used energies associated with consistent plasma formation corresponding to E_{REMPI}=3 mJ and E_{NIR}=37

mJ (E_{Total}=40 mJ). The ionization medium was air at initial conditions of P_0=1 bar and T_0=298 K. By orthogonally probing the plasma with a diagnostic probe laser we obtain a scattering signal that is the combination of Rayleigh and Thomson scattering. In our past work, we have separated the temporal regimes where the scattering is Thomson versus Rayleigh dominated.[13] At early times, we expect the signal to be dominated by electron Thomson scattering at the center of the plasma. At later times, as the plasma cools and recombines, we reach a point where negligible amounts of signal are due to free electron scattering. It is in this later regime that we make measurements of gas temperature using Rayleigh scattering. The separation of the two regimes can be approximated as the time where the observed (normalized) scatter signal at the center of the plasma stops falling and begins to rise.[13,55] Typically, this is associated with a flattening of the central signal and the trace begins to look more like a "U" than a "W". Normalized scattering signals are shown below in Fig. 3.9. The vertical axis represents scatter intensity I/I_0 (i.e. plasma scatter normalized by the scatter signal from ambient air, which serves as a reference) and the horizontal axis represents the transverse location of measurement across the plasma waist. The insert shows a sample 2-D scattering image where the REMPI/NIR lasers are introduced from the top and the scatter probe runs horizontally. Electron density calculations are made based on bounds set by the ratio of the scattering signal to the reference as described in our previous publications.[13] Working inwards from the edges (e.g. at position +/- 2 mm for the 1 μs delay curve), one has I/I_0~1. This is ambient gas where the shockwave has not propagated to yet. Moving further inwards on the same delay curve, a "hump" is observed (i.e., I/I_0~1.6 at position ~+/- 1.3 mm) corresponding to changes in particle densities on the leading edge and trailing edge of the shockwave. Moving more inwards gives diminished signals attributed to high temperatures (low densities). Finally, at the very center, we observe a scattering peak associated with free electrons (Thomson scattering).[13,49]

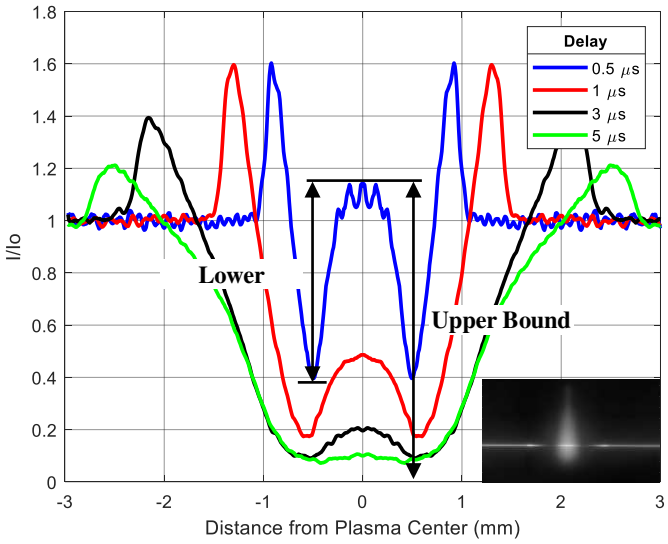

Figure 3.9: Combined Rayleigh/Thomson scatter signal along the transverse axis of the plasma for a resonant dual-pulse plasma. The scattering intensity has been normalized to a reference condition of Rayleigh scattering in air. Central signal rise is attributed to Thomson scattering from free electrons. The insert image in the bottom right details the raw ICCD image (before plasma and background subtraction) at a delay of 1 μs. The plasma formation lasers enter from the top of the image.

In Fig. 4, for the 0.5 μs delay case, we demonstrate the manner in which the bounds are set. The resulting electron densities at each delay are plotted in Fig. 3.10 against known electron densities calculated using the same techniques for both non-resonant dual-pulse plasmas as well as a non-resonant single pulse. The bounds indicate the estimates based on the bounds described above, while the center point is the average of the two. We observe that the resonant dual-pulse plasma has comparable electron densities to both non-resonant dual-pulse plasmas and non-resonant single pulse plasmas, though using only a total of 40 mJ for ionization as opposed to the 60 mJ required for non-resonant dual-pulse ignition, and 75 mJ required for non-resonant single pulse ignition. We report a peak electron density of $n_e \sim 7.5 \times 10^{17}$ cm^{-3} at t=150 ns.

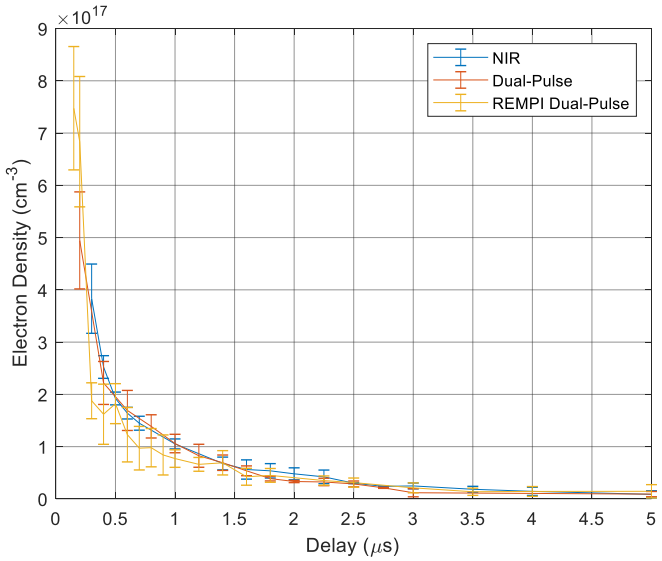

Figure 3.10: Electron density decay for the resonant dual-pulse plasma as a function of time. Comparable traces are shown for the non-resonant dual-pulse and single pulse cases.

3.3.5 Plasma Hydrodynamics

To fully understand the cooling process and accompanying plasma hydrodynamic evolution we examine the normalized scattering profiles at considerably later times from several microseconds to milliseconds (after the laser pulses). We can separate kernel dynamics into four regimes based on the scattering signal we observe. Each regime will be described in detail. The first regime occurs from ~0–5 µs and is dominated by plasma recombination. This regime is where we make estimates of electron density (Fig. 3.9 and 3.10). During this period, as the plasma recombines, fewer electrons scatter incident photons, resulting in central signal decay. The shockwave weakens (loses energy) as it propagates through the ambient medium. In the second regime at ~5–100 µs electron scattering is considered negligible. In this regime, the central scattering signal rises due to plasma cooling, the shockwave propagates to the edge of the frame, and we observe a "shelf" across the scattering profile that occurs immediately adjacent to the

shockwave. This is shown in Fig. 3.11 (most visible at ~10 µs) and is attributed to the density field of the rarefaction wave. Temperatures remain high during this period.

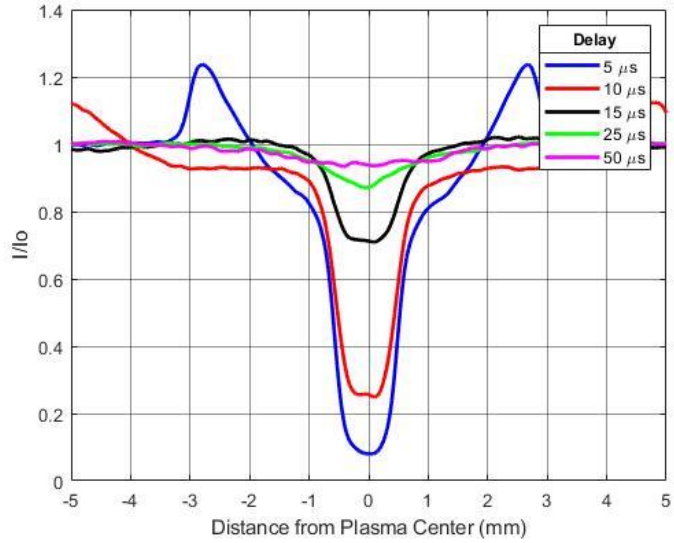

Figure 3.11: Rising temporal normalized scattering signal for the resonant dual-pulse plasma. This is indicative of plasma cooling and is the regime where we begin to estimate plasma temperatures.

After the signal has almost reached the reference condition (i.e. *I/Io*~1 over most locations), the plasma enters the third regime from ~100–500 µs. This regime is characterized by the development of more valleys across the profile which together yield a "W" shaped scattering signal as seen in Fig. 3.12.

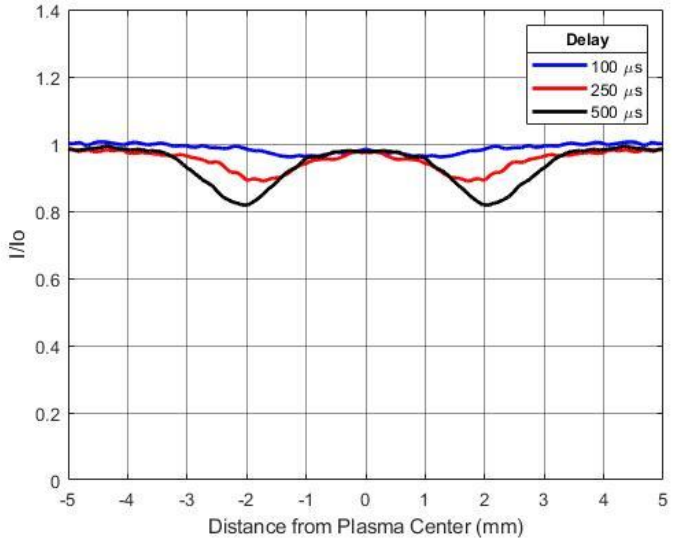

Figure 3.12: The normalized scattering signal for the resonant dual-pulse plasma in regime 3.

We attribute the "W" shaped profile to the fluid dynamic evolution of the plasma kernel. Kernel dynamics of both resonant and non-resonant dual-pulse plasmas dictate high temperatures in an axisymmetric toroid (originating from a counter-rotating toroidand a cool central tunnel).[2,58] A small increase in temperature is observed along the centerline. An image from modeling results by our group of a non-resonant DP plasma at 300 μs is shown in Fig. 3.13, with a sketched 1-D density profile (proportional to *I*/*Io*) based upon the probe location indicated by the white line.[58] This profile is approximately the inverse of the 1-D temperature profile by the ideal gas law. We hypothesize our probe beam to be in the location given by the white line due to the distance between valleys in Fig. 3.12 (approximately ±2.0 mm). It is important to note that the location of the scattering beam has significant effect on the scattering observed. A secondary location of kernel intersection is shown with a black line, as are the corresponding 1-D density profile. We hypothesize that the reason we have observed multiple dips for the single pulse NIR plasma in section 2.3 is due to this normalized scattering signal dependence on probe location.[55]

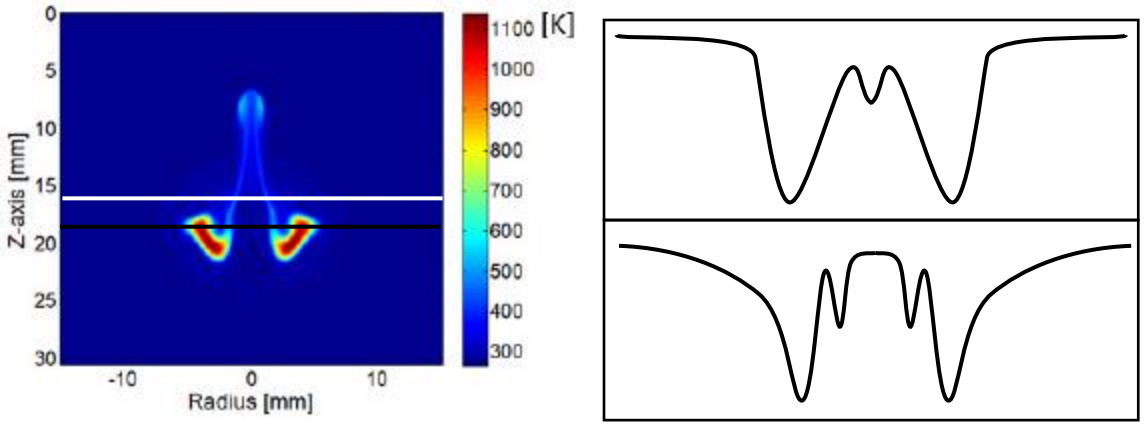

Figure 3.13: Plasma kernel temperatures at 300 µs (left) and corresponding 1-D densities based upon the white (right-top) and black (right-bottom) probe locations.[58]

The final regime from ~500 µs – 10 ms is characterized by a rise in the outward propagating valleys back to the reference condition. This is explained by the toroid continuing to cool, as well as a propagation of the toroid beyond the probe location. By 10 ms, little inhomogeneity exists in the medium and the signal and reference conditions are roughly equivalent as shown in Fig. 3.14. The present scattering measurements are spatially 1-D. In the future, 2-D (planar) scattering may allow for more detailed study of hydrodynamic effects including shockwave propagation, vorticity generation, and lobe formation.

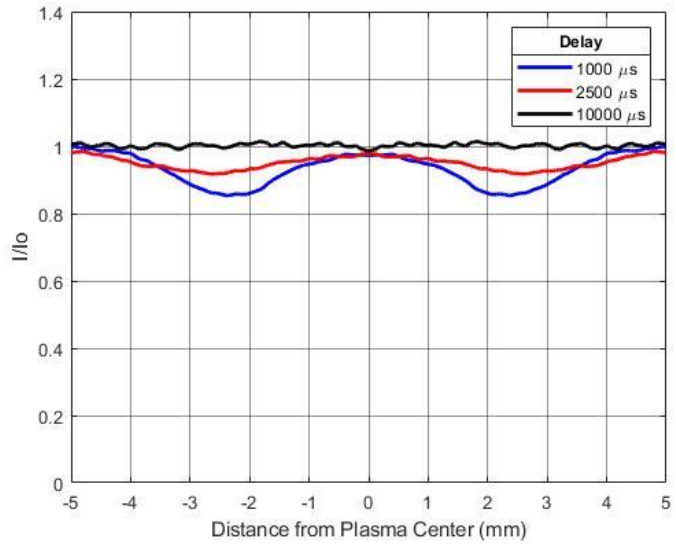

Figure 3.14: The normalized scattering signal for the resonant dual-pulse plasma at late (ms) times.

3.3.6 Temperature Measurements by Rayleigh Scattering

As described in section 2.3.2, Rayleigh based temperature measurements can be executed in sections where we assume either constant pressure or constant volume scenarios (as to accurately predict the temperature dependent scattering cross sections). Generally this technique is only employed at later times (>5 μs), where we can assume constant pressure and plasma chemical equilibrium composition. We propose a new method of estimating early time temperatures with constant volume assumptions, which requires that we assume kernel dynamics for the resonant dual-pulse plasma are similar to the non-resonant dual-pulse plasma. Given the complex flow fields shown above, we perform temperature measurements across the entire transverse axis, rather than at the point of minimum intensity (as the ideal gas analysis would recommend). The results are shown in Fig 3.15 for the constant volume, early time cases (left), as well as the constant pressure late time cases (right). It is important to note that the temperature profiles are highly sensitive to the (axial) location at which the Rayleigh probe beam crosses the laser plasma. Based on our hypothesized intersection shown in Fig. 3.13 (the white line), the probe beam is likely crossing the laser plasma upstream of the main toroid structure and location of maximum temperature. For this reason, the temperatures reported here for late delays may not be indicative of the highest temperature of the full kernel (and we also note the reported temperatures are lower than in our past work on other dual-pulse laser plasmas).[13,55]

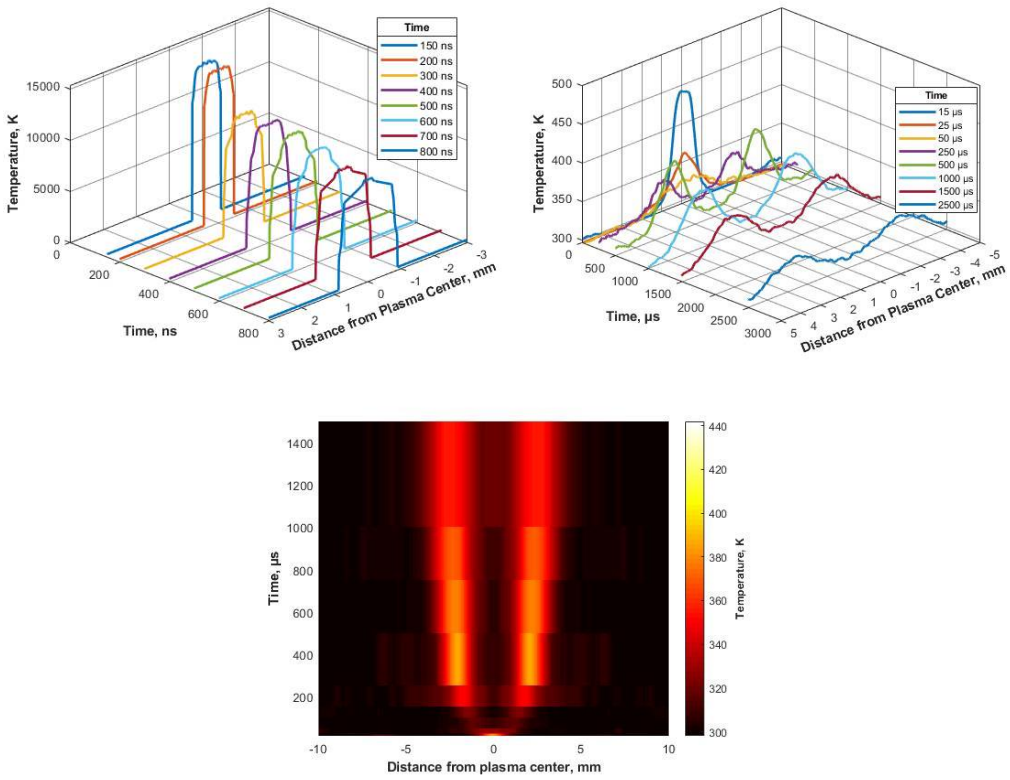

Figure 3.15: Spatial and temporal evolution of the resonant dual-pulse plasma kernel at early delays (top left) and late delays (top right, bottom). In the top figures, time is plotted in the direction out of the board to the right, and temperature is in the vertical direction. In the bottom figure, the temperature is represented by color, and the time decay is seen in the vertical direction. Transverse distance from the plasma centerline is on the x-axis for both plots.

At delays in the hundreds of microseconds time frame, we report temperatures around ambient with a cool central region and hotter region at a certain radius (~2-3 mm) from the centerline. This is consistent with the temperature range presented in Fig. 3.13 for the hypothesized probe location, where the peaks are attributed to the hottest regions of the axisymmetric toroid, and the central valley is explained by the entrainment of cool ambient fluid. By 10 ms, the temperature of the probe region has recovered to ambient. We attribute temporal variations in temperature to the time evolution of the kernel. The gas hydrodynamics predict expansion of the kernel in a manner that scans different regions of the kernel over the stationary probe beam. Because the probe beam is 1-D and fixed in space, it cannot follow a region of the kernel and is an

improper measure of maximum temperature. In the future, planar (2-D) Rayleigh scattering could be employed to fully cover the kernel flow field. Combining the results of the constant volume and constant pressure cases, and solving for maximum temperatures, we obtain Fig. 3.16. Accordingly we report a maximum measureable temperature of approximately 15,300 K at 150 ns. Kernel temperatures at later delays are similar to non-resonant dual pulse temperatures, though we note that the measurement is highly sensitive to probe beam location.

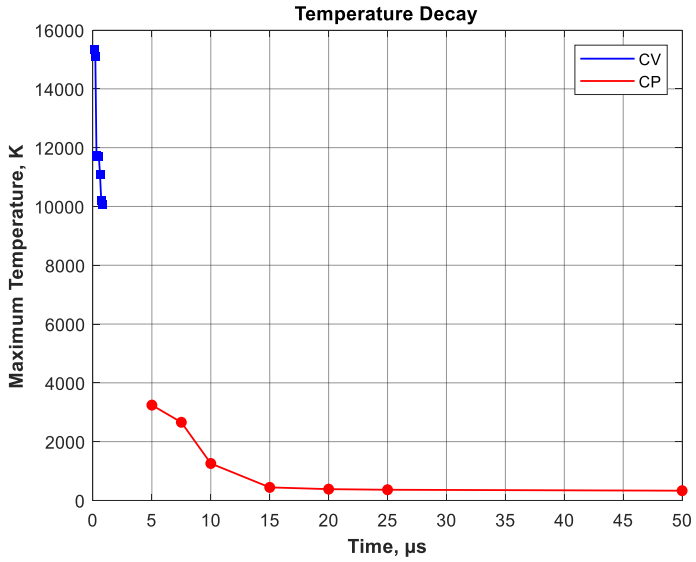

Figure 3.16: Temperature history of the resonant dual-pulse plasma. Here, the plot is segmented into the two regions where we know constant volume (blue) and constant pressure (red) analysis are somewhat reasonable. Much like the non-resonant case, this dual-pulse plasma falls below 1000 K very rapidly.

3.3.7 Ignition Testing

3.3.7.1 Combustion Efficiency

Resonant dual-pulse ignition was performed in three fuel-air mixtures, propane, methane, and hydrogen. Equivalence ratios of interest range from stoichiometric to the lean limit, with interest in precise determination of the lean limit. Pressure traces from these combustion events are shown in Fig. 3.17 where the central line indicates the average pressure, while the shaded

region represents one standard deviation from the average. At least ten pressure traces were collected for each equivalence ratio, and the results were averaged.

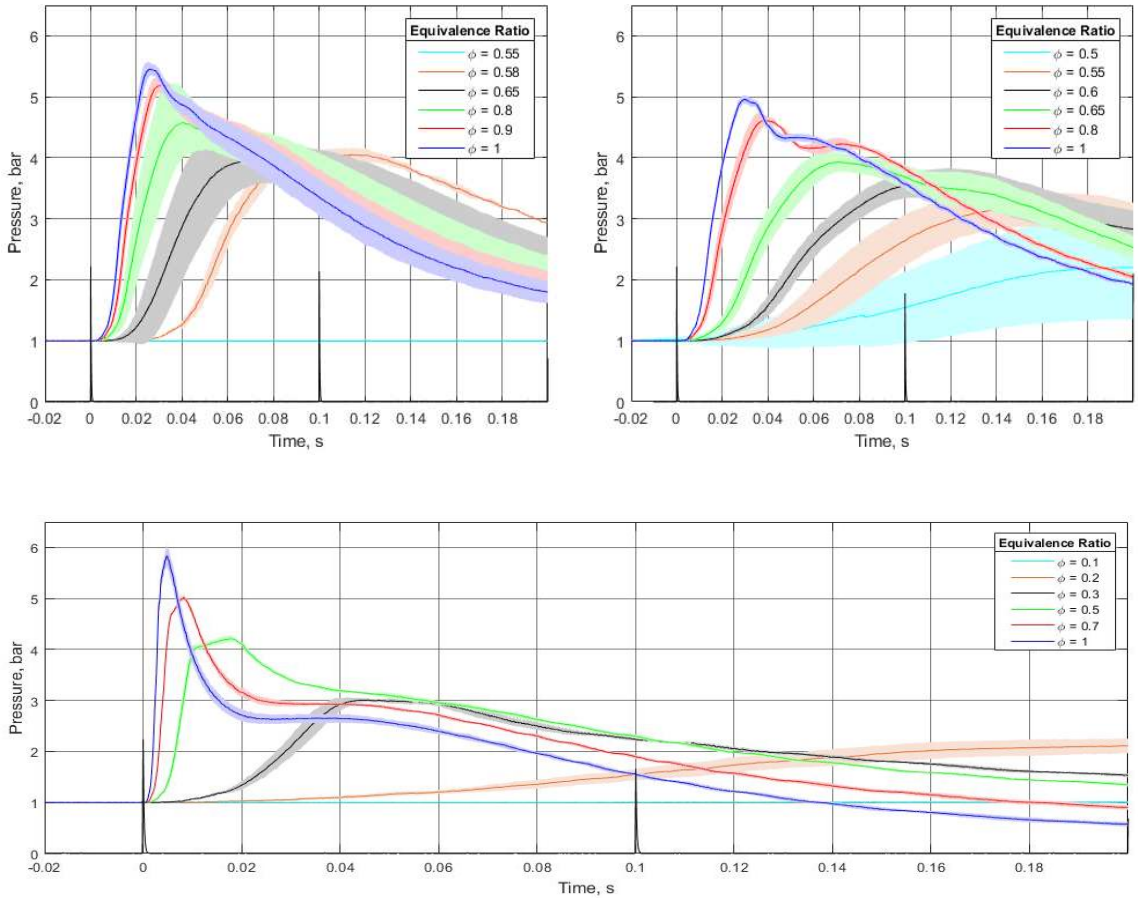

Figure 3.17: Pressure traces for propane (top left), methane (top right), and hydrogen (bottom) ignition using a resonant dual-pulse plasma. The line represents the average of ten traces, and the shaded region represents one standard deviation from the average.

We define the lean limit as the equivalence ratio for which ignition probability is greater than 50% (even including partial combustion events). Combustion efficiencies can be calculated from the heat release associated with the pressure traces and are presented in Fig. 3.18.[6] Vertical error bars represent one standard deviation in either direction, while horizontal error bars represent the uncertainty associated with partial pressure measurements. We report higher combustion efficiencies for hydrogen at nearly all equivalence ratios and similar efficiencies for propane and

methane for all equivalence ratios. Most cases in Fig. 14 ignited with 100% probability, but for cases where this is not true we indicate on the graph the number of successful ignition attempts as a proportion of the total number of tests. Accordingly, given our definition of requiring 50% ignition probability, we report a lean limit of ϕ~0.11 for hydrogen, a lean limit of ϕ~0.5 for methane, and a lean limit of has ϕ~0.60 for propane. For reference, non-resonant dual-pulse ignition has demonstrated lean limits of approximately ϕ~0.60 for both methane and propane while for single pulse ignition (with higher pulse energy) the lean limit for propane has been shown to be ϕ~0.7.[6,55] As expected, hydrogen ignites much more rapidly and easily than other fuels and also exhibits the highest peak pressure and shortest ignition delay.

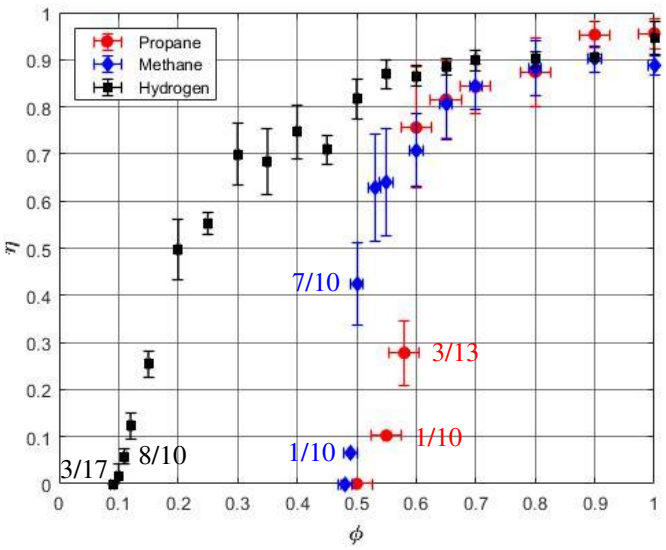

Figure 3.18: Combustion efficiency for propane (red), methane (blue), and hydrogen (black). Lean limits can be observed as the intersection of each data series with the x-axis.

Around the lean limit, we notice reduced efficiencies for propane when compared to methane. We consider localized variability in the equivalence ratio as a potential cause. Chamber heating is meant to encourage thorough mixing of the fuel and oxidizer, but little investigation has been performed with regards to how much time is necessary for proper mixing to occur. An

investigation into the ignition probability of methane around its lean limit ($\phi = 0.49$) showed that fifteen minutes of thermal equilibration significantly increased ignition probability. Future work will incorporate specialized mixing time for differing fuels based upon calculated diffusion rates.

3.3.7.2 Kernel Shapes from OH Chemiluminescence*

During combustion, we also monitor plasma kernel development via OH* chemiluminescence. A proxy for high temperature regions, OH* emission intensity allows for qualitative generalizations with regard to flame fronts and kernel shape. Ignition of stoichiometric methane is shown below in Fig. 3.19. Other fuels at equivalence ratios near stoichiometric exhibited nearly identical tendencies.

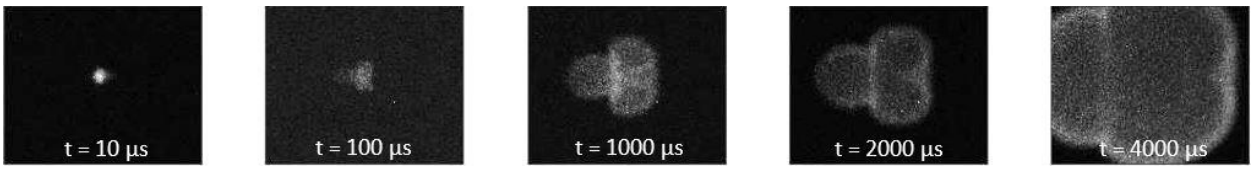

Figure 3.19: Flame propagation of stoichiometric methane images using OH* chemiluminescence. Text boxes detail the time at which the images were taken.

The results from OH* chemiluminescence reveal that third lobe formation occurs in all ignition events of all fuels at all equivalence ratios. However, lean cases exhibited rapid quenching of the third lobe within the first few hundred microseconds. Many showed separation of the third lobe from the toroid. For these cases, toroid vorticity continues to circulate fluid back towards the laser along the centerline, resulting in a point at the leading edge and the dimple on the trailing edge. At extremely lean conditions, kernel formation and long term development is very unpredictable. We hypothesize this to be due to localized variations in equivalence ratio, as well

as plasma temperature and electron density distributions. Some exemplary images from the ignition of methane are shown below in Fig. 3.20. These cases show multiple lobes and toroids separating and combining in a variety of different ways. We also notice that the flame speed of the kernel varies significantly in each ignition event.

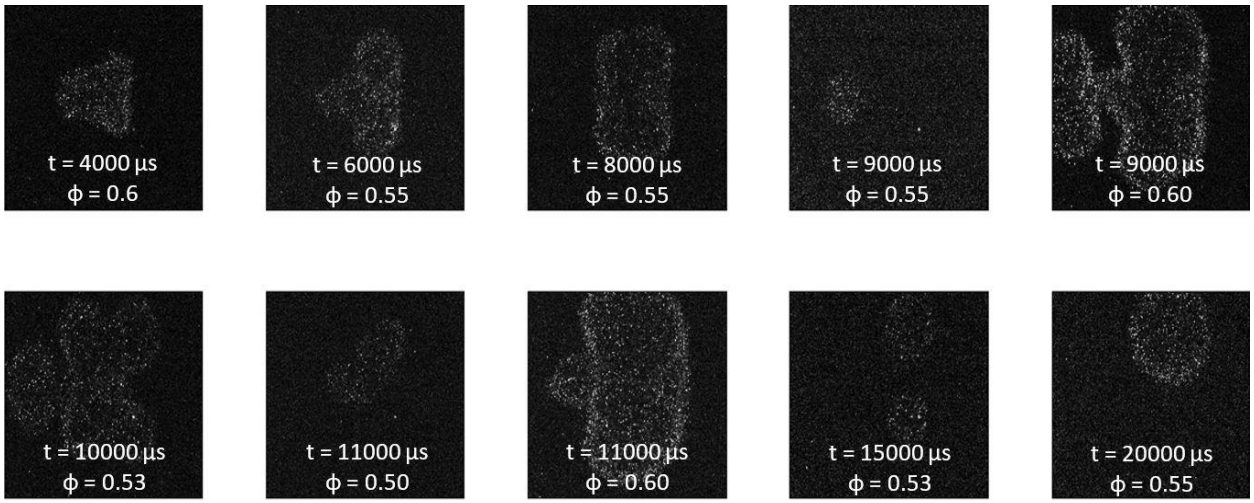

Figure 3.20: Kernel development of lean methane-air mixtures. Text boxes detail the time at which the images were taken and the equivalence ratio. We see significant variation between the images, which we attribute to localized variations in the equivalence ratio.

3.3.7.3 Investigation of Axial Offset on Resonant Dual-Pulse Ignition

Non-resonant ignition showed that focusing conditions, in particular any axial offset between the two beams, can significantly impact the kernel dynamics and ignition characteristics of dual-pulse plasmas.[6] By varying the offset between the waists of the ionization beams, plasma properties can be controlled. Ignition experiments were performed as described previously using a series of waist offsets. Resulting efficiencies extracted from pressure trace histories are shown in Fig. 3.21. Here, each point represents the average of three ignition tests.

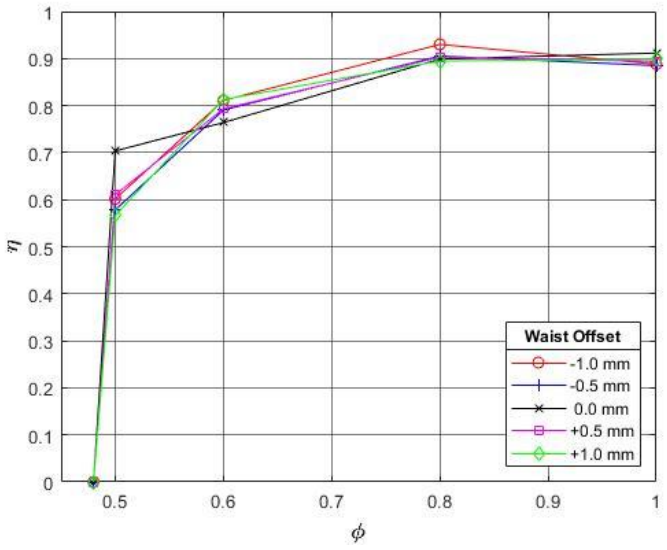

Figure 3.21: Combustion efficiency for different offsets. A negative offset represents the NIR beam focusing before the REMPI beam, and a positive offset represents the NIR beam focusing after the REMPI beam. Each point represents the average of three ignition tests.

Unlike the non-resonant case, we observe negligible differences in combustion efficiency as a function of the waist offset. All traces exhibit similar trends and identical lean limits. We hypothesize the difference to be due to the energy deposition ratios of each laser though it is important to note that our setup records only the delivered, not deposited (absorbed) energy, and it is the latter that is more relevant. For the non-resonant case, the ratio of the preionization pulse energy to the secondary pulse energy is 1:2 (E_{UV} = 20 mJ, E_{NIR} = 40 mJ). For the resonant case, the ratio is approximately 1:12 (E_{REMPI} = 3 mJ, E_{NIR} = 37 mJ). We do report a slight increase in the combustion efficiency around the lean limit for the ideal overlapped case, though it is not significant. To understand the fluid dynamics of the kernel, we employed OH* chemiluminescence in tandem with ignition experimentation across the same range of equivalence ratios. The images are shown below in Fig. 3.22. Here, each row represents a different equivalence ratio, and each column represents a different offset between the waists. A diagram depicting the waist overlaps is also shown.

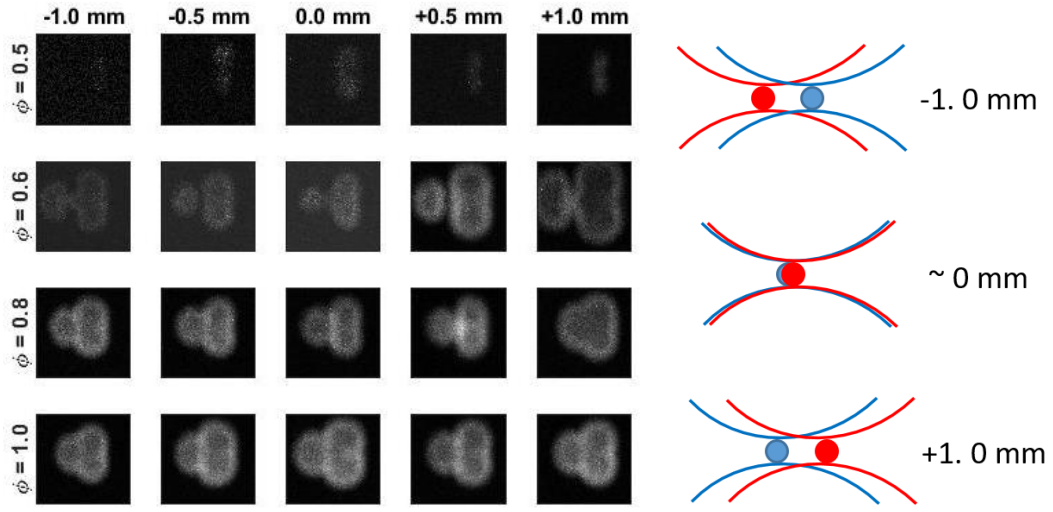

Figure 3.22: OH* chemiluminescence images from ignition (left) and a figure showing the overlap scenarios (right). The kernel exhibits similar fluid dynamic tendencies to non-resonant single pulse plasma kernels. Each image is taken at the optimal delay for plasma observation. This corresponds to 2 μs for equivalence ratios of ϕ = 0.80 and ϕ = 1.00, 5 μs for equivalence ratios of ϕ = 0.60, and 10 μs for the equivalence ratio of ϕ = 0.50.

We observe that little difference exists between the images at positive and negative offsets from the ideal overlap. This suggests that disproportionate energy depositions cause the flame to develop and propagate preferentially to the beam of higher energy. The preionization beam has little to no effect on the fluid dynamics, and only acts as an electron seeder for full breakdown. This prohibits advanced control over plasma properties as demonstrated through non-resonant dual-pulse ionization, and results in a resonantly enhanced dual-pulse plasma of properties very similar to the NIR single pulse case.

CHAPTER 4:

Filtered Rayleigh Scattering

4.1 Motivation

As demonstrated in section 3.3.5, reported temperature measurements are highly sensitive to the location of the probe beam. In the presented work we have done 1-D scattering (from a probe line), and sought to measure and report the highest temperature at a given plasma condition and time, but for fuller understanding (and comparison against simulation) it would clearly be preferable to perform 2-D planar measurements. Note also that the location of the peak temperature moves in time, and the complexity in interpreting the 1-D measurements given the spatial variations and the non-monotonic dependence of scattering signal on temperature. A further challenge in the present setup is in regards to suppression of background (elastic) scatter, for example from windows. Baffles along the beam line are used to minimize the collection of such background light but with the difficulty that if the beam slightly clips the baffle then aluminum particles can be introduced into the chamber, and these particles can strongly scatter light by Mie scattering which can damage the ICCD (hot-spot pixels).

To address the above issues, i.e. the need for 2-D planar measurements and improved background suppression, we intend to implement a planar filtered Rayleigh scattering setup (planar FRS).[74] By changing our focusing optics to a combination of spherical and cylindrical lenses, we can achieve a 2-D planar probe beam (i.e. a sheet of light). Further, following past literature, we will use a molecular vapor notch filter to suppress elastically scatter light (when the laser frequency is placed inside the absorption band). Specifically, we use a molecular iodine filter which possesses

transitions in the frequency range of the second harmonic of an Nd:YAG laser at ~532 nm. Matching to the iodine transitions requires two things from the laser: frequency overlap with the filter and narrow linewidth (~150 MHz). The following sections detail how we selected a transition and determined desired cell conditions, the effects of scattering volume conditions on filter transmission, as well as outline a couple experiments on a reference cell which demonstrate successful laser frequency tuning to match the transitions of the cell.

4.2 Theory

When laser light is sent through a scattering volume, the scattered light is frequency-shifted in a manner corresponding to the motion of the constituent particles. When this happens, the scattered light takes on a new broadened profile (also convolved with the laser line itself) that carries information on the velocity distribution (e.g. Maxwell-Boltzmann) of the scatterers. The scattering lineshape is typically referred to as the Rayleigh-Brillouin scattering profile and can be used to design filter conditions for FRS diagnostics.[74] There are two different regimes for Rayleigh-Brillouin scattering, both based upon density of the scattering volume. The first regime is referred to as the Knudsen regime, which assumes low density interrogation regions with Maxwellian velocity distributions and approximately no bulk velocity motion. In this scenario, the scattering profile can be estimated as a thermally broadened Gaussian line shape. The second regime assumes higher density, correlated molecular motion with a net bulk velocity. It is referred to as the hydrodynamic regime and is the sum of three Lorentzians, with two outer peaks indicative of sound waves propagating in opposite directions, and a central peak which is thermally broadened by the scattering volume. One practical example of this is laser light scattering from a plasma, where a radial blast wave is interpreted as equidistant Doppler shifts away from some

central frequency, and significant light is still scattered at the central laser frequency, which is thermally broadened. Though some of our experiments fall in this regime, we settle for the much more commonly used middle ground kinetic regime, where well established models exist. The most common model is the Tenti S6 model which assumes that the scattering volume consists of only one diatomic gas and neglects some rotational Raman transitions.[75] Existing literature demonstrates that despite these assumptions, the model can accurately predict scattering spectra.[74] Using a number of parameters such as particle density (N), mixture temperature (T), the scattering wave vector (K), thermal velocity (v_o), shear viscosity (η), and a characteristic Y-parameter, the spontaneous Rayleigh-Brillouin scattering lineshape can be obtained. Of all conditions, the Y parameter is best parameter to describe the state of the system. It can be calculated as shown below in Equation 4.1, and physically represents the ratio of sound waves capable of scattering light to the molecular mean free path of the scattering volume. This can be related to the ratio of the speed of sound in the medium to the speed of light, recognizing that $\Lambda \sim 1/\nu$, where ν is the frequency of incident light.

$$Y = \frac{NkT}{\sqrt{2}K v_0 \eta} \sim \frac{\lambda/2}{\Lambda \sin(\theta/2)} \tag{4.1}$$

Here, λ represents the wavelength of incident laser light responsible for scattering, Λ the mean free path of the molecules in the scattering volume, and θ the angle at which light is scattered from its direction of incidence. Y parameters significantly greater than one have small mean free paths, resulting in many collisions and a larger number of sound waves capable of scattering incident light. They generally describe system near the hydrodynamic regime and result in amplified three peak Rayleigh-Brillouin scattering (RBS) profiles. Y parameters significantly less than one have mean free paths larger than the required wavelengths of sound waves and therefore sound waves can't propagate to scatter light. They are indicative of systems in or near the Knudsen

regime, where the RBS spectra is estimated by a Gaussian lineshape. The effects of the Y parameter on the RBS spectra are published in literature, typically against a non-dimensional frequency x, which is a function of laser frequency, thermal velocity, and the scattering wave vector.[74]

Now that we know what our RBS lineshape looks like, we need to understand how the use of a molecular iodine filter can assist in the suppression of the central elastically scattered light, while admitting the Doppler shifted light. In order to do this, we must first understand how these iodine vapor cells function. One of the first absorption filters for FRS is described by Forkey et al.[74] It describes a cylinder of approximately 10 cm by 5 cm in diameter made of Pyrex glass with iodine crystals sealed inside the cavity. Control over the absorption intensity is established through two parameters, cell pressure and cell temperature. Cell temperature is controlled through heating tape applied to the outside of the chamber and usually has a controllability range of ~70 K. Control over the pressure inside the cell is much more complicated. Instead of controlling the pressure of the cell directly, the pressure of the cell is modulated through the control of side arm temperature. The use of this side arm allows for the separation of condensed iodine from gaseous iodine, which directly affects the vapor pressure of gaseous iodine and in turn the total pressure inside the cell. The temperature of the side arm is controlled using a heat exchanging water jacket, extracting heat from the cell and resulting in the condensation of iodine. The amount of condensed iodine, and corresponding cell pressure can be varied by changing the flow rate of the water (and therefore the rate of heat transfer) inside the jacket. The cell pressure can be calculated from the wet bulb temperature of this side arm (T_w) by Equation 4.2, below.[74] Of these two parameters, cell pressure (or side arm temperature) has the biggest impact on transmission. It can be imagined as if the side

arm temperature is used for coarse control of the transmission, while cell temperature used for the fine control.

$$log_{10}P(torr) = 9.75715 - \frac{2867.028}{T_W(℃)+254.180} \tag{4.2}$$

Cells that exist readily in the market today are referred to as "starved", which essentially means that they are sealed at some given temperature, and are intended to be operated above this temperature. This works essentially the same way as the non-starved equivalent, but requires a less complex system, where all that is required is the cell with some set starvation temperature (corresponding to the desired side-arm temperature if it were un-starved), and a temperature controller with heating tape. We were able to obtain such a cell to do some preliminary testing, which is described in section 4.5.

An important parameter to understand in the use of molecular iodine filters is the saturation intensity inside the cell. As detailed in section 4.5, a number of preliminary experiments resulted in senseless data due to excessively high input energy incident on the cell. Forkey reports the saturation intensity of the transition to be a function of transition frequency (ν=5.63 x 10^{14} Hz), the absorption cross section (σ=4.00 x 10^{-17} cm^2), and the natural lifetime (τ=1.00 x 10^{-6} s).[74]

$$I_{sat} = \frac{h\nu}{2\sigma\tau} \tag{4.3}$$

Using equation 4.3, we obtain saturation intensities on the order of ~4667 W/cm^2. Physically, this represents the threshold intensity above which stimulated processes are driven such that the molecular iodine can no longer strongly absorb incident light. For this reason, we need to make sure that light intensity passing through the cell does not surpass this value.

4.3 Simulation of Scattering Spectra for Cell Design

We first measured the range of output frequencies over which our seed laser (SI-2000) can usefully operate (in terms of linear frequency response to modulation). We then use the well established model developed by Forkey et al. to model the transmission of the filter in wavenumbers as a function of different input temperatures and pressures.[74] For our application, we will require two filters, one which actively monitors the frequency of the laser in real time and provides feedback to adjust laser frequency accordingly, and one which is used for the actual collection of scattered Rayleigh-Thomson light. For the reference cell, we will desire lower side arm temperature such that there is a greater response (change) of transmission for small changes in frequency. For the sample collection, we will want a higher side arm temperature and lower transmission as to suppress as much of the elastically scattered light from the planar probe beam as possible. When selecting a specific iodine transition and cell conditions for each of these filters, we looked for four parameters. The first was the magnitude of the transmission inside the absorption band. The second and third parameters important for filter design are that the notch must be wider than the background scatter, yet narrow enough to pass some reasonable fraction of the Doppler shifted scatter. The fourth and final parameter is the steepness of the sides of the notch, which ideally rises from full suppression to full transmission over <~1 GHz (~1 pm). In addition to these parameters, we designed our cell to have similar frequency and transmission trends to those noted in literature.[48,54,72,76–79] First, we select a transition for which the transmission minimum is small (at least less than 0.01) and then we alter the filter model conditions, specifically the cell pressure and temperature until we see that all of the aforementioned conditions were met. The final temperature and pressure determined to be (approximately) optimal are T=300 K and P=2 torr. The corresponding transmission plot is shown below, where the blue trace represents

filter transmission, the orange indicates our RBS spectra, and the red shows the laser lineshape with an assumed linewidth of 100 MHz. The transmitted region is also shown and is shaded in blue. Using this filter design, light elastically scattered by this lineshape will be significantly suppressed. Note that in practice, transmissions as low as those reported by the model will not be received since non-modeled filter transmissions may contribute and unseeded (broadband) light may be present within the probe pulse.

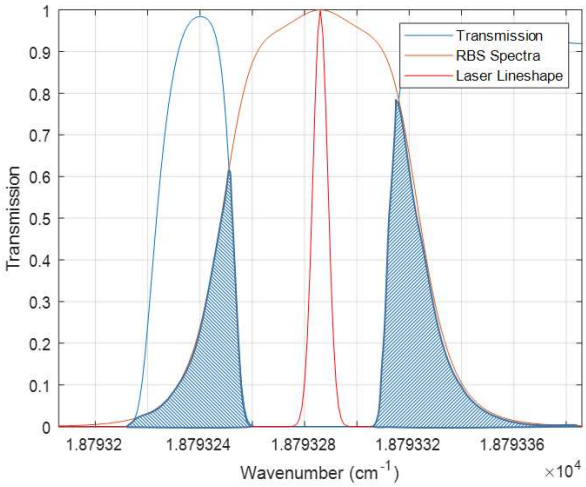

Figure 4.1: Filter profile at T = 300 K, P = 2 torr demonstrating selected filter conditions outlined in literature and the corresponding transmission (region shaded in blue).

The P=2 torr scenario allows for significant elastic scatter absorption (with transmission < ~10^{-24} at the very center), while still admitting a decent amount of Doppler shifted light from the RBS profile. Lower pressure admits more elastic scatter than is desirable, while higher pressure suppresses too much of the wings. The shaded region shown in Fig. 4.1 (right) shows the region which will pass to the ICCD in our setup. We calculate the corresponding side arm (wet bulb) temperature for the chamber using Equation 4.2, and find it to be T_w=49.013 °C.

4.3.1 Effects of High Temperatures in the Scattering Volume

Because the RBS spectra depend on pressure and temperature of the scattering volume, it is imperative that we understand exactly how much of the light is transmitted through the filter for different expected laser plasma cases. This is similar to the CP and CV curves for unfiltered Rayleigh scattering (Section 2.3.2) but now with an additional contribution to reflect the spectral overlap of the RBS (and Thomson) lineshape with the filter profile. For the CP case, we maintain the initial condition of 1 bar while incrementing the temperature in steps of 500 °C. For the CV case, we increment the temperature in the same manner and calculate a corresponding pressure from the ideal gas law using the known chamber volume of 195 cm^3.

4.3.1.1 Constant Pressure Scenario

We will begin by looking at the constant pressure case. There are five steps in this process. First, we need to develop the RBS spectra for each of the given temperatures and pressures. The dependence of RBS spectra on temperature is shown in Fig. 4.2.

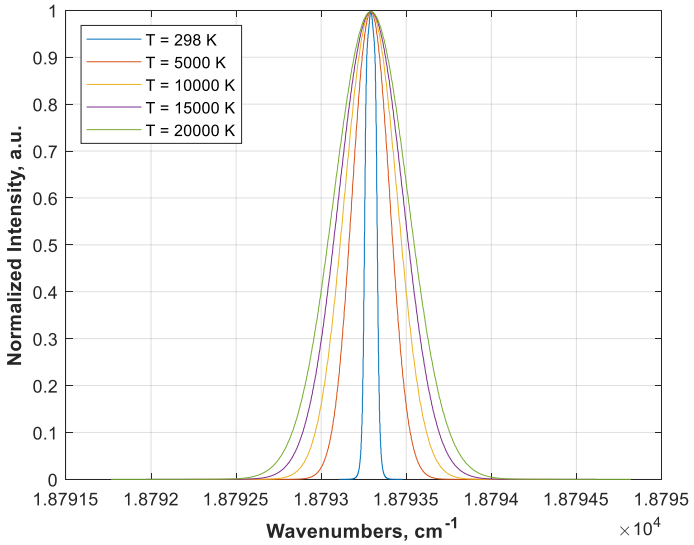

Figure 4.2: RBS spectra for a variety of input temperatures. Note that these spectra are normalized such that they all have the same peak height.

Then, we integrate the total area of the RBS spectra and the transmitted area of the RBS spectra based on the filter described in the previous section (where we match the center frequencies of the RBS and filter). This analysis is shown in Fig. 4.3, where three sample temperatures have been evaluated. Note that with increasing temperature, the broadening of the RBS spectra results in greater transmission.

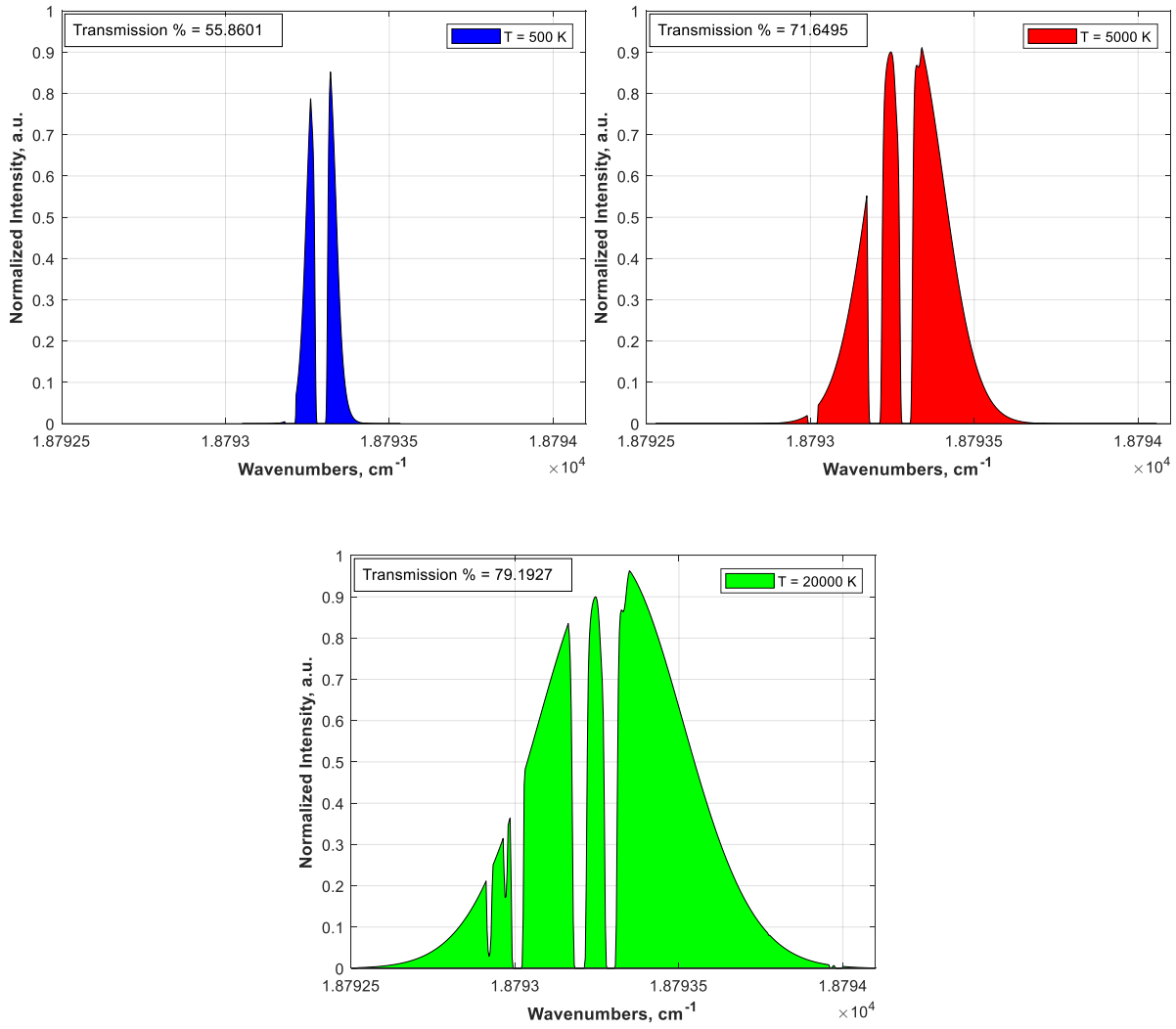

Figure 4.3: Transmitted light for RBS linshapes corresponding to T=500 K (left), T=5000 K (right), and T=20,000 K (bottom).

From those values, we determine the proportion of the RBS spectra that is transmitted and correct each of the points in the observed *I/Io* constant pressure and constant volume analyses by multiplying by the transmission percentage and dividing by the transmission percentage at reference conditions (298 K, 1 bar). As noted above, more light is transmitted due to a broadened RBS spectra for higher scattering volume temperatures. This manifests itself as a vertically "stretched" observed *I/Io* curve. This is great for data analysis in the T≥7500 K regime because it means experimental noise has less of an impact on the reported temperature, though the opposite is true in the T<7500 K.

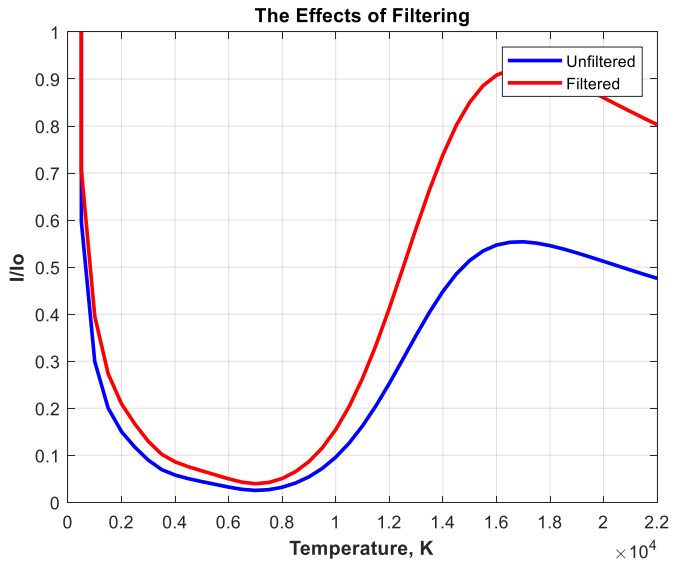

Figure 4.4: Constant pressure observed *I/Io* values resulting from the use of FRS and scattering volumes with different temperatures. The blue curve represents the observed *I/Io* for an unfiltered experiment, where the red represents the observed *I/Io* for a filtered experiment in this notch.

4.3.1.2 Constant Volume Scenario

Using the same techniques, we create RBS spectra using dictated temperatures and pressures calculated from the ideal gas law. Then, we overlay this with the filter and integrate to

solve for the transmission percentage. Shown in Fig. 4.5 are the corresponding RBS profiles and transmission areas.

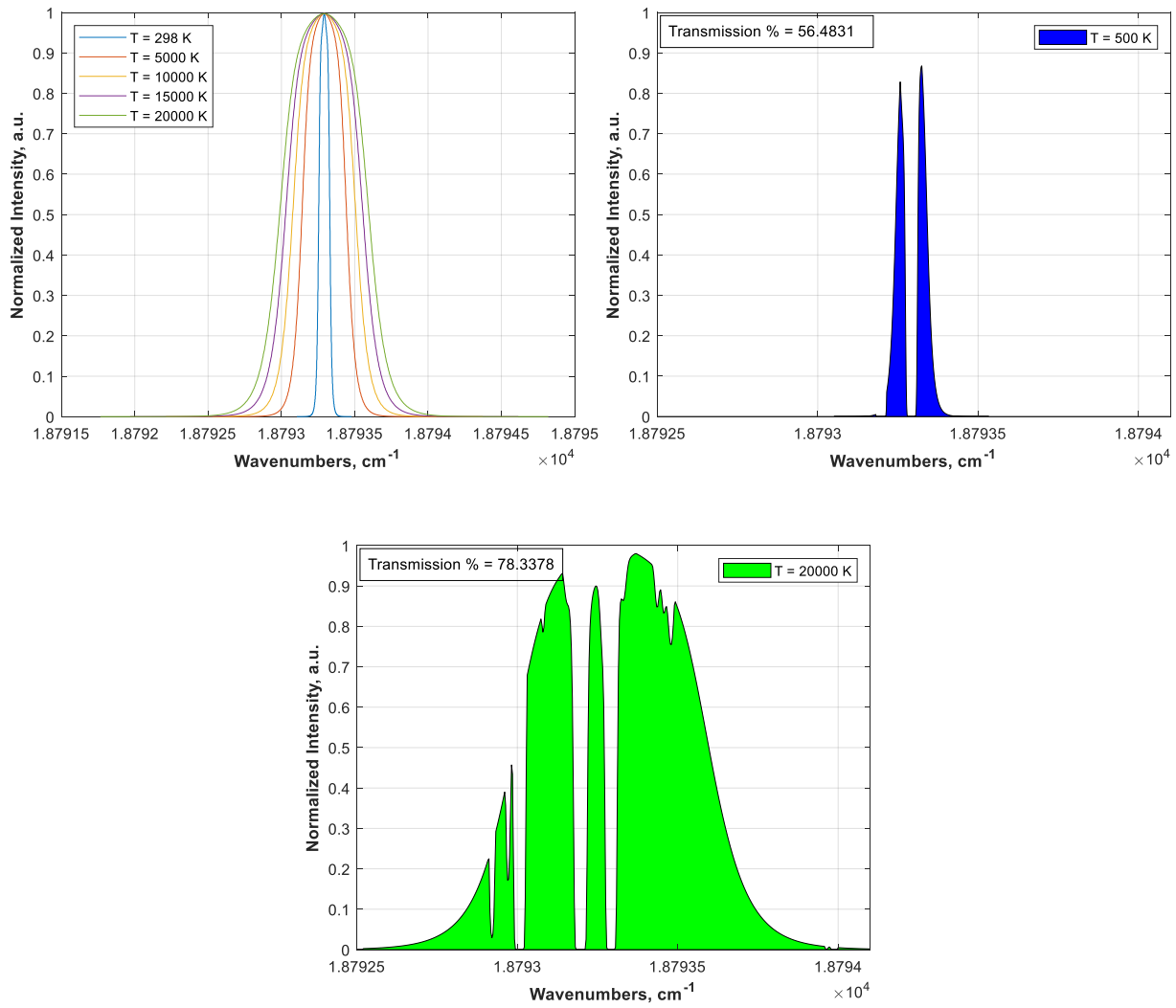

Figure 4.5: RBS lineshapes for a variety of temperatures (left), and transmitted light for RBS linshapes corresponding to T=500 K (right), and T=20,000 K (bottom). The RBS lineshape and corresponding transmission is different from those in the CP case, because the scattering volume pressure is assumed to vary with temperature by the ideal gas law, rather than remaining fixed.

Creating the observed *I/Io* curve, we ascertain that filtering gives us greater advantages at low temperatures where the slope is now greater, minimizing the impacts of noise, but we usually

use this at early times to evaluate signals of *I/Io* >> 1. It could be hard determining whether we are in the pre or post-dip region in some cases, but it shouldn't be impossible using some assumptions of plasma cooling and temperature distributions.

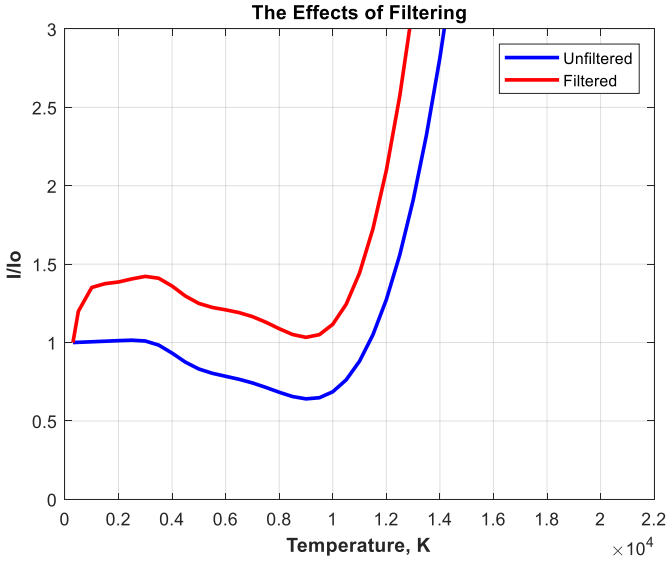

Figure 4.6: Constant volume observed *I/Io* values resulting from the use of FRS and scattering volumes with different temperatures. The blue curve represents the observed *I/Io* for an unfiltered experiment, where the red represents the observed *I/Io* for a filtered experiment in this notch.

4.3.2 Effects of Bulk (or Localized) Velocity Variations

In addition to understanding the effects of localized temperature gradients on the scattering signal and corresponding filter transmission, we want to confirm that bulk (or localized) velocity distributions do not bias measurements of temperature. We do this by applying a Doppler shift to our RBS spectra and performing the same integration procedure described above across a variety of temperatures, then apply those results to the *I/Io* curves. We do this for bulk velocities of ±10 m/s, ±25 m/s, ±50 m/s, ±100 m/s, ±250 m/s, ±500 m/s, and ±1000 m/s. Shown below is the result of the shift that occurs at 1000 m/s (the most extreme

case). Note the significant difference in shape (as compared to Fig. 4.3), because the RBS feature is no longer resonant (centered) with the I_2 absorption transition.

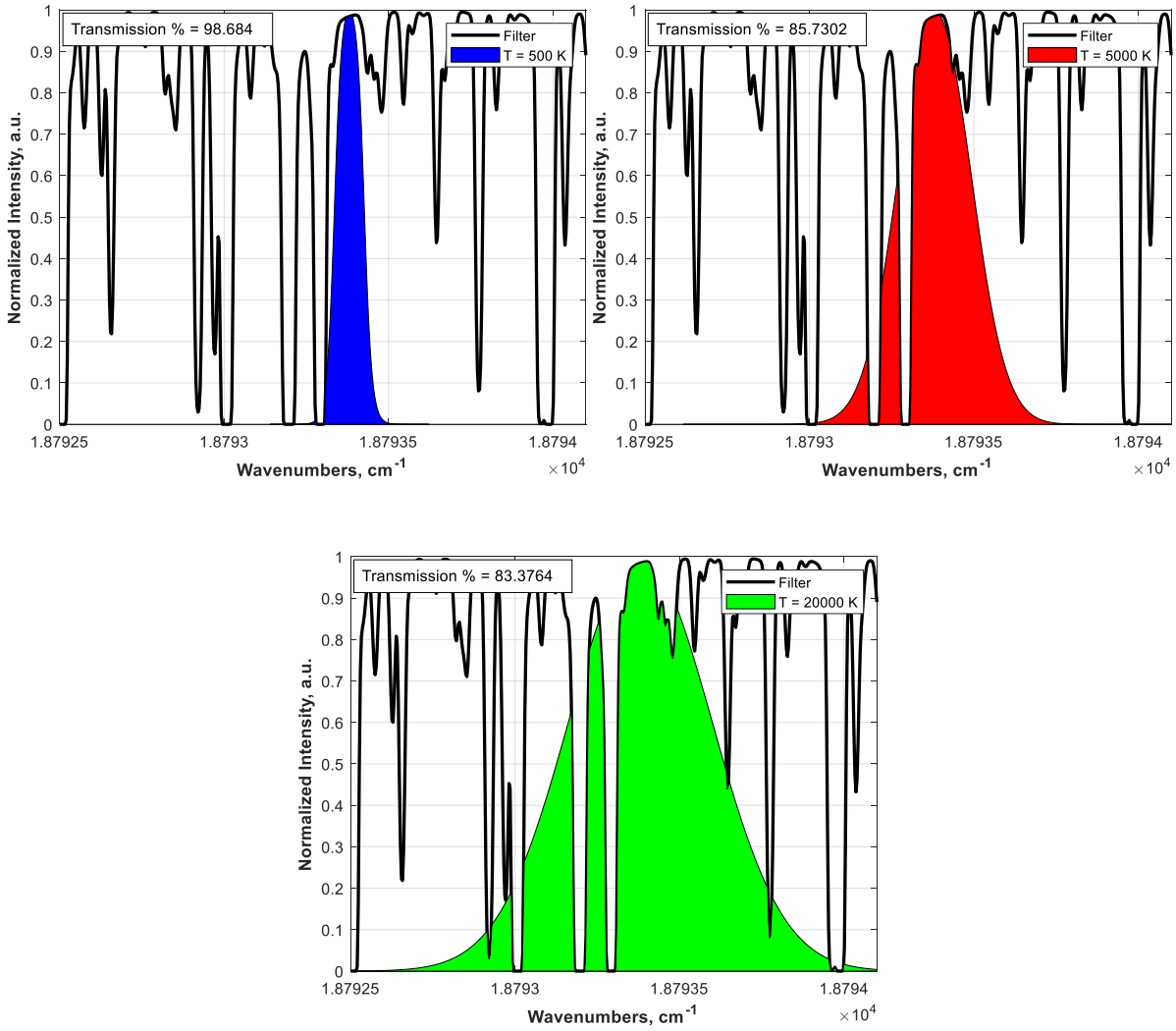

Figure 4.7: Transmitted light for RBS linshapes corresponding to T=500 K (left), T=5000 K (right), and T=20,000 K (bottom) for a Doppler shift of +1,000 m/s. Note how the Doppler shift moves the scattered RBS lineshape out of the targeted transition.

4.3.2.1 Constant Pressure Scenario

After applying these shifts, we examine the resulting observed intensity curve. We see that across the range of all Doppler shifts, there seems to be negligible changes in the observed intensity. We note larger differences at the tails, but not significantly different results. This is

actually quite a surprising result, and is investigated in more depth in Appendix A, where we validate the model is actually working properly by deriving the error from the ideal gas behavior that we know exists over the range of 0-2500 K. In Fig 4.8, you can see the effects of ±250 m/s. The orange curve assumes zero velocity. To estimate the error, lets take an example. Assuming an *I/Io* of 0.90 and a negligible velocity distribution, we would calculate a temperature of ~18,500 K. If the velocity is ~ ±250 m/s the real temperature is ~ 17,900 K or ~19,100 K. This is an error of 3.141%. Considering the velocity shouldn't exceed 250 m/s in more than a few regions of the frame, it is reasonable to assume the curve at 0 m/s. This will be examined with more detail in the following pages.

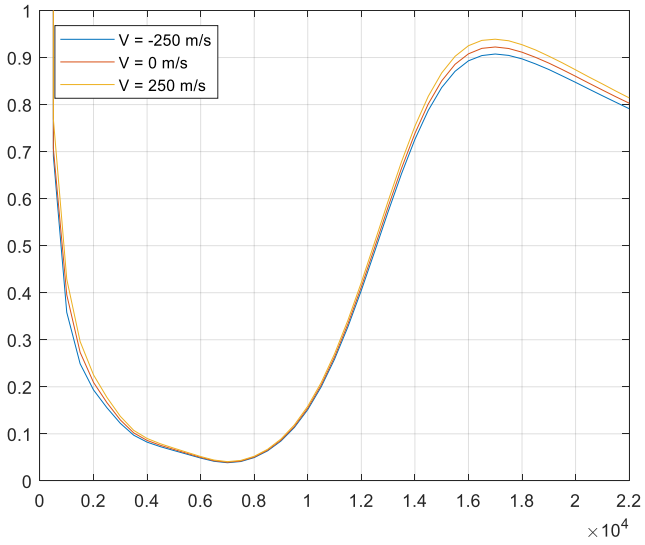

Figure 4.8: The observed *I/Io* lineshape for bulk velocity changes of ±250 m/s.

The spliced error results from 1/T symbolic calculations and 1-D interpolated errors (described in detail in Appendix A) are shown in Fig. 4.9. Breaks in the data indicate points where the 0 m/s case has no corresponding value at elevated temperatures (it exceeds the maximum of minimum of the elevated curve). Examine Fig. 4.8 for example, where the yellow curve doesn't

ever reach the minimum of the orange curve, and the blue curve doesn't ever reach the orange's maximum. We note these to be at the maximums and minimums of the curves, where the interpolated point switches from being of lower temperature to higher temperature. This is the reason for the sign change we also observe at this break. Examining the curves, we should be concerned about velocities greater than 250 m/s at temperatures < 2,000 K if we want to stay below 10 % error.

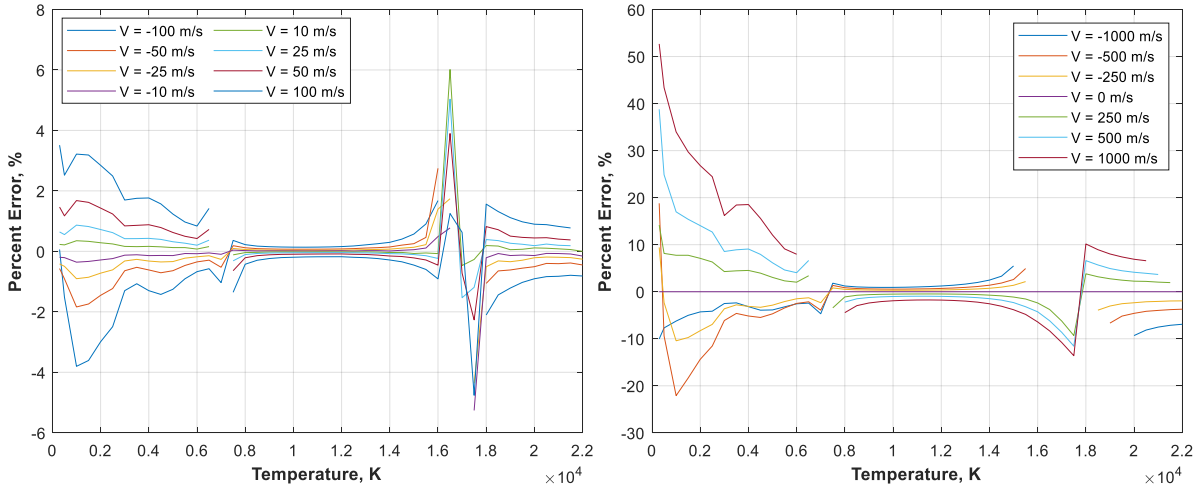

Figure 4.9: Estimated error in the CP case induced by assuming a net zero bulk velocity when the bulk velocity is actually in the range of 0-100 m/s (left) or 250-1000 m/s (right). Note that the error is reported as the spliced combination of where the 1/T assumption holds (which has better accuracy and resolution than 1-D interpolation) and 1-D interpolation where 1/T does not hold.

We see from modeling by Dumitrache et al. that around 5 µs (where we begin to employ CP analysis) we have maximum velocities ~150 m/s.[58] The velocity distribution at 4.703 µs is shown in Fig. 4.10, below, where the contour represents the velocity in m/s. Since we know that the velocity only falls from here, we can confidently conclude that we should not have error >10% in our measurement region when we assume no bulk velocity when a bulk velocity exists.

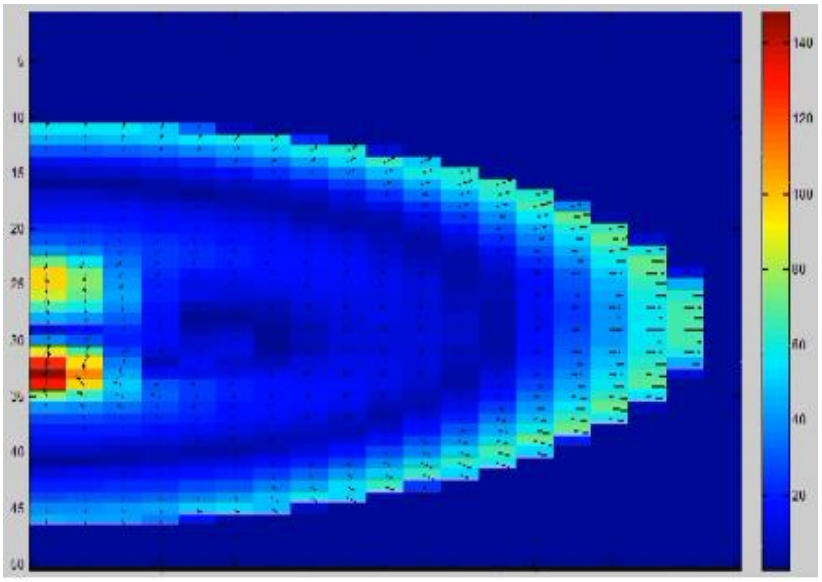

Figure 4.10: Kernel velocities for the non-resonant dual-pulse plasma at a time of ~4.7 µs after laser energy deposition. Note that the maximum velocity (shown as a countour) is less than 150 m/s, indicating we will have less than 10% error when employing the constant pressure analysis for temperature.[58]

4.3.2.2 Constant Volume Scenario

Applying the same analysis to the constant volume case, we obtain the observed intensities shown in Fig. 4.11 at selected bulk velocities of ±250 m/s, though all velocities previously mentioned were again employed. We note larger differences at lower temperatures and no general trend, as the transitions have arbitrary distances from the central transition, so the transmittance (and therefore *I/Io*) are somewhat arbitrary. We typically use this kind of analysis (CV) on high temperature early time (<1.5 µs) plasmas. Here, the temperature is generally in excess of 10,000 K. Because of this, we should be fine to use the 0 m/s case, though we should note that temperatures below 5,000 K have significant dependence on the velocity of the scattering volume. If we have a very cold plasma, we should try to incorporate a velocity measurement to accurately predict temperature.

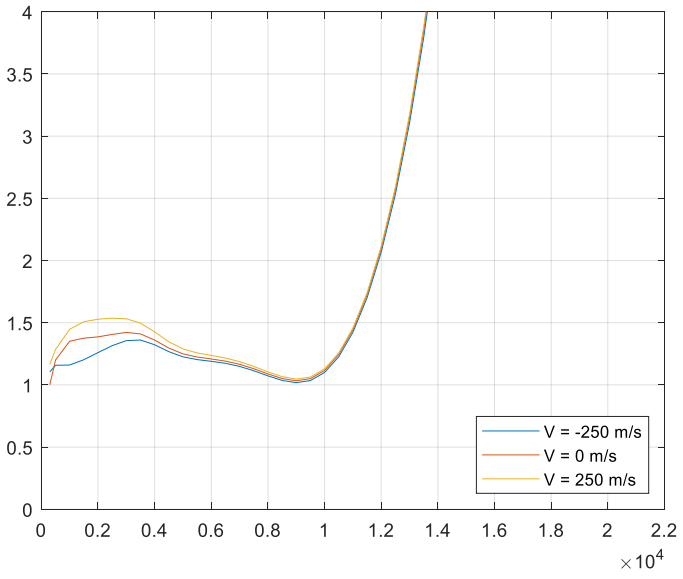

Figure 4.11: Observed *I/Io* curves for a few selected bulk velocities. We typically see much variation around 0-4000 K, but good agreement regardless of bulk velocity magnitude below that, which we attribute to small changes in transmission associated with a very large thermally broadened RBS spectra as shown in Fig. 4.2.

Because we have no equations that properly model the *I/Io* curve, we have to experimentally interpolate the error for all points. We see that the effects are much more profound on the CV case, where the *I/Io* curve is much more dependent on velocity and has relatively similar low temperature *I/Io* values. Again making use of the non-resonant dual-pulse model developed by Dumitrache et al., we can further constrain our range of analysis.[58] During the time for which the CV case is used, the velocity range is 0 m/s to 500 m/s (Fig. 12-left).

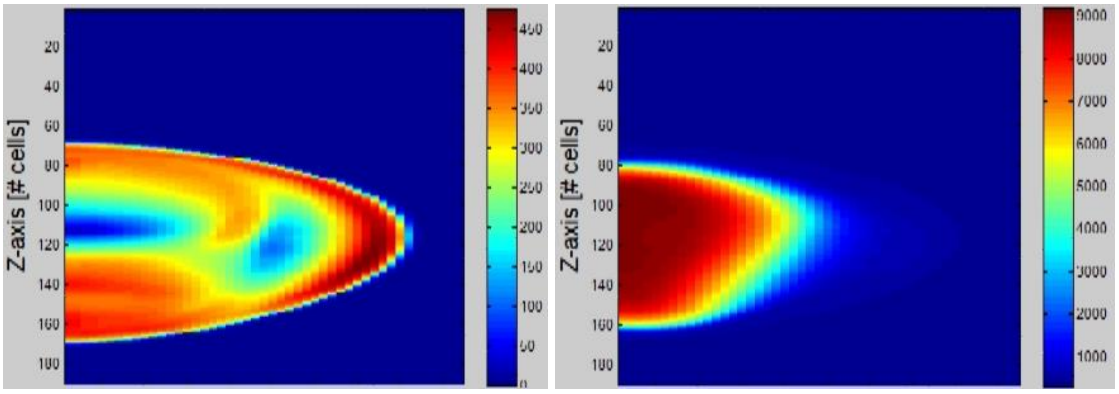

Figure 4.12: Kernel velocities (left) and temperatures (right) for the non-resonant dual-pulse plasma at a time of ~0.5 µs after laser energy deposition. Note that the maximum velocity (shown as a countour) is ~500 m/s, while the temperature in these maximum velocity regions range significantly, indicating we will have significant error when employing the constant volume analysis for temperature. [58]

Fig. 12 shows that there is little correlation between velocity and temperature, and we see that high (> 400 m/s) velocity positions correspond to both low (298 K) and high (9000 K) temperature regions (see the case at 0.5 µs in Fig. 4.12). This makes analysis very challenging. However, we do know that though the velocity distribution is unpredictable in the first 0.5 µs, the temperature is very predictable. Accordingly, we could strictly calculate temperature for regions where the velocity is known to be sufficiently small or the temperature is sufficiently high. For early times, sufficiently high temperatures limit error, then the roles reverse at later delays and sufficiently low velocities limit our error. If we examine the 0.5 µs in Fig. 4.12, we see that the red, orange, and yellow regions are all T > 5250 K. The corresponding error plot is shown in Fig. 13 for the T > 5000 K regime.

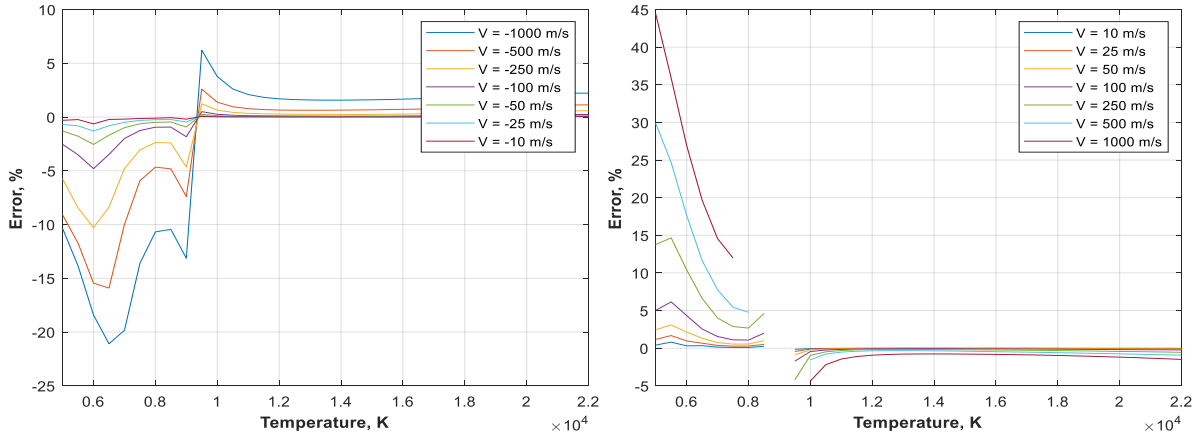

Figure 4.13: Estimated error in the CV case induced by assuming a net zero bulk velocity when the bulk velocity is moving towards the scattering beam (left) or away from the scattering beam (right). Here we examine a much smaller region in hopes of doing selective analysis of temperature where we know our error is small.

Examining the corresponding velocity plot in Fig. 4.13, the maximum velocity in the area of high temperature is ~400 m/s. That puts our error between the green and blue curves, where the maximum possible error is 30%. Though not ideal, we can assume this error is acceptable because of the few locations where it will occur. In summary, we can estimate a region of the plane for the first 1.3 µs where we assume high temperatures exist, as informed by modeling. For the 1.3 µs to 5 µs cases, we evaluate the whole region via CV methods, assuming that small velocities limit our error. For t >5 µs, we use the CP case, where we know error to be <10% due to small velocities.

4.4 Testing a FRS Cell

4.4.1 Experimental Setup

We use a Continuum SI-2000 seeder to seed a Continuum Precision Powerlite II 8000 (which is referred to as the host laser). A software program allows for modulation of the seed laser frequency (of which we expect the host laser to follow). The seeding stability is actively monitored by a photodiode inside the host laser, by triggering an oscilloscope off the Q-switch and measuring the reduction in build-up-time (BUT). The beam is passed through a series of microscope slides and neutral density (Nd) filters, whose sole purpose it to reduce the beam energy. A wavemeter is used to also help monitor the seeding stability, as well as inform the location in frequency space of our laser. A energy normalization photodiode is placed immediately before the chamber, and light passing through the microscope slide is imaged onto it. A beam expansion process is undergone right before the chamber to decrease the intensity per unit area passing through the chamber, as to further decrease the chances of transition saturation. Finally, the light that exits the filter is focused onto a photodiode. The experimental setup is shown below in Fig. 4.14.

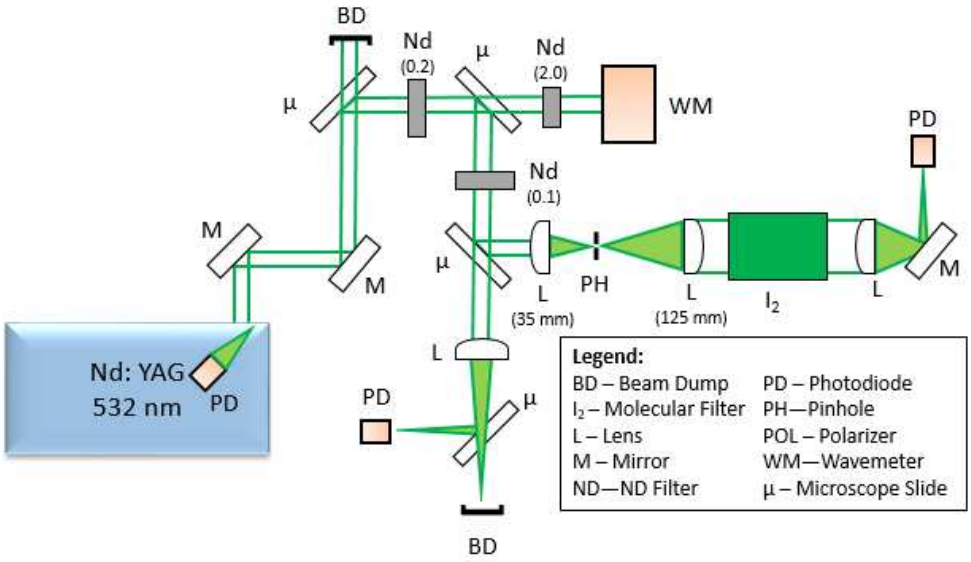

Figure 4.14: Optical layout for characterization of our seeder and scanning of a sample I_2 cell.

4.4.2 Seeding Limitations and Requirements

It became quickly apparent that though the seeder may independently operate at all wavelengths, it does not properly seed the host laser at each of these wavelengths. Recall that there are two parameters necessary for this technique to work. The first is narrow linewidth, and the second is frequency tunability. Neither of these are possible without proper seeding. For these reasons, we perform an experimental scan with our seed laser and monitor how well the host seeds, as well as how much suppression of the beam is seen through the iodine notch filter. The setup is shown in Fig. 4.14. We very quickly realized that there exists some central baseline (λ=532.070 nm) for which the host laser naturally lases. Significant deviation from this ($\Delta\lambda$>0.025 nm) results in an unstable seeding condition where many dropout exist in the data. Additionally, we realized that seeding range is a strong function of input energy. When operating in with a much shorter delay between Q-switch and flashlamp firing, we observed much more consistent seeding over a larger range. Another important factor is the depletion rate of the transition. After running the setup at

high power, very little change in intensity was observed through the filter. Noting the saturation intensity reported in Equation 4.3 of the theory section, we calculated a saturation intensity of 4667 W/cm^2. Accordingly we directed our beam through a series of microscope slides, ND filters, and a telescoping lens arrangement to step down the energy as to not saturate the transition.

4.4.3 Results

For each frequency step executed in the seeder software, a number of traces were recorded, and saved according to the wavemeter output. The transmission percentage was calculated as the integral ratio between the third photodiode and the first photodiode. The result was normalized to a reference condition where the laser frequency was not overlapped with any transitions. After sampling a number of traces for each wavemeter reading, we obtain a wavelength versus transmission plot. Shown in Fig. 4.15 is such a plot, where the errorbars represent the measurement uncertainty of the WM (±0.0005 nm). We then assume an actual wavelength based on a couple parameters. The first is the minimum. The zeros are placed at the minimum of the model. For values other than zero the wavelength is assumed to be at the point of intersection with the model if it is within the bounds of the measurement uncertainty. The wavelength is assumed to be at the point closest to the model at the maximum extent of the errorbars if it does not intersect the model in the bounds of the uncertainty. If the value doesn't intersect with the model, it is left alone (values on far right). Note that filter conditions do not match those designed for in the previous section, as this is a sample cell of side arm temperature of 35°C and an operating temperature of 85°C. Accordingly, this is a separate filter plot from those detailed above.

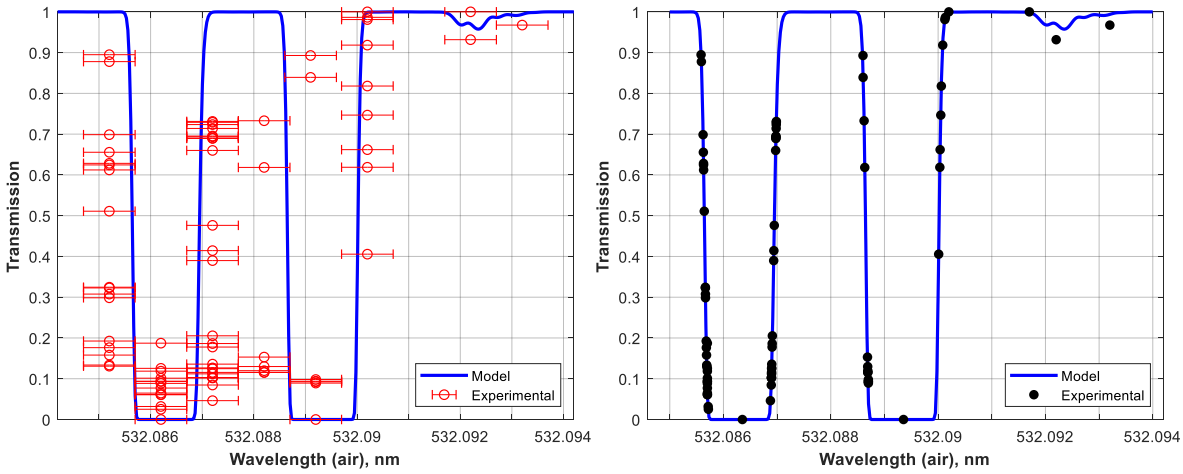

Figure 4.15: Filter transmission as a function of seeder wavelength. The left plot shows a series of data points with the measurement uncertainty represented as errorbars, while the right shows the resulting assumed wavelengths obtained through the technique described above.

Though admittedly it would be good to have better resolution in our measurement of the laser wavelength, we note that the experimental results match the model very well when we assume the wavelength uncertainty. Hoping to maintain full suppression over a long time range when we move towards planar FRS, we set the laser in the center of the first transition, and monitored the transmission. It stayed stable at transmission ~0 for more than 15 minutes. This demonstrates successful tuning of our seeder host system to a transition of iodine absorption, such that significant suppression of elastically scattered light exists.

4.5 Conclusions

Moving towards implementation of an FRS cell in planar combined Rayleigh/Thomson scattering experiments, we note some general precautions. First, the energy has to be high leaving the laser. We can successfully seed our laser across a wide variety of wavelengths, provided we have enough energy. Contrarily, our energy entering the chamber has to be low. We must ensure

we are not saturating the transition when we run planar FRS. This will be hard to monitor when we are running scattering in our chamber, though we anticipate much lower beam energy passing through the filter. We suggest the use of multiple Nd filters and extensive energy measurements before installation of the filter and ICCD.

We can successfully seed inside the transition stably and see zero transmission if these two preceding conditions are met. If the laser doesn't warm up in the iodine absorption region, we can toggle the slider until we see it reach a stable condition inside the notch.

Currently, we cannot apply any kind of feedback to control our laser as is to maintain our location in wavenumber space, however the laser seems to be stable enough to remain inside the notch to not completely leave it. We have two options, modify our seeder so that we can apply a bias voltage, or do real time measurements of our transmission and normalize our data to that. If we develop a real time monitoring system with feedback, we need to imbed in the code a means of differentiating between a small peak and noise (for which both yield non-zero integrals). Additionally, we should design the cell with a much lower side arm pressure such that $dT/d\lambda$ is large inside the notch. Right now, when we are in the notch, we have little to no idea where we are in wavelength space since small amounts of noise significantly change our estimated wavelength. If the valley were more abrupt and less flat, we would have better knowledge of our wavelength, which will allow us to better modify our seeder wavelength and know how much suppression is happening through the non-reference cell that gets imaged on the ICCD (necessary for data corrections or normalizations based on transmission in planar FRS).

CHAPTER 5:

Conclusions

The objective of this thesis is to investigate plasma properties and ignition characteristics of an extension from the dual-pulse plasma formerly developed by our group to a resonant dual-pulse plasma. This technique primarily addresses the issue of large input energies required for laser ignition, and has demonstrated successful reduction of the minimum ignition energy (MIE) necessary for complete combustion with similar efficiencies and lean limits to the non-resonant dual-pulse plasma. Chapter 2 addressed existing gaps in literature for non-resonant plasmas, and determined plasma properties and ignition characteristics that would be compared to the same parameters of the resonant dual-pulse plasma. Chapter 3 discusses the development and characterization of the new resonant dual-pulse plasma. Chapter 4 then described current inhibitions to full comprehension of plasma parameters, and presented a proposed solution to these issues. This chapter serves to evaluate the four aforementioned plasmas relative to each other and detail the direction of the project for the future.

5.1 Summary

5.1.1 Plasma Electron Densities

The electron densities for each plasma under investigation are shown in Fig. 5.1. We note that no significant differences exist between the three ignition capable plasmas (NIR single pulse, and the two dual-pulse plasmas). The REMPI preionization pulse has lower electron density, and decays much more rapidly, likely due to the small amount of deposited energy. Most significantly, the REMPI dual-pulse plasma is able to form the most electron dense plasma with a combined 40

mJ of pulse energy. This is a 33% reduction from the single pulse NIR and non-resonant dual-pulse plasmas, which use 60 mJ of incident laser energy.

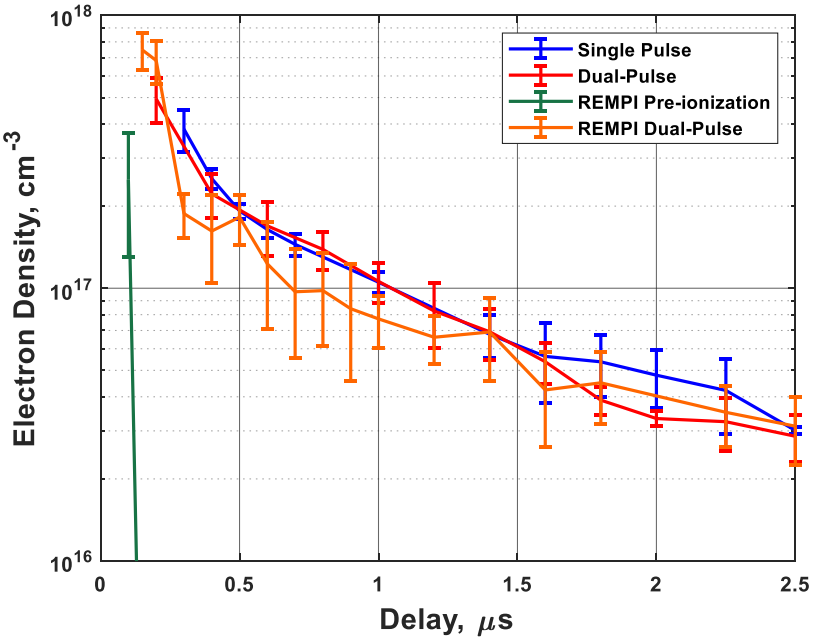

Figure 5.1: Plasma electron density histories for the plasmas of interest. Note that none of the ignition capable plasmas have significantly different electron densities.

We report maximum measureable electron densities of n_e~3.8x10^{17} cm^{-3} at 300 ns for the single pulse plasma, n_e~5.0x10^{17} cm^{-3} at 200 ns for the dual-pulse plasma, n_e~2.5x10^{17} cm^{-3} at 100 ns for the resonant preionization pulse, and n_e~7.5x10^{17} cm^{-3} at 150 ns for the resonant dual-pulse plasma. We observe electron temporal profiles in the resonant case that are similar to non-resonant dual-pulse plasmas (and single pulse plasmas) using ~2/3 of the (delivered) energy. It is significant to note that this can be improved upon by changing the proportion of energy committed to each leg of ionization. In this scenario, only 3 mJ are used for preionization, and 37 mJ are used for energy addition. From experience with the non-resonant dual-pulse case, we know that full breakdown is elucidated more easily by increasing the preionization energy than increasing the energy addition pulse. If we can approach a condition similar to the non-resonant case, where 1/3

of the energy is used for preionization, and 2/3 is used for energy addition, we can more accurately compare the two plasmas. Currently, we are limited by the output energy of our laser system.

5.1.2 Plasma Gas Temperatures

Using the combined Rayleigh/Thomson diagnostic over ranges where assumptions of chemical equilibrium, constant pressure, and constant volume scenarios apply, we obtain Fig. 5.2, showing peak temperatures of the plasma kernel at varying times. It is important to note two things. First, the use of Rayleigh scattering analysis becomes increasingly difficult at later delays, due to complex flow fields and the ability to only measure temperature in one dimension. Therefore, variation in probe beam location could result in different temperatures than the ones shown here. Secondarily, the goal of measuring the plasma is to inform ignition characteristics. However, the mixtures we employ these diagnostics in contain no fuel content. We know that in the presence of fuel, a toroid has fully formed and began propagating through the chamber on the timescale of hundreds (and even tens) of microseconds. In order to properly address ignition characteristics, Rayleigh/Thomson scattering should be performed in fuel-air mixtures. The difficulty in this is that each trial requires recharging of the chamber and proper diffusion (mentioned later in this chapter) when fuel is introduced, so the timescale required to obtain a statistically significant result becomes immense.

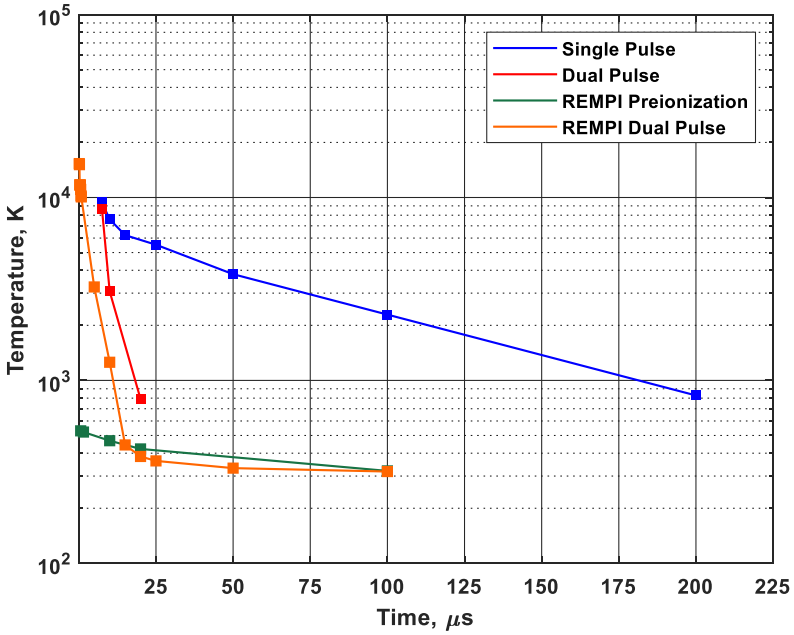

Figure 5.2: Plasma gas temperature histories. Note that both dual-pulse cases cool to below 1000 K withing the first 25 µs, while the single pulse case takes nearly 200 µs.

We report maximum measureable gas temperatures of T~9,400 K at 7.5 µs for the single pulse plasma, T~8,700 K at 7.5 µs for the non-resonant dual-pulse plasma, T~530 K at 600 ns for the resonant preionization plasma, and T~15,300 K at 150 ns for the resonant dual-pulse plasma. We note that this result is dependent on the assumption of constant volume at early times, which has yet to be analyzed for the resonant case. Shlieren imaging would best serve this purpose. Additionally, we observe that the dual-pulse cases typically cool much more rapidly than the single pulse case, but it is yet to be determined whether this is a limitation due to the 1-D measurement technique, or a result of complex fluid dynamics. We will investigate this using 2-D FRS in the future to understand this phenomena better in the future.

5.1.3 Ignition Testing

5.1.3.1 Combustion Efficiency

Using the pressure histories of ignition and calculated heat release rates, we obtain Fig 5.3, detailing combustion efficiencies in the three fuels for the three plasmas of interest. We see that in all three cases, the dual-pulse plasmas have higher combustion efficiencies, and extend the lean limit, effectively shifting the curves up and to the left. Though it is important to note that this could be attributed to differences in deposited energy for the REMPI dual-pulse case, we can confidently conclude that the use of dual-pulse plasmas increases combustion efficiencies and extends the lean limit. The lean limits for single pulse NIR plasmas are determined to be ϕ=0.12 for hydrogen, and ϕ=0.53 for methane, while past experimentation has demonstrated a lean limit of ϕ=0.70 for propane. Corresponding values for the non-resonant dual-pulse plasma are ϕ=0.11 for hydrogen, ϕ=0.50 for methane, and ϕ=0.60 for propane which exactly match the lean limits of the resonant dual-pulse case. We note that hydrogen has the closest lean limits when comparing ionization mechanisms, and encourage further demonstration of this effect in other fuels.

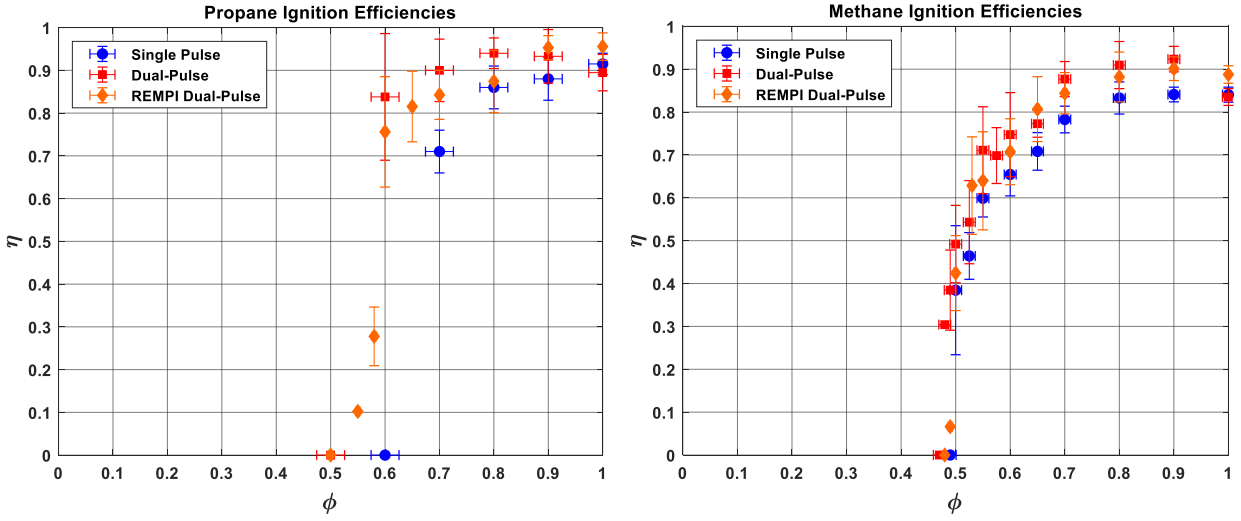

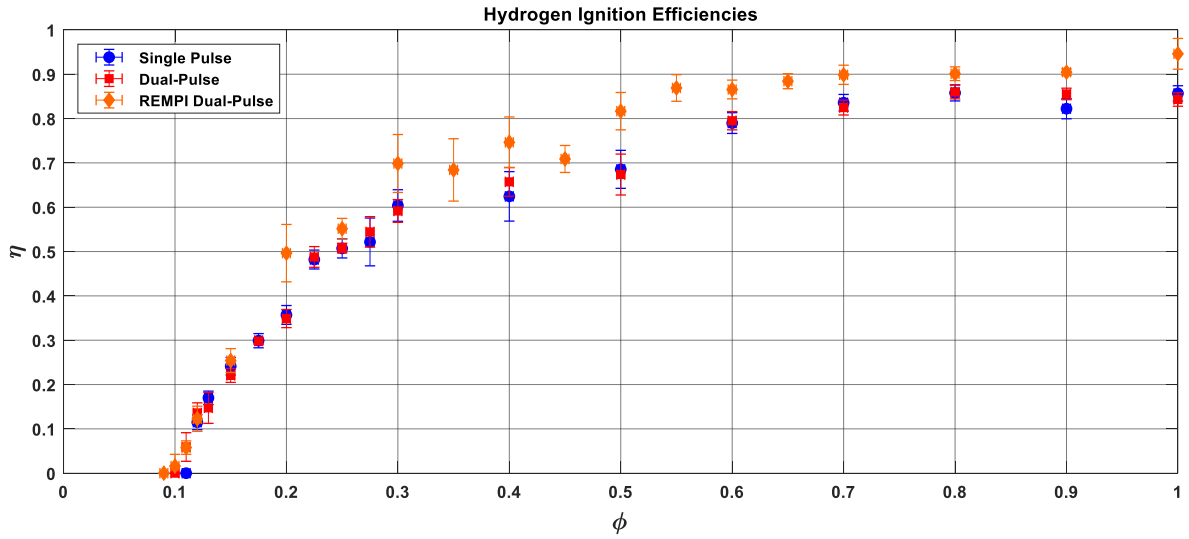

Figure 5.3: Combustion efficiencies for the three ignition capable plasmas in propane (top left), methane (top right) and hydrogen (bottom). Note how both dual-pulse cases exhibit higher combustion efficiencies for most equivalence ratios in all three fuels. Lean limits are also extended, as can be observed in the leftward shift of the curve.

5.1.3.2 Kernel Shapes from OH Chemiluminescence*

OH* chemiluminescence for single pulse NIR plasmas in methane-air mixtures showed similar three lobe structures to those well established for propane-air mixtures, while hydrogen-air mixtures tended to have much more rapid radial growth when compared with longitudinal growth of the third lobe. Most importantly, for all mixtures, the undesirable third lobe was present. For the non-resonant dual-pulse plasma, the preionization channel was clearly seen, and had sufficient energy to dictate kernel shape for near stoichiometric conditions in hydrogen-air mixtures. Suppression of the third lobe occurred in both hydrogen and methane near stoichiometric conditions, but the third lobe could be observed at extended delays for the leaner cases. Hydrogen-air mixtures ignited much more rapidly for both plasmas when compared with methane-air mixtures. The resonant dual-pulse plasma exhibited similar kernel shapes to single pulse ignition, revealing that third lobe formation occurs in all ignition events of all fuels at all equivalence ratios. Lean cases exhibited rapid quenching of the third lobe within the first few hundred microseconds.

Many showed separation of the third lobe from the toroid. For this reason, we speculate that deposited energy may be greater, causing efficiency to rise.

5.1.3.3 Investigation of Axial Offset on Dual-Pulse Ignition

An investigation into the axial offset between waists for the non-resonant dual-pulse plasmas showed that it is preferable to focus the energy addition beam further downstream from the preionization pulse rather than upstream, if perfect overlap (Δz=0.0 mm) cannot be achieved. For downstream focusing, third lobe suppression is stronger and ignition probability is increased. For upstream focusing, the energy addition pulse acts more like a single pulse plasma, responsible for both MPI and EAI and forming a three lobe structure more frequently. At near stoichiometric conditions, upstream focusing can result in a four lobe structure with the fourth lobe centered near the preionization channel. This fourth lobe typically detaches from the main toroid much like the third lobe. We find that zero axial offset (Δz=0.0 mm) results in the most efficient and most probable ignition with the lowest lean limit. The benefit of lean limit extension completely ceases by an offset of 2 mm, while kernel flame propagation directions are highly variable in the region of ±0.5 mm.

For the resonant dual-pulse plasma, no such effect was observed. Unlike the non-resonant case, we observe negligible differences in combustion efficiency as a function of the waist offset. All traces exhibit similar trends and identical lean limits. We hypothesize the difference to be due to the energy deposition ratios of each laser though it is important to note that our setup records only the delivered, not deposited (absorbed) energy, and it is the latter that is more relevant. For the non-resonant case, the ratio of the preionization pulse energy to the secondary pulse energy is 1:2 (E_{UV}=20 mJ, E_{NIR}=40 mJ). For the resonant case, the ratio is approximately 1:12 (E_{REMPI}=3

mJ, E_{NIR}=37 mJ). We do report a slight increase in the combustion efficiency around the lean limit for the ideal overlapped case, though it is not significant. No variation in the waist offset altered the shape of the kernels. We recommend further investigation into this phenomena with higher preionization energy (E_{REMPI}=13 mJ, E_{NIR}=26 mJ for example).

5.1.4 Filtered Rayleigh Scattering

We have demonstrated that filtered Rayleigh scattering is possible with our current equipment. We illustrated proper filter scanning, recognizing that the measurement uncertainty in the wavemeter is large. It is important when using this laser to have high enough power for the system to seed well, while simultaneously using low energy through the chamber (which shouldn't be difficult when imaging scatter). We have shown that though elevated temperatures and bulk velocities are something to be aware of, the plasmas we are interested in should not possess high enough variations to produce large error in estimations of temperature or electron density. We have also selected a specific transition, and corrected our observed intensity curves so that we can properly estimate temperature without inducing this error.

5.2 Sources of Error and Potential Improvements

5.2.1 Diffusion Characteristics of Fuel-Air Mixtures

One concern that arose over the course of experimentation was the tendency of certain fuels (primarily propane and methane) to have higher ignition probabilities when the preheat time increased. The most logical explanation for this trend relates to the diffusivity of the fuel. The goal of this section is to characterize the temporal diffusion through the chamber, to understand how

much preheat time is necessary to be able to assume a homogeneous distribution of fuel, devoid of localized fuel concentrations and corresponding variations in equivalence ratio. When filling the chamber, we fill with the partial pressures of the constituents, beginning with the fuel and following with air. Due to the location of the inlet of the chamber (shown in Fig. 5.4), we can assume that the sequencing of constituent addition dictates high concentrations at the two ends of the chamber. Since the length in the y-direction is significantly less than that in the x-direction, we assume constant concentration at all radius values from the central axis of the chamber, reducing the problem to 1-D.

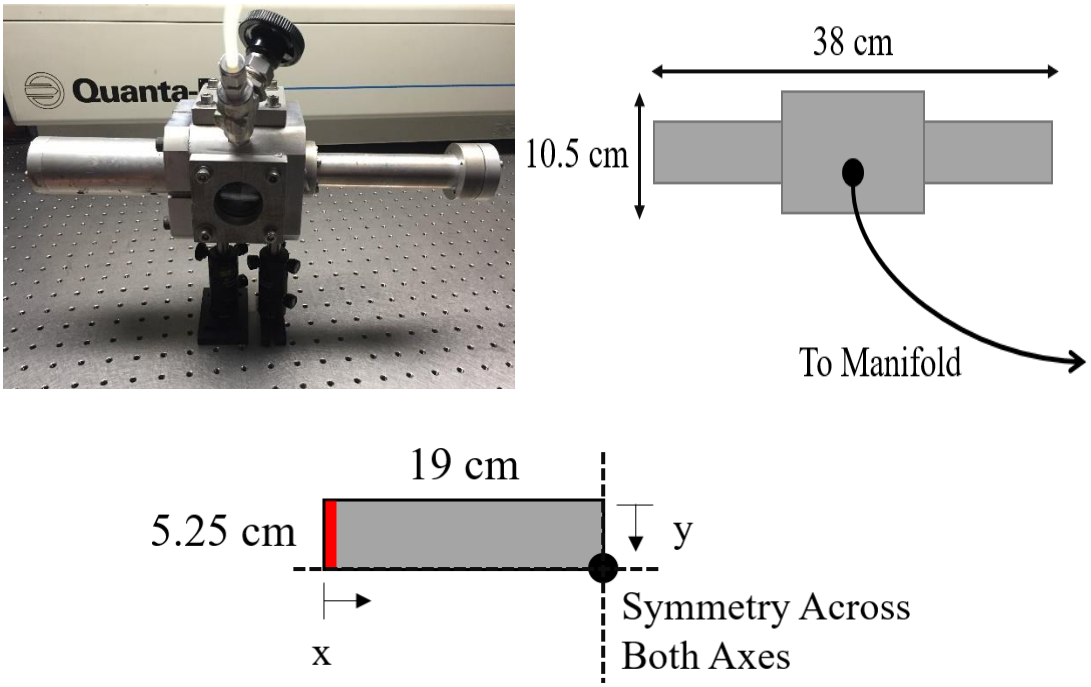

Figure 5.4: The custom chamber used for ignition experimentation (top left). Sapphire windows are used to withstand the elevated pressures inside the chamber, while heating tape (not shown) is used to raise the surface temperature to 50°C, promoting mixing in the chamber. Also shown is the assumed chamber geometry in a birds eye view (top right), from which we assume our 2-D modeling geometry (bottom center).

To calculate the concentration as a function of location and time, we begin with Fick's second law, which states that for 1-D diffusion the first derivative of the concentration (C) with

respect to time (t) is equivalent to the product of some diffusion constant (D) with the second derivative of the concentration with respect to position (x).[80]

$$\frac{dC}{dt} = D\frac{d^2C}{dx^2} \tag{5.1}$$

The diffusion constant however is not constant, but varies with mixture parameters. We investigate this variation in Appendix B, but note that the variation is not significant over the equivalence ratios employed. We therefore use well established diffusion coefficients (D_{prop}=0.1144 cm^2/s, D_{meth}=0.2382 cm^2/s, D_{H2}=0.611 cm^2/s) as found in literature and correct them by the temperature relationship mentioned in the prior equation when necessary.[83–88]

Returning to Fick's second law (Eqn. 5.1) and assuming a constant diffusion coefficient, we propose the solution for 1-D free diffusion where we assume a reflective wall at some position x_o. The derivation for the solution of Einstein's diffusion equation and Brownian motion is well outlined in the lecture notes from PHYS498 from University of Illinois at Urbana-Champaign, but the final expression for the probability of finding a particle at a position x at time t can be described by:[89]

$$p(x,t) = \frac{1}{\sqrt{4\pi D(t-t_0)}}\exp\left[-\frac{(x-x_0)^2}{4D(t-t_0)}\right] + \frac{1}{\sqrt{4\pi D(t-t_0)}}\exp\left[-\frac{(x+x_0)^2}{4D(t-t_0)}\right] \tag{5.2}$$

The second term accounts for diffusion that would exit the chamber if not for a reflective wall. By adding this term, we close the system. We show that this equation does indeed satisfy Fick's second law in Appendix C. We now solve for the distribution of fuel through the chamber as a function of x and t, from both ends of the chamber. Because Fick's law is a linear partial differential equation, the sum of any two solutions is also a solution. So if we model diffusion from each end separately assuming a single reflective surface, the sum of those two solutions should accurately model axial diffusion in the chamber. We admit that complex 2-D geometry and a fixed

domain would better represent the situation we are trying to model. Though the problem is analytically solvable, it has proven too computationally intensive. More sophisticated numerical methods would need to be adopted (as well as initial concentration distribution measurements) in order to more accurately model this in the future. Our approach can be considered valid however by limiting the time domain to a region where little to no fuel has passed the bounds of the far wall. We define this cutoff time to be the point where the concentration at the far wall is 1.5% of the concentration when the fuel is homogenously distributed throughout the chamber. We choose this value so that the hydrogen-air concentration field can be seen at ten minutes. We know that hydrogen-air ignition probability does not increase with greater preheat time after ten minutes, and therefore use it as a metric to evaluate the other fuels. This time corresponds to approximately 55 minutes for propane-air, 30 minutes for methane-air, and 12 minutes for hydrogen-air (by definition). The solution results presented henceforth are normalized in the same manner to this homogenous concentration. An example normalized 1-D concentration for hydrogen-air is shown in Fig. 5.5 for a variety of delays.

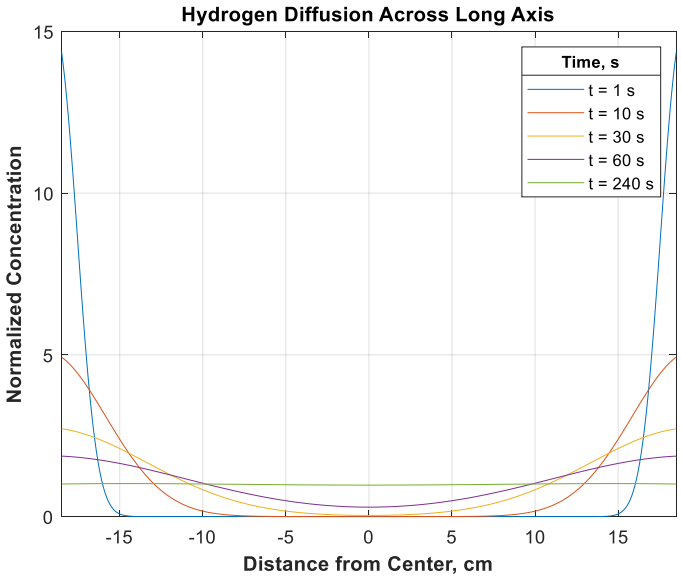

Figure 5.5: Diffusion of hydrogen from the far ends of the chamber to the center. A normalized concentration of one represents a condition where the concentration is equal to the concentration of a uniform homogenous mixture of fuel and air.

Examining the diffusion scenario at a time of 10 minutes, we see that hydrogen air has a standard deviation of 0.03447 (shown in Fig. 5.6). We can assume that mixtures with standard deviations less than this value are thoroughly mixed, as hydrogen-air ignited at all expected equivalence ratios, though we may see good enough homogeneity at standard deviations greater than this value. We also see from the distributions that over the range of 3 minutes 34 seconds to nine minutes, the standard deviation is less than it is at ten minutes, because the two distributions have not yet interacted. We can reduce our preheat time accordingly, and should use a target time of 4 minutes 30 seconds, where the standard deviation is at its minimum.

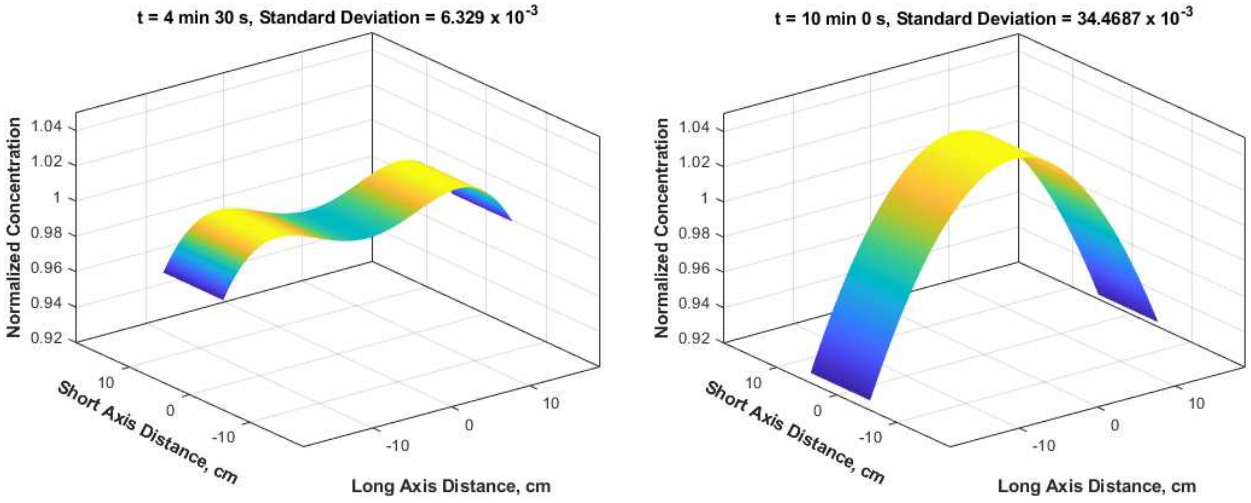

Figure 5.6: Two dimensional concentration distributions for hydrogen-air for the location of smallest standard deviation (left), and for the currently used ten minute preheat condition (right). Note that both figures have the same scale.

Moving onto propane air mixtures, we have similar concentration distributions over a different timescale. The ten minute and minimum standard deviation cases are shown in Fig. 5.7.

The best time to ignite the mixture is 21 min 32 seconds, however the mixture has a lower standard deviation than the limit set by hydrogen over the range of t=17 min-44 min. Most importantly, the 10 minute case used for all ignition experimentation presented in this work is not good. We need to provide more preheat time to promote proper diffusion in the chamber. This is probably why we have the unexpected result of methane igniting at lower equivalence ratios compared to propane. We can expect higher combustion efficiency and probability for lean mixtures, as well as extension of the lean limit, when we increase our mixing time.

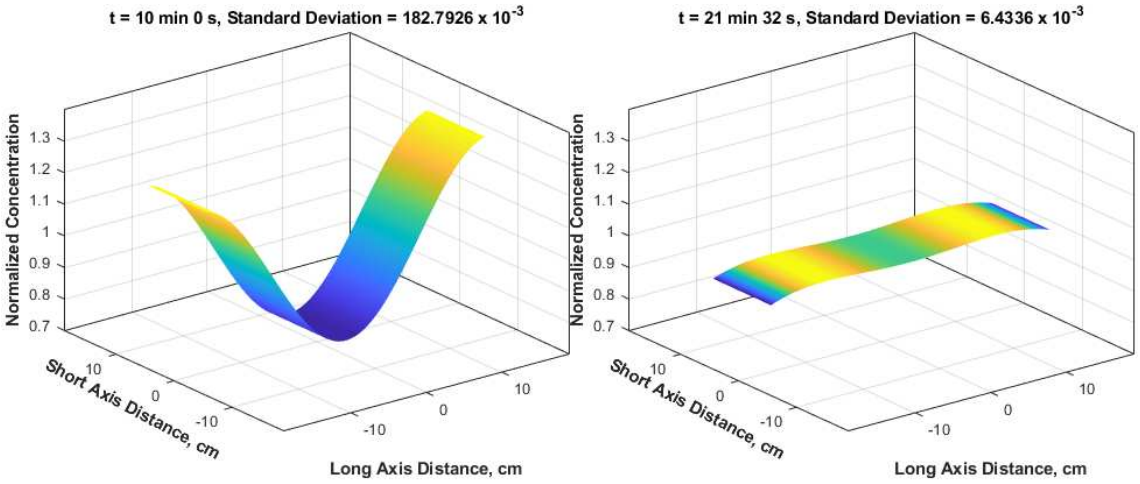

Figure 5.7: Two dimensional concentration distributions for propane-air for the currently used ten minute preheat condition (left), and the time of smallest standard deviation (right). Note that both figures have the same scale.

For methane-air ignition, the best time to ignite the mixture is 11 min, 55 seconds. However the mixture has a lower standard deviation than the limit set by hydrogen over the range of approximately t=9 min–24 min. The 10 minute case is relatively good, and the mixture is pretty close to the low point in the standard deviation curve. The concentration distributions are shown in Fig. 5.8. One important thing to note is the inversion of the curve that occurs as the two peaks interact. Shown also in Fig. 5.8 is the 15 minute case, which is known to have higher ignition probability than the 10 minute case. The reason we see increased ignition probability at 15 minutes

is the distribution of the fuel. We see at ten minutes that the center of the chamber under represents the average air to fuel ratio and at fifteen minutes that the center of the chamber over represents the average air to fuel ratio, resulting in a higher probability of localized ignition, which can spread more easily once it has that catalyzing push.

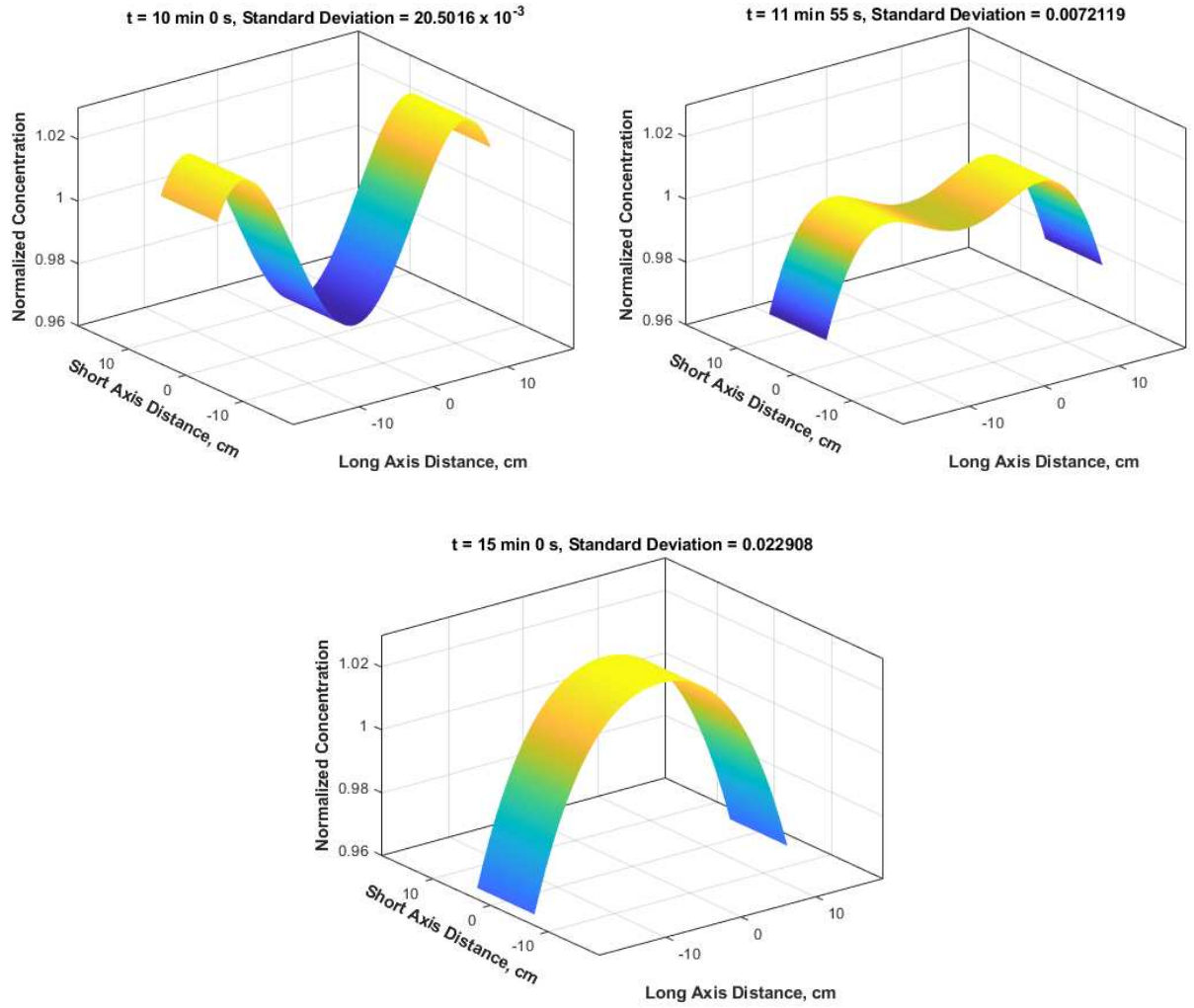

Figure 5.8: Two dimensional concentration distributions for propane-air for the currently used ten minute preheat condition (left), the time of smallest standard deviation (right), and the fifteen minute preheat condition where ignition probability increases (bottom). Note that all figures have the same scale.

Returning back to the definition of the diffusion coefficient, we know that the diffusion coefficient (D) scales with temperature (T) by $D \alpha T^{3/2}$ as noted previously. Assuming all other parameters held constant, the corresponding diffusion coefficient for a high temperature condition can be related to the low temperature diffusion coefficient by:

$$D_{HighT} = D_{LowT} * \frac{T_{High}^{\frac{3}{2}}}{T_{Low}^{\frac{3}{2}}} \tag{5.5}$$

There are two reasons why we want to investigate this relationship in further detail. The first is to determine if it is necessary to integrate conduction and convection equations from the high temperature wall to the low temperature mixture, or if assuming a mean temperature is a sufficient approximation (and a constant diffusion coefficient is a decent estimate). Secondarily, we want to determine if we can reduce the amount of preheat time necessary for ignition by increasing the preheat temperature. Summarizing the fuels of interest, the best time to ignite the mixtures of interest corresponds to approximately 5 minutes for hydrogen, 12 minutes for methane, and 22 minutes for propane. If we can lower the necessary preheat time for propane and methane, we can collect data with greater efficiency. By performing the same analysis described above, we can obtain the standard deviation for a variety of preheat temperatures. Shown in Fig. 5.9 (left) is the standard deviation for propane-air mixtures. By then taking the times corresponding to the minima of the standard deviation curves, we can estimate the target times as a function of preheat temperature. This is shown in Fig. 5.9 (right).

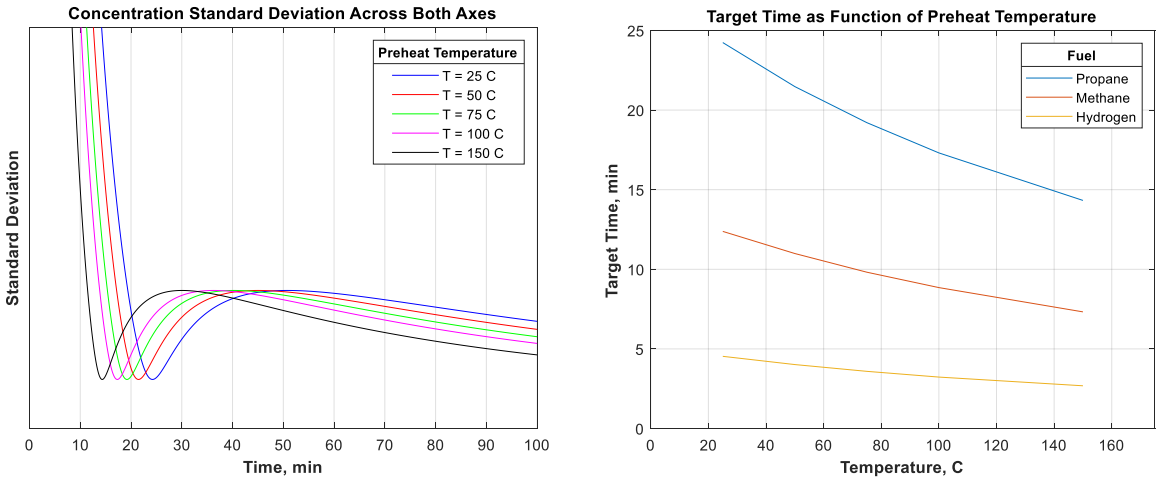

Figure 5.9: Standard deviations in the concentration profiles of propane-air mixtures at a variety of preheat conditions (left), and corresponding target times developed from standard deviation minima for the three fuels of interest (right). Note that the propane case has the highest sensitivity to the preheat temperature, though it does not affect target time enough to encourage higher preheat values.

We use Fig. 5.9 to evaluate the concerns addressed earlier (constant diffusion constant and possibility of increased experimentation efficiency). With regards to the constant diffusion coefficient, we do not see significant enough variation in the concentration distribution to indicate that we need to account for conductive and convective terms and pointwise time resolved changes in the diffusion coefficient based on temperature. If we examine the case most sensitive to preheat temperature (propane-air), we see that assuming either 25°C (no preheat), or 50°C (instantaneous preheat) results in a variation in target time of only a few minutes. For this reason, we assert that future investigations into chamber diffusion can be accurately modeled with a constant value for the diffusion coefficient. We encourage implementation of a mean temperature based on the heated wall temperature and the cool fuel air mixture. Unfortunately, this result discourages the possibility of decreasing preheat time by increasing preheat temperature. If we preheat the chamber by a full 100°C and assume it instantaneously heats the mixture, we only save about four minutes in

experimentation. We therefore conclude that feasible preheat temperatures do not significantly alter the time required for proper mixing to occur.

5.2.2 Efficiency Trends at High Equivalence Ratios

Throughout the course of this work, we regularly noticed a downward trend of combustion efficiency near stoichiometric conditions. A couple examples of this exist in Figs. 2.13, 2.21, and 3.18. There are a couple explanations for this. The first is extremely high pressure gradients with respect to time. Most noticeably for hydrogen, a rapid oscillation in pressure occurred during the pressure rise, with greatest amplification at the peak. We hypothesize this to be due to the seating and unseating of the windows against the chamber. The chamber is sealed well and holds strong vacuum, and though we do account for leakage in our calculations, this kind of window reverberation experienced at high equivalence ratios could cause unintended fluid dynamic effects and fuel pockets which are undesirable and result in unburned fuel. This pressure reverberation is shown in Fig. 5.10 below, where hydrogen-air of equivalence ratio ϕ=1.0 is ignited with the REMPI dual-pulse plasma with initial conditions of P_0=1bar and T_0=323 K.

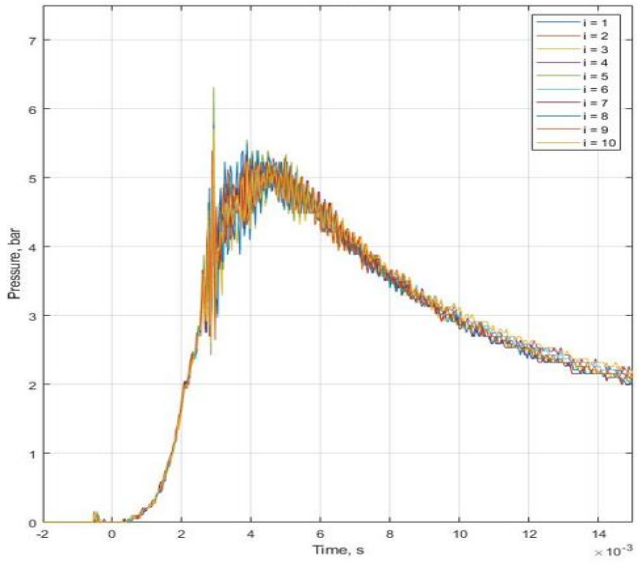

Figure 5.10: High pressure, high equivalence ratio ignition of hydrogen using a dual-pulse REMPI plasma. Notice that though there is great agreement between tests, the peak pressure comes significantly before the peak of a running average centerline and significant oscillation in pressure occurs near this point.

The second explanation is that widely accepted data analysis techniques terminate heat release prematurely. As seen with the pressure traces in multiple occurrences (Figs. 2.12, 2.20 and 3.17), at near stoichiometric conditions there exists a secondary rise in pressure in the hundreds of milliseconds regime, in which additional heat release could be occurring. This is seen for all fuels, but is most prominent for methane-air mixtures. Though the reason for this second spike in pressure is unknown, it is likely that additional integration over this area will result in efficiencies much closer to one.

5.2.3 Chamber Redesign

The chamber we currently use was designed in a manner that places the windows orthogonal to the chamber arms. Though simple and easy to machine, this prevents some difficulties when aligning and operating a series of laser systems. For the vast majority of the experiments that are performed in this chamber, the laser light is focused down inside the chamber. When selecting mirrors and placing the chamber, it is a regular struggle trying to find an position where all beams pass through the chamber, yet the back reflections from the windows don't focus onto any of the upstream optics. Particularly for dual-pulse Rayleigh/Thomson scattering (shown in Fig 5.11, below), where there are three beams focused inside the chamber, it becomes common practice to tilt or rotate the chamber off axis to deflect back reflections out of the main beam, where they can be dissipated inside beam dumps.

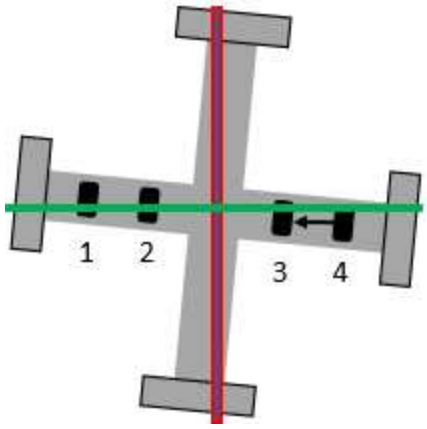

Figure 5.11: A sample image showing the chamber with an induced tilt angle and baffles (seen in black).

The difficulty lies in the scattering associated with large tilt angles. For the setup shown above we show that in some cases, we have to even move the baffles closer to the center of the chamber to ensure that the beam does not clip on the baffles, resulting in particle sputtering and eventual Mie scattering in the beam. Particularly when we become interested in planar FRS, this will be a problem. The solution to this would be to redesign our chamber in a manner that places windows at an angle from the chamber arms. Ideally, the angle between the incident beam and the window normal would match the Brewster angle, and no light would be reflected off the surface. For sapphire windows, the corresponding Brewster angle is $\theta_B = 60.535°$, while for UV fused silica, $\theta_B = 56.310°$. We target an average of the two of $\theta_B = 58.423°$ as experiments for ignition use the former and Rayleigh/Thomson scattering the latter. Unfortunately, due to window thicknesses and sealing requirements, a Brewster angle window could not be an adaptation to our existing chamber, but would rather require the design and assembly of a completely new chamber. However, for the chamber in existence we still perform a redesign that will have better qualities than the orthogonal windows we have now. Using SolidWorks and existing files for the chamber arm, we have developed a new chamber arm with a corresponding incidence to window normal

angle of $\theta = 16.699°$. Though the full drawings are presented in Appendix D, the isometric view of the redesigned chamber arm is show in Fig. 5.12 below.

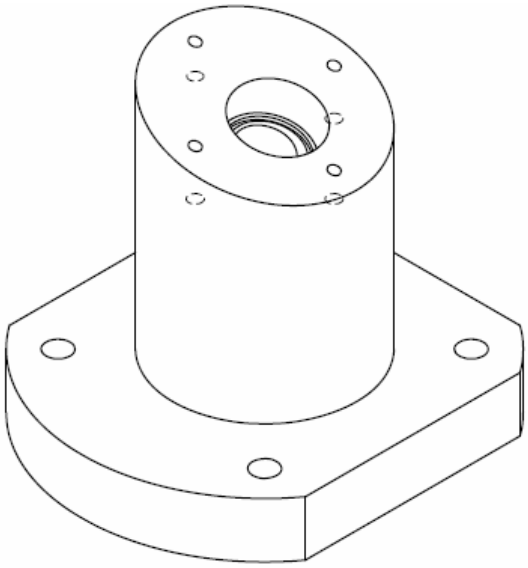

Figure 5.12: An isometric view of the redesigned entry arm. This arm typically admits ionization beams, and introducing a slight tilt to it would make alignment and back reflection mitigation significantly easier.

5.3 Future Work

The current focus of dual-pulse laser ignition is advancement of both the diagnostic and understanding of the parameters that influence plasma properties. For each of the aforementioned plasmas, the electron densities and temperatures are highly dependent on a number of parameters. Beam quality, focusing conditions, laser fluence, ambient/target medium, all have significant impacts. Being able to characterize plasma parameters as a function of all of these input conditions will allow for a better understanding of how we can optimize a plasma to match desirable plasma conditions for each separate application.

One immediately interesting study would be the effects of preionization energy on plasma parameters and combustion characteristics. For the existing resonant dual-pulse case, preionization energies have not exceeding 5 mJ. Being able to match the preionization energy of the non-resonant equivalent (20 mJ) is imperative to being able to properly understand the differences between the two plasmas.

Another interesting study would be varying focusing conditions to selectively target regions of localized high fuel content when compared with the average. If we can accurately model the diffusion of the fuel in the chamber and ignite mixtures by forming flame fronts where we know fuel content characteristics are favorable, we may be able to ignite mixtures where the average equivalence ratio is lower than the lean limit presented here.

More importantly, existing gaps are present in the determination of temperature over the lifetime of the plasma. Developing a model or technique that accurately estimates temperature as a function of observed intensity across all times is an encouraged point of study. Also encouraged is the employment of planar FRS, which will increase the dimensionality of the study from 1-D to 2-D, decreasing the sensitivity of temperature measurements on location of the probe beam.

BIBLIOGRAPHY

1. Herdin, G., Klausner, J., Weinrotter, M., Graf, J. & Wimmer, A. GE Jenbacher's Update on Laser Ignited Engines. *2006 ASME Intern. Combust. Engine Div. Fall Tech. Conf.* 2006 (2005).

2. Bradley, D., Sheppard, C. G. W., Suardjaja, I. M. & Woolley, R. Fundamentals of high-energy spark ignition with lasers. *Combust. Flame* **138**, 55–77 (2004).

3. Dumitrache, C. *et al.* A study of laser induced ignition of methane – air mixtures inside a Rapid Compression Machine. *Proc. Combust. Inst.* **36**, 3431–3439 (2017).

4. Kopecek, H. *et al.* Laser Ignition of Methane-Air Mixtures at High Pressures and. *J. Eng. Gas Turbines Power* **127**, 213–219 (2004).

5. Herdin, G. *et al.* Laser Ignition: A New Concept to Use and Increase the Potentials of Gas Engines. *2005 ASME Intern. Combust. Engine Div. Fall* **10**, 1352 (2005).

6. Dumitrache, C., Vanosdol, R., Limbach, C. M. & Yalin, A. P. Control of Early Flame Kernel Growth by Multi-Wavelength Laser Pulses for Enhanced Ignition. *Sci. Rep.* **7**, 1–8 (2017).

7. Dumitrescu, C. *et al.* Fiber-Optic Spark Delivery for Gas-Phase Laser-Induced Breakdown Spectroscopy. *Appl. Spectrosc.* **61**, 1338–1343 (2007).

8. Yalin, A. P. *et al.* Fiber Optic Delivery of Nanosecond Laser Pulses for Spark Formation in Gases. *Laser Appl. to Chem. Secur. Environ. Anal.* **7**, (2006).

9. Mahamud, R. *et al.* Dual-Pulse Laser Ignition Model. *Phys. Fluids* **30**, (2018).

10. Tropina, A. A., Shneider, M. N. & Miles, R. B. Modeling of Dual-Pulse Laser Ignition. *55th AIAA Aerosp. Sci. Meet.* 2017 (2017).

11. Tropina, A. A., Miles, R. B. & Shneider, M. N. Mathematical Modeling of Dual-Pulse Laser Ignition in a Turbulent Flow. *J. Propuls. Power* (2017).

12. Dumitrache, C., VanOsdol, R., Limbach, C. M. & Yalin, A. P. Laser Ignition of Propane-Air Mixtures Using a Dual-Pulse Technique. *55th AIAA Aerosp. Sci. Meet.* 1–8 (2017). doi:10.2514/6.2017-1976

13. Dumitrache, C., Limbach, C. M. & Yalin, A. P. Threshold characteristics of ultraviolet and near infrared nanosecond laser induced plasmas. *Phys. Plasmas* **23**, (2016).

14. Butte, C., Yalin, A. P. & Dumitrache, C. Dual-Pulse Laser Ignition Using Oxygen REMPI Preionization. *2019 AIAA Aerosp. Sci. Meet. AIAA Aviat. Forum* (2019).

15. Ronney, P. D. Laser Versus Conventional Ignition of Flames. *Opt. Eng.* **33**, 510–522 (1994).

16. Hill, R. A. Ignition-Delay Times in Laser Initiated Combustion. *Appl. Opt.* **20**, 2239–2242 (1981).

17. Mcguire, S., Chng, T. L. & Miles, R. B. Nanosecond Time-Resolved 2 + 2 Radar REMPI Measurements Performed in Molecular Nitrogen ∗. *Am. Inst. Aerosp. Aeronaut.* (2013).

18. Morgan, C. G. Laser-Induced Breakdown of Gases. *Reports Prog. Phys.* **38**, 621–665 (1975).

19. Adelgren, R., Elliott, G., Knight, D., Zheltovodov, A. & Beutner, T. Energy Deposition in Supersonic Flows. *AIAA Proc.* (2001).

20. O'Briant, S. A., Gupta, S. B. & Vasu, S. S. Review: laser ignition for aerospace propulsion. *Propuls. Power Res.* **5**, 1–21 (2016).

21. Brieschenk, S., Kleine, H. & O'Byrne, S. Laser Ignition of Hypersonic Air – Hydrogen Flow. *Shock Waves* **23**, 439–452 (2013).

22. Negishi, J., Horisawa, H. & Kimura, I. Mixing and Reaction Enhancement Characteristics of Laser-Induced Plasmas and Detonations in Laser-Augmented Scramjets. *AIP Conf. Proc.* **830**, 151–162 (2006).

23. Yu, Y. *et al.* Stabilization of a Premixed Methane-Air Flame with a High Repetition Nanosecond Laser-Induced Plasma. *Opt. Laser Technol.* **92**, 24–31 (2017).

24. Wermer, L., Lefkowitz, J. K., Ombrello, T. & Im, S. kyun. Ignition Enhancement by Dual-Pulse Laser-Induced Spark Ignition in a Lean Premixed Methane-Air Flow. *Proc. Combust. Inst.* **000**, 13–33 (2018).

25. Phuoc, T. X. & White, F. P. An optical and spectroscopic study of laser-induced sparks to determine available ignition energy. *Proc. Combust. Inst.* **29**, 1621–1628 (2002).

26. Harmon, R. S. *et al.* LIBS: a new versatile field-deployable real-time detector system with potential for landmine detection. *Proc. SPIE* **5089**, (2003).

27. Harmon, R. S., Lucia, F. C. De, Miziolek, A. W. & Lapointe, A. The Use of Laser-Induced Breakdown Spectroscopy to Discriminate Between Landmines and Other Objects. (2004).

28. Harmon, R. S. *et al.* Discrimination and Identification of Plastic Landmine Casings by Single-Shot Broadband LIBS. *Proc. SPIE* **5794**, (2005).

29. Palanco, S., Lo, C. & Laserna, J. J. Design , construction and assessment of a field-deployable laser-induced breakdown spectrometer for remote elemental sensing. *Spectrochim. Acta Part B* **61**, 88–95 (2006).

30. Palanco, S. *et al.* Test of a stand-off laser-induced breakdown spectroscopy sensor for the detection of explosive residues on solid surfaces. *J. Anal. At. Spectrom.* **21**, 55–60 (2006).

31. Lucena, P., Tobaria, L. M. & Laserna, J. J. Standoff LIBS detection of explosive residues behind a barrier. *J. Anal. At. Spectrom.* **24**, 1123–1126 (2009).

32. Pichahchy, A. E., Cremers, D. A. & Ferris, M. J. Elemental analysis of metals under water using laser-induced breakdown spectroscopy. *Spectrochim. Acta Part B* **52**, 25–39 (1997).

33. Lazic, V., Colao, F., Fantoni, R. & Spizzicchino, V. Recognition of archeological materials underwater by laser induced breakdown spectroscopy B. *Spectrochim. Acta Part B* **60**,

1014–1024 (2005).

34. Wiens, R. C. *et al.* Combined remote mineralogical and elemental identification from rovers : Field and laboratory tests using reflectance and laser-induced breakdown spectroscopy. *J. Geophys. Res.* **107**, (2002).

35. Erfani, R., Zare-Behtash, H. & Kontis, K. Influence of shock wave propagation on dielectric barrier discharge plasma actuator performance. *J. Phys. D. Appl. Phys.* **45**, (2012).

36. Little, J., Nishihara, M. & Adamovich, I. High-lift airfoil trailing edge separation control using a single dielectric barrier discharge plasma actuator. *Exp* **48**, 521–537 (2010).

37. Corke, T. C., Enloe, C. L. & Wilkinson, S. P. Dielectric Barrier Discharge Plasma Actuators for Flow Control. *Annu. Rev. Fluid Mech.* **42**, 505–529 (2010).

38. Wei, Q., Niu, Z., Chen, B. & Huang, X. Airfoil Roll Control by Bang-Bang Optimal Control Method with Plasma Actuators. 1–10 (2018).

39. Shang, J. S. *et al.* Mechanisms of plasma actuators for hypersonic flow control. *Prog. Aerosp. Sci.* **41**, 642–668 (2006).

40. Erfani, R., Zare-Behtash, H., Hale, C. & Kontis, K. Development of DBD plasma actuators: The double encapsulated electrode. *Acta Astronaut.* **109**, 132–143 (2015).

41. Walker, S. & Segawa, T. Mitigation of flow separation using DBD plasma actuators on airfoils : A tool for more efficient wind turbine operation. *Renew. Energy* **42**, 105–110 (2012).

42. Huang, X. & Zhang, X. Streamwise and spanwise plasma actuators for flow-induced cavity. *Phys. Fluids* **20**, 1–10 (2008).

43. Bak, M. S., Im, S. & Cappelli, M. A. Successive laser-induced breakdowns in atmospheric pressure air and premixed ethane – air mixtures. *Combust. Flame* **161**, 1744–1751 (2014).

44. Michael, J. B. *et al.* Subcritical microwave coupling to femtosecond and picosecond laser ionization for localized , multipoint ignition of methane / air mixtures Subcritical microwave coupling to femtosecond and picosecond laser ionization for localized , multipoint ignition o. *J. Appl. Phys.* **108**, (2017).

45. Wermer, L., Hansson, J. & Im, S. Dual-pulse laser-induced spark ignition and flame propagation of a methane diffusion jet flame. *Proc. Combust. Inst.* **000**, 1–8 (2016).

46. Eckbreth, A. C. *Laser Diagnostics for Combustion Temperature and Species*. (CRC Press, 1996).

47. Strutt, J. W. L. R. Investigation of the Character of the Equilibrium of an Incompressible Heavy Fluid of Variable Density. *Proc. London Math. Soc.* **14**, 170–177 (1883).

48. Limbach, C. M., Dumitrache, C. & Yalin, A. P. Laser Light Scattering from Equilibrium, High Temperature Gases: Limitations on Rayleigh Scattering Thermometry. *47th AIAA Plasmadynamics Lasers* 1–13 (2016).

49. Limbach, C. M. & Miles, R. B. Rayleigh and Thomson Scattering Diagnostics of Laser Air

Sparks : A Testbed for Tailoring Laser Plasmas. *45th AIAA Plasmadynamics Lasers Conf.* (2014). doi:10.2514/6.2014-2538

50. Limbach, C. M. & Miles, R. B. Simultaneous Temperature, Density and Velocity Measurements in Laser-Generated Plasmas by Rayleigh and Filtered Rayleigh Scattering. *AIAA Proc.* (2014). doi:10.2514/6.2014-0143

51. Friss, A. & Yalin, A. P. Cavity-enhanced Thomson scattering measurements of electron density and temperature in a hollow cathode discharge. *Opt. Lett.* **43**, 5343–5346 (2018).

52. Friss, A., Limbach, C. M. & Yalin, A. P. Cavity-enhanced rotational Raman scattering in gases using a 20 mW near-infrared fiber laser. *Opt. Lett.* **41**, 3193–3196 (2016).

53. Joshi, S., El-Rabii, H., Dumitrescu, C., Puzinauskas, P. & Yalin, A. P. Temperature and electron density measurements of laser-induced plasmas in air at elevated pressures. *Spectrosc. Lett.* **44**, 103–112 (2011).

54. Glumac, N., Elliott, G. & Boguszko, M. Temporal and Spatial Evolution of the Thermal Structure of a Laser Spark in Air. *43rd AIAA Aerosp. Sci. Meet. Exhib.* 1–16 (2005). doi:10.2514/6.2005-204

55. Butte, C., Dumitrache, C. & Yalin, A. Properties of Dual-Pulse Laser Plasmas and Ignition Characteristics in Propane-Air and Methane-Air Mixtures. *2019 AIAA Aerosp. Sci. Meet. AIAA Scitech Forum* (2019).

56. Phuoc, T. X. An experimental and numerical study of laser-induced spark in air. *Opt. Lasers Eng.* **43**, 113–129 (2005).

57. El-Rabii, H., Victorov, S. B. & Yalin, A. P. Properties of an air plasma generated by ultraviolet nanosecond laser pulses. *J. Phys. D. Appl. Phys.* **42**, 075203 (2009).

58. Dumitrache, C. & Yalin, A. Numerical Modeling of the Hydrodynamics Induced by. *2018 AIAA Aerosp. Sci. Meet. AIAA SciTech Forum* (2018). doi:10.2514/6.2018-0689

59. Ballester, J. *et al.* Chemiluminescence monitoring in premixed flames of natural gas and its blends with hydrogen. *Proc. Combust. Inst.* **32**, 2983–2991 (2009).

60. He, L., Guo, Q., Gong, Y., Wang, F. & Yu, G. Investigation of OH∗ chemiluminescence and heat release in laminar methane–oxygen co-flow diffusion flames. *Combust. Flame* **201**, 12–22 (2019).

61. Kathrotia, T., Riedel, U., Dreier, T. & Schulz, C. Strain rate and fuel composition dependence of chemiluminescent species profiles in non-premixed counterflow flames: Comparison with model results Strain rate and fuel composition dependence of chemiluminescent species profiles in non-premixed counterflow. *Appl. Phys. B* **107**, 561–569 (2012).

62. Morsy, M. H. & Chung, S. H. Numerical simulation of front lobe formation in laser-induced spark ignition of ch 4 /air mixtures. *Proc. Combust. Inst.* **29**, 1613–1619 (2002).

63. Endo, T. *et al.* An experimental study on the ignition ability of a laser-induced gaseous breakdown. *Combust. Flame* **178**, 1–6 (2017).

64. Kojima, H., Takahashi, E. & Furutani, H. Breakdown plasma and vortex flow control for laser ignition using a combination of nano- and femto-second lasers. *Opt. Express* **22**, 90–98 (2014).

65. Beduneau, J., Kim, B., Zimmer, L. & Ikeda, Y. Measurements of minimum ignition energy in premixed laminar methane/air flow by using laser induced spark. *Combust. Flame* **132**, 653–665 (2003).

66. Glassman, I., Yetter, R. & Glumac, N. *Combustion*. (Elsevier Inc., 2014).

67. Wu, Y., Zhang, Z. & Adams, S. F. Temperature sensitivity of molecular oxygen resonant-enhanced multiphoton ionization spectra involving the C3Πgintermediate state. *Appl. Phys. B Lasers Opt.* **122**, 1–10 (2016).

68. Adams, S. F., Miles, J. A. & Laber, A. C. Resonant Laser Induced Breakdown for Fuel-Air Ignition. *AIAA J.* **48**, 1–5 (2010).

69. Dumitrache, C., Butte, C., Eickelberg, A. & Yalin, A. P. On the Use of REMPI Pre-Ionization for Laser Plasma Formation. *2018 AIAA Aerosp. Sci. Meet.* (2018). doi:10.2514/6.2018-1431

70. Adams, S. F. & Williamson, J. M. Spectroscopic Study of N2 (b1Πu, ν = 8) by Atmospheric-Pressure Resonant-Enhanced Multiphoton Ionization and Fluorescence Detection. *J. Phys. Chem.* **117**, 13535–13542 (2013).

71. Dibble, R. W. Laser Rayleigh Thermometry in Turbulent Flames. *Eighteenth Symp. Combust. Combust. Inst.* 1489–1498 (1981).

72. Miles, R. B., Lempert, W. R. & Forkey, J. N. Laser Rayleigh Scattering. *Meas. Sci. Technol.* **12**, (2001).

73. Adams, S. F., Schweickert, D. L., Tolson, B. A. & Hensley, A. L. Resonant Laser-Induced Breakdown across High Voltage Gap for Air-Fuel Ignition. *IEEE Trans. Plasma Sci.* 159–162 (2014).

74. Forkey, J. N. Development and Demonstration of Filtered Rayleigh Scattering- A Laser Based Flow Diagnostic for Plana Measurement of Velocity, Temperature, and Pressure. (1996).

75. Tenti, G., Boley, C. D. & Rashmi, D. On the Kinetic Model Description of Rayleigh-Brillouin Scattering from Molecular Gases'. *Natl. Res. Concil Canada* **52**, 285–290 (1974).

76. Elliott, G. S., Glumac, N. & Carter, C. D. Molecular filtered Rayleigh scattering applied to combustion. *Meas. Sci. Technol.* **12**, 452–466 (2001).

77. Boguszko, M. & Elliott, G. S. On the use of filtered Rayleigh scattering for measurements in compressible flows and thermal fields. *Exp. Fluids* **38**, 33–49 (2005).

78. Yalin, A. P., Ionikh, Y. Z. & Miles, R. B. Gas temperature measurements in weakly ionized glow discharges with filtered Rayleigh scattering. (1999). doi:10.2514/6.1999-3431

79. Hoffman, D. & M, K. Two-dimensional temperature determination in sooting flames by filtered Rayleigh scattering. *Opt. Lett.* **21**, 525–527 (1996).

80. Elliott, R. & Watts, H. Diffusion of some Hydrocarbons in Air : a Regularity in the Diffusion Coefficients of a Homologous Series. *Can. J. Chem.* **50**, 31–34 (1971).

81. Klein, M., Hanley, H. J. M., Smith, F. J. & Holland, P. *Tables of Collision Integrals and Second Virial Coefficients for the (m,6,8) Intermolecular Potential Function*. *US Department of Commerce* (1974).

82. Klein, M. & Hanley, H. J. M. Application of the m-6-8 Potential to Simple Gases. *J. Phys. Chem.* **76**, 1743–1751 (1972).

83. Matsunaga, N., Hori, M. & Nagashima, A. Gaseous Diffusion Coefficients of Propane and Propylene into Air, Nitrogen and Oxygen. *Netsu Bussei* **21**, 143–148 (2007).

84. Krokidas, P., Castier, M., Moncho, S., Brothers, E. & Economou, I. G. Molecular Simulation Studies of the Di ff usion of Methane, Ethane, Propane, and Propylene in ZIF-8. *J. Phys. Chem.* **119**, 27028–27037 (2015).

85. Kholmurodov, K., Abasheva, M. & Yasuoka, K. Molecular dynamics simulations of valinomycin interactions with potassium and sodium ions in water solvent. *Adv. Biosci. Biotechnol.* 216–223 (2010). doi:10.4236/abb.2010.13030

86. Holland, P. M. & Hanley, H. J. M. A Correlation of the Viscosity and Thermal Conductivity Data of Gaseous and Liquid Propane. *J. Phys. Chem.* **8**, 559–575 (1979).

87. Roberts, R. C. Molecular Diffusion of Gases.

88. Tang, M. J., Shiraiwa, M., Pöschl, U., Cox, R. A. & Kalberer, M. Compilation and evaluation of gas phase diffusion coefficients of reactive trace gases in the atmosphere : Volume 2 . Diffusivities of organic compounds , pressure-normalised mean free paths , and average Knudsen numbers for gas uptake calculations. *Atmos. Chem. Phys.* **15**, 5585–5598 (2015).

89. Illinois-Champaign, U. of. *Einstein Diffusion Equation*. (1999).

Appendix A: Confirming that Error Estimates for FRS are Accurate

This aside from the analysis of the constant pressure case examines whether our integration process and vertical scaling is valid and explains how calculations for bulk velocity error are done. For the 0 m/s case, the transmission percentages are normalized by the ambient condition (298 K, 1 bar, 0 m/s). For elevated velocities, the "ambient" case cannot be used because it assumes a non-zero bulk velocity. Instead, we must correct by the absolute ambient case where the bulk velocity is zero. For both the CP and CV cases, the transmission at absolute ambient (v = 0 m/s) is 47.164%. For each Doppler shifted case, we develop a new *I/Io* curve based on the following equation:

$$\left(\frac{I}{I_0}\right)_{filtered} = \left(\frac{I}{I_0}\right)_{unfiltered} * \frac{t(T,v)}{t(T_0, v=0)} \tag{A.1}$$

Here, I is the scattering signal, Io is the reference signal, T is the elevated temperature, To is the reference temperature, v is the bulk velocity, and t is the transmission at some given conditions. The transmission is the hardest to model, as it does not have any predictable behavior with changes in v, because of the locations of the transitions of I_2. For the first 2500 K, the curve very accurately follows the 1/T behavior.

$$\left(\frac{I}{I_0}\right)_{unfiltered} \approx \frac{T_0}{T} \quad \therefore \quad \left(\frac{I}{I_0}\right)_{filtered} \approx \frac{T_0}{T} * \frac{t(T,v)}{t(T_0, v=0)} \tag{A.2}$$

Equation A.1 is the one that is used for calculations of *I/Io*. This curve can be accurately modeled as Equation A.2 up to the cutoff temperature of 2500 K. After this point, it departs due to high electron densities. The difference in the filtered and unfiltered curves at any temperature can then be represented by:

$$\left(\frac{I}{I_0}\right)_{filtered} - \left(\frac{I}{I_0}\right)_{unfiltered} \approx \frac{T_0}{T}\left(\frac{t(T,v)}{t(T_0, v=0)} - 1\right) \tag{A.3}$$

To determine if we are actually properly determining the final *I/Io* for each elevated velocity, we can check our results against the *1/T* model for the region over which it applies (0-2,500 K). Differentiating Equation A.2 and recognizing that *To* and $t(T_0,\ v=0)$ are constants, we get:

$$\frac{d}{dT}\left(\frac{I}{I_0}\right)_f \approx \frac{T_0}{T} * \frac{\frac{dt(T,v)}{dT}}{t(T_0,\, v{=}0)} - \frac{t(T,v)}{t(T_0,\, v{=}0)}\frac{T_0}{T^2} \tag{A.4}$$

When we multiply this result by dT, we obtain:

$$d\left(\frac{I}{I_0}\right)_f \approx \frac{T_0}{Tt(T_0,\, v{=}0)}\left(dt(T,v) - \frac{t(T,v)}{T}dT\right) \tag{A.5}$$

There are two ways to evaluate this equation that will be informative. The first is to assume a temperature (vertical line) so that *dT* is zero. This will describe the error in assuming *1/T*. The equation can then be written as:

$$d\left(\frac{I}{I_0}\right)_f \approx \frac{T_0}{Tt(T_0,\, v{=}0)}\left(dt(T,v)\right) \tag{A.6}$$

The second is to assume a normalized signal (*I/Io*) (horizontal line) so that d(*I/Io*) is zero. This will describe the error induced in assuming zero bulk velocity when it is non-zero. The equation can then be written as:

$$dt(T,v) = \frac{t(T,v)}{T}dT \rightarrow dT = \frac{Tdt(T,v)}{t(T,v)} \tag{A.7}$$

Examining the first case (Equation A.6), we expect that for a given change in filter transmission (dictated by the change in bulk velocity), we can predict the change in *I/Io* at that temperature. We expect the error here (defined below in Equation A.8) to be zero if the *1/T* model accurately predicts the curve. Here, we always use the zero velocity case as $(I/Io)_1$ and use elevated velocities for the $(I/Io)_2$ case. The resulting error as a function of temperature is shown in Fig. A.1.

$$err(\%) = \frac{\left(\frac{I}{I_0}\right)_2 - \left(\left(\frac{I}{I_0}\right)_1 + d\frac{I}{I_0}\right)}{\left(\frac{I}{I_0}\right)_2} \tag{A.8}$$

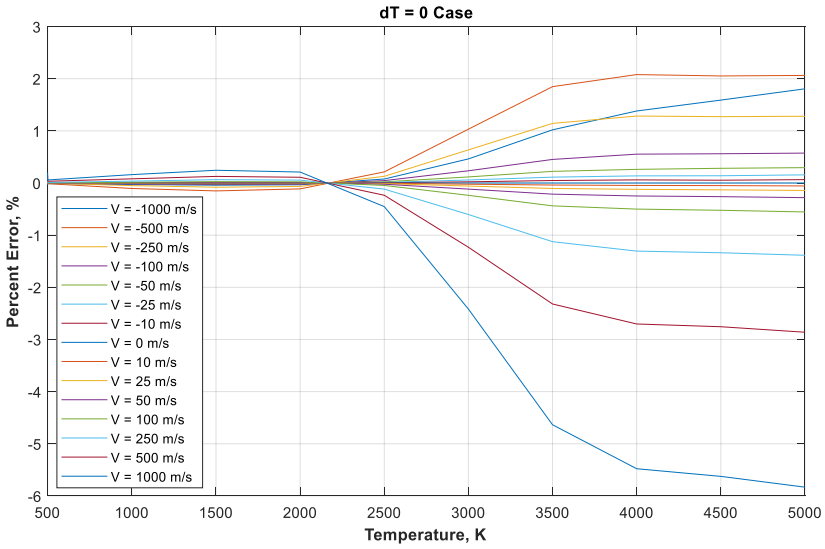

Figure A.1: The estimated error associated with performing pointwise 1-D data interpolation, when compared with symbolically solving for the change in intensity based on the ideal gas relationship. Note how the error departs from zero at 2200 K, which is in good agreement with section 2.3.2.

As anticipated, we experience negligible error (<0.245%) for the region where the To/T assumption holds. After this, the error diverges due to increasing electron density. We experience non-zero error here due to the point spacing (500 K) and the corresponding error associated with interpolation with ~large grid spacing.

Examining the second case (Equation A.7), we expect that for a given change in filter transmission (dictated by the change in bulk velocity), we can predict the change in the reported temperature. This can be interpreted as a horizontal line in the *I/Io* curves. We expect the error (described by Equation A.9) to be non-zero. The amount of error will tell us exactly how much error we can anticipate if we assume a zero velocity and the scattering volume actually possesses some elevated velocity, assuming the 1/T assumption. The corresponding error is shown in Fig.

A.2, where the left plot shows small Doppler shifts and bulk velocities, while the right plot shows larger bulk velocities.

$$err(\%) = \frac{dT}{T} \tag{A.9}$$

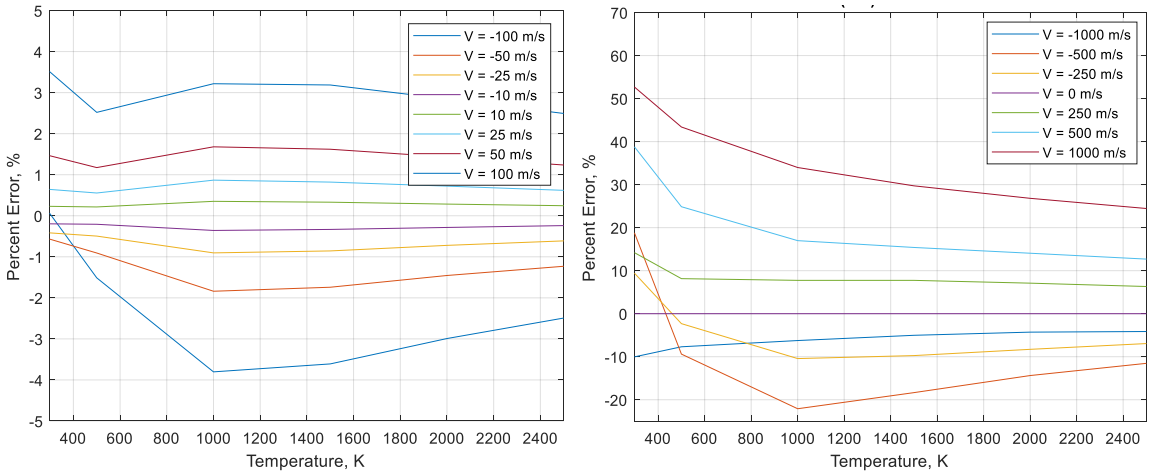

Figure A.2: Estimated error induced by assuming a net zero bulk velocity when the bulk velocity is actually in the range of 0-100 m/s (left) or 250-1000 m/s (right). Note that the error is only approximated over the region where we know the 1/T assumption (and corresponding error equation) holds.

We see that below 100 m/s, all error is below 3.803%. You will notice that bulk velocities > 250 m/s have problematic error at the low temperatures (mainly because of the dt term). For example, at very low temperatures, nearly 100% of the RBS signal is transmitted at 1000 m/s opposed to the 47% reference transmission at 0 m/s. Since we apply CP to t>5 µs, we will have to examine modeling results and evaluate whether or not any of these low temperature high velocity regions exist. Secondarily, in order to validate that our integration technique is appropriately correcting observed intensity values, we need to compare the results of calculating dT symbolically with the error found by 1-D data (Fig. A.3). Comparing the two over the range of applicability, we see that the interpolated result is similar, but larger than the To/T case, especially at low temperatures.

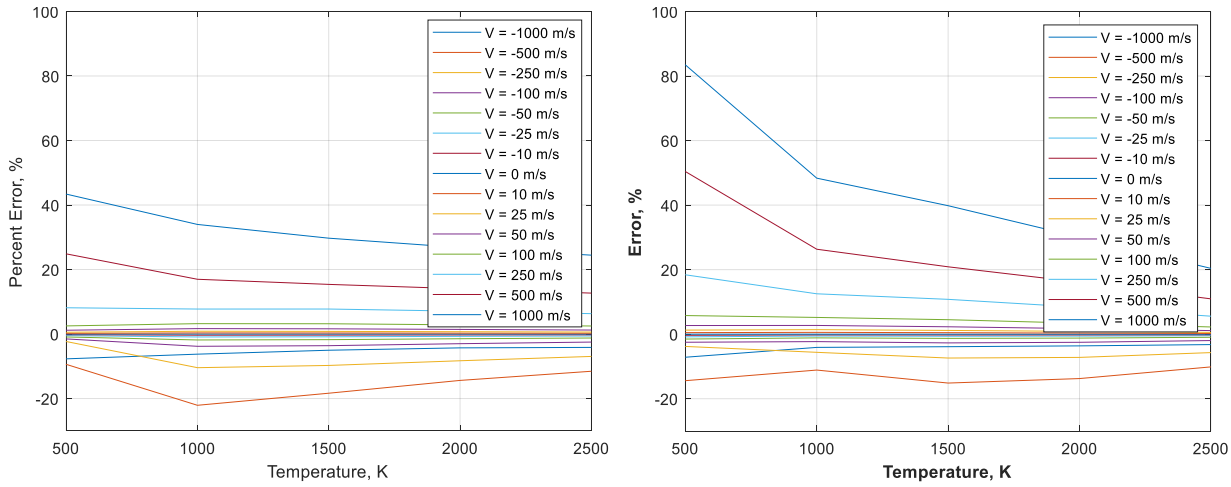

Figure A.3: Estimated error induced by assuming a net zero bulk velocity when the bulk velocity is non-zero for symbolic 1/T analysis (left) and for 1-D data interpolation (right).

Delving into the data, we see that this is again due to grid spacing and interpolation. Since we have grid spacing of 500 K, our *I/Io* curve is higher than the To/T curve for the interpolated points (see Fig A.4, a zoomed in version of Fig 4.4). For this reason, interpolation for a given *I/Io* gives us larger differences in dT (when the Doppler shifted curve is left of the zero velocity case- see Fig 4.4) and smaller when the Doppler shifted curve (seen in red in Fig. 4.4 is to the right of the zero velocity case. The slope of the line amplifies this error, resulting in a small change in dT (<200 K) which results in a large error @ low temperature due to the equation provided. For example, lets take the 1000 m/s case, which lies left of the 0 m/s case. For the symbolic evaluation at 500 K, we calculate a dT of 217 K and therefore an error of 217/500 = 43.4%. For the numerical interpolation, we have a much larger change in temperature (417 K) because of the slope at this point and the need to extend further than the 1/T curve. This gives us an error of 417/500 K=83.4 %. In general, I would encourage smaller grid spacing for better error, but because both error measurements are relatively consistent above 1000 K, I would argue that the scattering region is no longer interesting at this point, and will not end up being reported. For this reason, we will use

the error from the 1/T equation for the region (0-2500 K) and then will extend interpolated results to the rest of the measurement region (2500 K – 22000 K), where To/T does not apply.

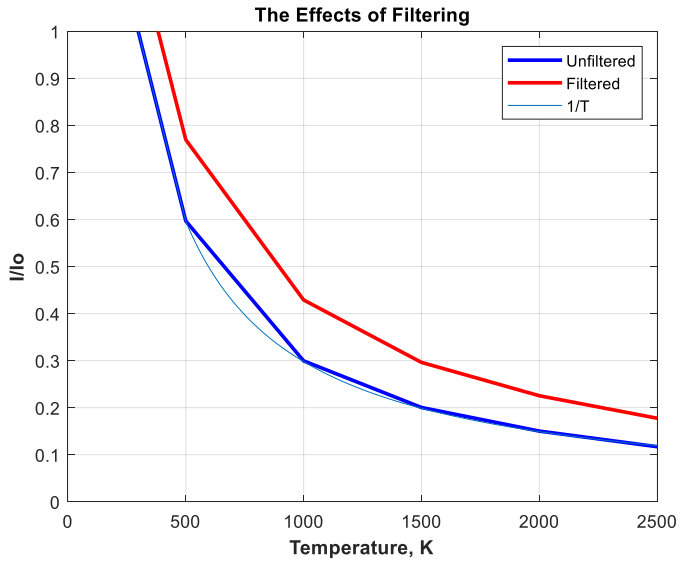

Figure A.4: A zoomed in version of Fig. 4.4, showing that the lower resolution filter points overestimate the 1/T approximation when interpolation occurs.

Appendix B: Determining Variation in the Diffusion Constant

Using the Boltzmann transport equation (a way to define the hydrodynamic properties of a system diffusing from non-equilibrium), we can derive an equation for the diffusion coefficient using Chapman-Enskog theory, a hydrodynamic solution at the particle scale to the Boltzmann equation which relates heat, mass, and particle transport.[81,82]

$$D = \frac{AT^{\frac{3}{2}}}{P\sigma_{12}\Omega}\sqrt{\frac{1}{M_1}+\frac{1}{M_2}} \tag{B.1}$$

The resulting equation is a function of the mixture temperature (T) and pressure (P), the mean collision diameter (σ_{12}), the collision integral (Ω), and the molar masses of the constituents (M). One of the major takeaways from this equation is that the diffusion constant is proportional to the temperature to the 3/2 ($D \sim T^{3/2}$).[82] This is significant because it can help characterize the effect of varying preheat temperature, and will be discussed later in this chapter.

First, we need to evaluate the variation in the diffusion coefficient as a function of the equivalence ratio for the three fuel-air mixtures of interest (propane, methane, and hydrogen). For our purposes, we start by assuming instantaneous heat transfer to the mixture from the walls (constant temperature at the preheat temperature T=50°C=323K). This assumption will be investigated later in this chapter. Defining terms, $A = 1.859\ x\ 10^{-3}\ \frac{atm\ Å\ cm^2\sqrt{\frac{g}{mol}}}{K^{\frac{3}{2}}\ s}$ is the empirical coefficient, P is the chamber pressure, which is always set to P=1 bar=0.987 atm, and the molar masses correspond to air (M_1 = 28.965 g/mol) and the fuel of interest ($M_{2\text{-Propane}}$ = 44.100 g/mol, $M_{2\text{-Methane}}$ = 16.040 g/mol, $M_{2\text{-Hydrogen}}$ = 2.016 g/mol). The collision diameter and collision integral are more complex to define. For these values, a intermolecular potential function is presented,

generally the (m,6,8) potential, which defines σ_{12} as the "characteristic distance associated with the potential," and $\Omega = \Omega^{(1,1)*}(T^*)$ as the reduced temperature dependent collision integral at the reduced temperature $T^* = kT/\epsilon$. This parameter is calculated based on the integral cross section (a measured quantity), the initial relative kinetic energy of the particles, and the temperature. These values are tabulated provided you know the m and γ parameters of the mixture. The m parameter is defined as the repulsive index, and is specific to the constituent molecules in a mixture. The γ parameter is referred to as the inverse eight attraction strength, because it is proportional to a characteristic distance (or radius-r_m) where the intermolecular potential function is maximized to the negative eighth power:[82]

$$\gamma = \frac{C_8}{\epsilon {r_m}^8} \tag{B.2}$$

In this equation, C_8 is the coefficient indicating the strength of attraction, and ϵ is the maximum of the intermolecular potential energy. If ϕ represents the intermolecular energy, you can relate ϵ to r_m by $\phi(r_m) = -\epsilon$. For most molecules, the values of m, γ, σ, and ϵ/k (where k= $1.381\times10^{-23}\ \frac{kg*m^2}{s^2\,\mathrm{K}}$ is the Boltzmann constant), are tabulated in literature.[81] Realizing that air is composed of a number of different species, we have acquired the desired parameters for these variables, and compiled them in Table B.1. We use the values of m and γ to locate the proper tabulated collision integrals in the Klein tables, and find $\Omega^{(1,1)}$ based upon T* = T/(ϵ/k) by interpolation between temperatures. We don't know the γ parameter for hydrogen, so we bound our values of $\Omega^{(1,1)}$, based on the limits to what γ could be.[81]

Table B.1: Parameters used to calculate the diffusion coefficient across varying equivalence ratios for propane-air, methane-air, and hydrogen-air mixtures.

	N_2	O_2	Ar	CO_2	CH_4	C_3H_8	H_2
m	12	10	11	14	11	11	12
γ	2	1	3	1	3	3	?
σ	3.54	3.437	3.292	3.68	3.68	3.75	1.78
ϵ/k	118	113	153	282	168	358.9	11.423
T^*	2.7373	2.8584	2.111	1.1454	1.9226	0.9	28.2534
$\Omega^{(1,1)}$	0.9785	0.9528	1.0519	1.3155	1.0839	1.46922	(0.6294-0.6521)

We now calculate a reduced collision integral Ω and characteristic distance σ (average collision diameter) based upon the weighted average of the components. We assume well documented air constituents (N_2=78.084%, O_2=20.946%, Ar=0.934%, CO_2=0.033%) and neglect species with contributions less than 0.01%. We calculate a diffusion coefficient for all equivalence ratios using variable weighted averages for Ω and σ based on the molar compositions of fuel and air for each equivalence ratio. The resulting equivalence ratio dependent collisional cross sections and diffusion coefficients are shown for the three fuels in Fig. B.1. Note that only the domain for which successful ignition has been observed is plotted.

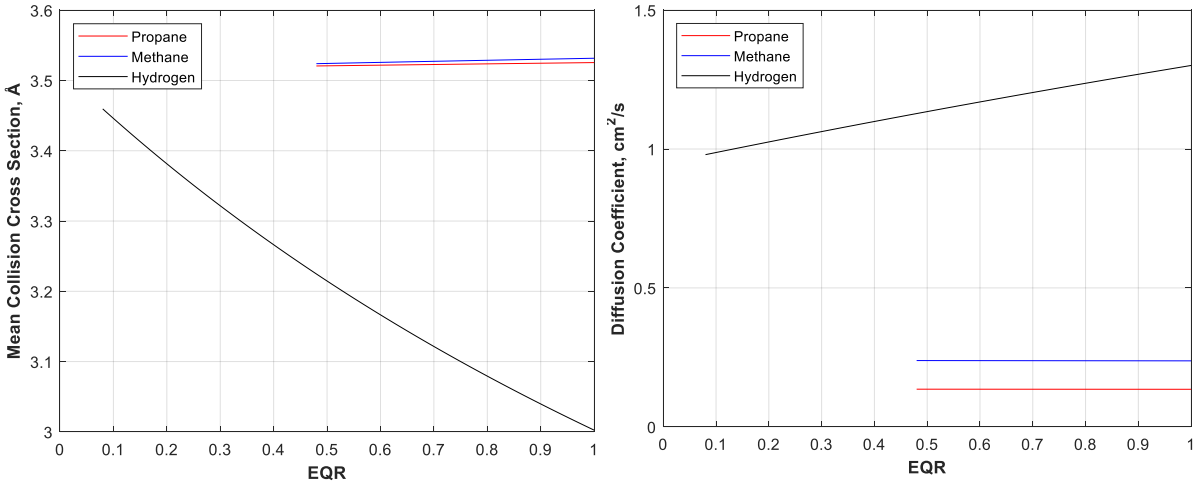

Figure B.1: Equivalence ratio dependent cross sections (left) as calculated as the weighted average of the constituents, and total diffusion coefficient (right).

We see that the mean collisional cross section changes very little for propane and methane. For these two fuels, cross section increases because the mean collisional cross section follows that of the fuel, and the cross section of fuel is greater than the cross section of air. The opposite is true for hydrogen, as is the magnitude of the difference in cross section. The result is that the diffusion coefficient varies much more for hydrogen than methane and propane, and in the opposite direction. The diffusion coefficient for hydrogen varies by 14.5% over the equivalence ratios of interest. When compared to the 0.11% of methane and 0.0682% of propane, this seems large, but with such a comparatively high diffusion coefficient, the results on necessary diffusion time are insignificant as will be shown later. We therefore can assume a constant diffusion coefficient at the mean value, and it will not introduce significant error to our calculations.

Appendix C: Confirming p(x,t) is a Solution to Fick's Second Law

Fick's second law can be found in Eqn. 5.1, where the proposed solution is found in Eqn. 5.2. Assuming the non-trivial solution, we evaluate each component of the sum, and prove that they independently are solutions to Fick's law, meaning that their sum is also a solution. First, we evaluate the first component by checking our boundary conditions. Our first boundary condition is that the slope must be zero at the reflective wall ($x = x_o$) at time $t = t_o$. We define a new variable ψ, to simplify the solution.

$$\psi = \frac{1}{2}[\pi D(t - t_0)]^{-1/2} \tag{C.1}$$

Solving for the slope at x_o, t_o we obtain the following. We see that it does indeed satisfy the boundary condition.

$$\frac{dp}{dx}(x_0, t_0) = \psi \exp\left[-\frac{(x-x_0)^2}{4D(t-t_0)}\right] * \frac{-2x+2x_0}{4D(t-t_0)}\Big|_{x=x_0} = \psi \exp\left[-\frac{(x-x_0)^2}{4D(t-t_0)}\right] * 0 = 0 \tag{C.2}$$

The second boundary condition assumes that at a far enough distance ($x = \infty$) the probability of finding a particle is zero. We see that as $x \rightarrow \infty$, the denominator of both components goes to infinity, and the probability goes to zero. We now evaluate whether or not the presented solution satisfies Fick's second law. We start by evaluating the right hand side of the equation, by taking the derivative of the probability function with respect to x twice. The first derivative is shown below.

$$\frac{dC}{dx} = \psi \exp\left[-\frac{(x-x_0)^2}{4D(t-t_0)}\right] * \frac{-2x+2x_0}{4Dt-4Dt_0} \tag{C.3}$$

Taking the derivative a second time, we obtain:

$$\frac{d^2C}{dx^2} = \psi \exp\left[-\frac{(x-x_0)^2}{4D(t-t_0)}\right] * \frac{-2}{4Dt-4Dt_0} + \frac{-2x+2x_0}{4Dt-4Dt_0} * \psi \exp\left[-\frac{(x-x_0)^2}{4D(t-t_0)}\right] * \frac{-2x+2x_0}{4Dt-4Dt_0} \tag{C.4}$$

Simplifying, the result becomes:

$$\frac{d^2C}{dx^2} = \psi \exp\left[-\frac{(x-x_0)^2}{4D(t-t_0)}\right] * \left[\left(\frac{-2x + 2x_0}{4Dt - 4Dt_0}\right)^2 - \frac{2}{4Dt - 4Dt_0}\right]$$

$$= \psi \exp\left[-\frac{(x-x_0)^2}{4D(t-t_0)}\right] * \frac{x^2 - 2xx_0 + {x_0}^2 - 2Dt - 2Dt_0}{4D^2t^2 - 8D^2tt_0 + 4D^2{t_0}^2}$$

$$= \psi \exp\left[-\frac{(x-x_0)^2}{4D(t-t_0)}\right] * \frac{x^2 - 2xx_0 + {x_0}^2 - 2Dt - 2Dt_0}{4Dt^2 - 8Dtt_0 + 4D{t_0}^2} \quad \text{(C.5)}$$

We know examine the left hand side of the equation, where we take the first derivative with respect to time. The result and its simplification process is shown below.

$$\frac{dC}{dt} = \psi \exp\left[-\frac{(x-x_0)^2}{4D(t-t_0)}\right] * \frac{(x-x_0)^2}{4D(t-t_0)^2} * 1 + \exp\left[-\frac{(x-x_0)^2}{4D(t-t_0)}\right]\frac{1}{2}\pi^{-\frac{1}{2}}D^{-\frac{1}{2}}\left[-\frac{1}{2}(t-t_0)^{-\frac{3}{2}}\right] * 1$$

$$= \psi \exp\left[-\frac{(x-x_0)^2}{4D(t-t_0)}\right] * \left[\frac{(x-x_0)^2}{4D(t-t_0)^2} - \frac{1}{2(t-t_0)}\right]$$

$$= \psi \exp\left[-\frac{(x-x_0)^2}{4D(t-t_0)}\right] * \left[\frac{x^2 - 2xx_0 + {x_0}^2}{4D(t^2 - 2tt_0 + {t_0}^2)} - \frac{1(2D)(t-t_0)}{2(t-t_0)(2D)(t-t_0)}\right]$$

$$= \psi \exp\left[-\frac{(x-x_0)^2}{4D(t-t_0)}\right]\left[\frac{x^2 - 2xx_0 + {x_0}^2 - 2Dt - 2Dt_0}{4Dt^2 - 8Dtt_0 + 4D{t_0}^2}\right] \quad \text{(C.6)}$$

Noting that this result matches the second derivative with respect to x, we can confirm that first component of the solution does indeed satisfy Fick's second law. The second component follows the same analysis and gives the same result. We are therefore able to present this solution knowing that it is indeed a solution to Fick's second law.

Appendix D: Chamber Redesign Drawings

Recommended chamber redesigns are presented in this section as a way of avoiding unintentional back reflection focusing on important upstream optics. Two parts exist here. The first is the chamber arm itself, which connects to the chamber housing via four machine screws at the base. The design has rotated the angle of window insertion off axis, as to allow for off axis back reflections. A small groove is designed for the 1" O-ring. The second part is the end cap, which screws onto the end of the arm once the O-ring, window, and teflon spacer have been inserted. Though it is directional, the through holes and taps are still along the axial direction of the chamber arm. Shown in Fig. D-1 is the chamber arm, and in Fig. D-2 is the end cap.

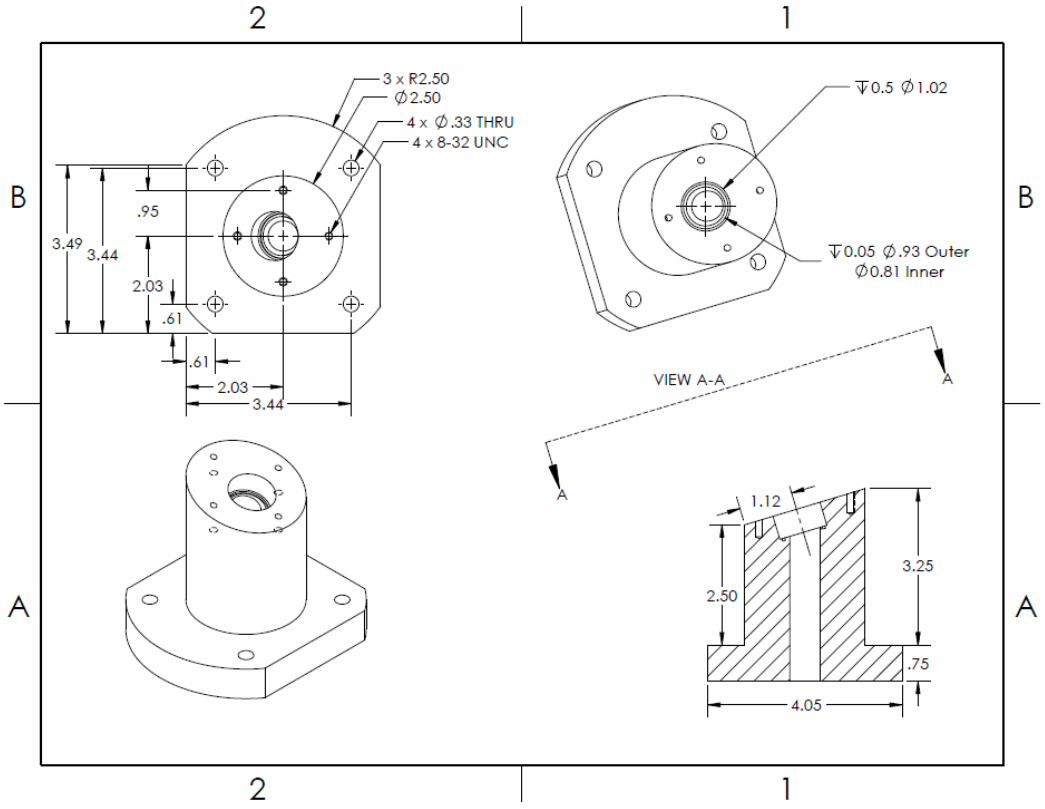

Figure D-1: The chamber arm for an off axis back-reflections. This is a modification that could be applied to our existing chamber.

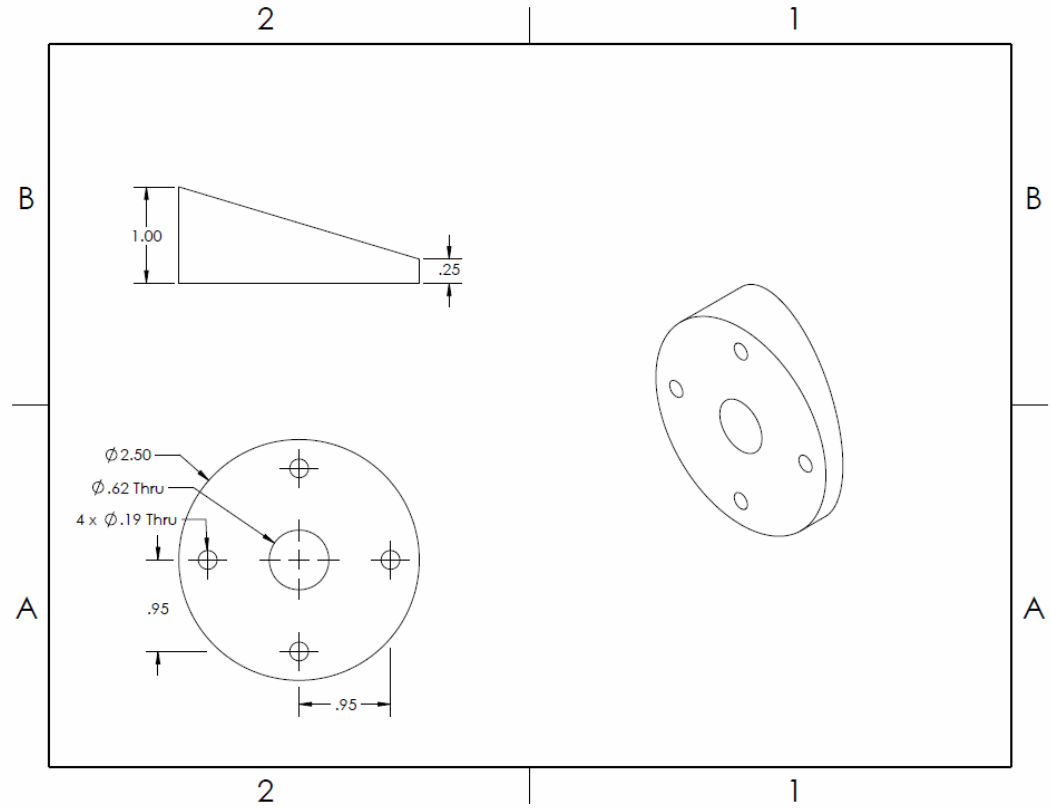

Figure D-2: The end cap for the chamber arm resulting in off axis back-reflections. This is a modification that could be applied to our existing chamber.